

MEASLES AND WHOOPING COUGH IN LONDON, AND IMMUNE AMNESIA

MEASLES AND WHOOPING COUGH IN LONDON 1750–1900, AND THE
ROLE OF IMMUNE AMNESIA IN RECURRENT EPIDEMICS

By HYEOK JUN LEE, B.Sc.

A Thesis Submitted to the School of Graduate Studies in Partial Fulfilment of the
Requirements for the Degree Master of Science

McMaster University © Copyright by Hyeok Jun Lee, April 2023

McMaster University MASTER OF SCIENCE (2023)

Hamilton, Ontario (Computational Science and Engineering)

TITLE: Measles and Whooping Cough in London 1750–1900, and the Role of Immune Amnesia in Recurrent Epidemics

AUTHOR: Hyeok Jun Lee, B.Sc. (University of Toronto)

SUPERVISOR: Dr. David Earn

NUMBER OF PAGES: x, 132

Lay Abstract

This thesis presents the weekly mortality time series of measles and whooping cough between 1750 and 1900, and describes their epidemic patterns over time. We also model the phenomenon of measles-induced immune amnesia (reduced pre-existing immunity after a measles infection), and examine how it alters the recurrent patterns of whooping cough at a population level. Additionally, we construct a plausible time series of the birth and all-cause mortality rate over the same 150 years. Overall, our analysis suggests immune amnesia alters the longer periodicities of whooping cough to resemble that of measles. Furthermore, we show that this longer periodic structure is similar to that of whooping cough in the late 19th century. Finally, the given mortality, birth rate, and all-cause mortality rate time series can serve as tools for other epidemiological studies, such as predicting long-term epidemic patterns of other diseases.

Abstract

Vaccine-preventable infectious diseases are still prevalent today. Hence, accurate data and techniques such as mathematical modelling are required to better understand their impact on a population level. This is especially the case for measles, as it has been identified to cause immune amnesia (IA): the loss of pre-existing immunological memory for other diseases after a measles infection. First, spectral analysis was used to describe the recurrent patterns of measles and whooping cough (WC) using weekly London mortality data between 1750–1900. Then, stochastic simulations of a model incorporating IA were performed to understand the effect of IA on the recurrent patterns of WC. The periodograms of the simulated model revealed that increasing IA strength and duration caused the longer periodicities of WC to resemble those of measles. This shift was seen for different population sizes, seasonal forcing amplitudes, and mean transmission rates, suggesting this trend can be observed in different ecological or social contexts. When the birth and death rates of London were used in the model with IA duration of less than a year, the WC periodogram of the simulations resembled that of the London mortality data between 1842–1900. Overall, the simulations demonstrate that IA may have contributed to the longer period spectral structure of WC that was found in the real data. Additionally, the mortality, birth rate, and death rate data presented in this thesis provide new tools for future studies in mathematical epidemiology.

Acknowledgements

I would first like to thank my supervisor Dr. David Earn for the guidance and insights he has provided during my research, and his support while I was working towards my degree.

I would also like to thank Dr. Ben Bolker and Dr. Jonathan Dushoff for taking time out of their busy schedules to be part of my examination committee.

I would like to thank the Mac Theobio lab, my peers, and the CSE department as well for making this experience more enjoyable.

Finally, I would like to thank my family and friends for all the support they have provided.

Contents

1	Introduction	1
1.1	Measles-induced Immune Amnesia	1
1.2	Objectives	2
2	Measles and Whooping Cough Mortality in London	3
2.1	London Bills of Mortality	3
2.2	Classification of Diseases in LBoM	3
2.3	Data Processing	4
2.4	Spectral Analysis	8
3	Modelling Immune Amnesia	12
3.1	The SEIR Model	12
3.2	The Two-Disease Immune Amnesia Model	14
3.3	The Adaptive Tau Algorithm	16
3.4	Methods	17
3.5	Results	19
4	Modelling Immune Amnesia with Time-Varying ν & μ	33
4.1	London Birth and Death Rates 1750–1900	33
4.2	Methods	38
4.3	Results	39
5	Discussion & Future Directions	48
5.1	Discussion	48
5.1.1	London measles and WC mortality, 1750–1900	48
5.1.2	IA and WC spectral structure	49
5.1.3	IA with different disease parameters	50
5.1.4	IA with time-varying ν and μ	51
5.1.5	Birth rate of London, 1750–1900	52
5.2	Future Directions	52
6	Conclusion	53
A	Analysis of Disease-Free Equilibria	60
B	Supplementary Figures	66
B.1	Simulations with $N = 8 \times 10^5$	67
B.2	Simulations with $N = 2.5 \times 10^6$	74
B.3	Simulations with $\nu_{\text{low}}(t)$ and $\mu(t)$	81
B.3.1	1750–1900	81
B.3.2	LBoM Period	88
B.3.3	RGWR Period	95

B.4	Simulations with $\nu_{\text{high}}(t)$ and $\mu(t)$	102
B.4.1	1750–1900	102
B.4.2	LBoM Period	109
B.4.3	RGWR Period	116
C	Sample Codes	123
C.1	Processing & Analyzing London Mortality Data	123
C.2	Base Code for Stochastic Simulation of IA Model	127

List of Figures

1	Measles and Whooping Cough Mortality in London	5
2	Validation of Mortality Data	6
3	All-Cause Mortality & Normalized Disease Mortality	7
4	Periodograms of Measles & Whooping Cough	9
5	Wavelet Spectra of Measles & Whooping Cough	11
6	SEIR Model	12
7	Two-Disease Immune Amnesia Model	15
8	Incidence Time Series from Simulation	20
9	Power Spectra for $\theta = 0.5$	21
10	Comparison of Average Power Spectra for $N = 8 \times 10^5$	22
11	Changes in Spectral Structure for Different θ and $1/\kappa$, $N = 8 \times 10^5$	23
12	Wavelet Spectra of Simulation Data	26
13	Changes in Spectral Structure for Different θ and $1/\kappa$, $N = 2.5 \times 10^6$	27
14	Average Power Spectra for Different α	30
15	Average Power Spectra for Different $\langle\beta\rangle$	33
16	Birth and All-Cause Mortality in London	34
17	Population Size of London	35
18	Birth Rate and All-Cause Mortality Rate of London	36
19	Correcting Calculated Birth Rate of London	37
20	Comparing London and England Vital Rates	38
21	Changes in Spectral Structure for Different θ and $1/\kappa$, $\nu(t)$ & $\mu(t)$ 1750–1900	41
22	Changes in Spectral Structure for Different θ and $1/\kappa$, $\nu(t)$ & $\mu(t)$ LBoM	42
23	Changes in Spectral Structure for Different θ and $1/\kappa$, $\nu(t)$ & $\mu(t)$ RGWR	44
24	Periodogram of Measles & Whooping Cough in Different Time Periods	45
25	Comparing Periodograms of London Mortality Data and Simulations	46
26	N in simulations with Time-varying ν and μ	47
27	Comparing Periodicity of Disease Mortality with Literature	49
28	Two Disease Immune Amnesia Model SIR Version	60
29	Additional Periodograms for $N = 8 \times 10^5$	73
30	Additional Periodograms for $N = 2.5 \times 10^6$	80
31	Additional Periodograms for Time-Varying ν_{low} and μ	87
32	Additional Periodograms for Time-Varying ν_{low} and μ in LBoM	94
33	Additional Periodograms for Time-Varying ν_{low} and μ in RGWR	101
34	Additional Periodograms for Time-Varying ν_{high} and μ	108
35	Additional Periodograms for Time-Varying ν_{high} and μ in LBoM	115
36	Additional Periodograms for Time-Varying ν_{high} and μ in RGWR	122

List of Tables

1	Parameters in Simulations	18
2	State Changes in Simulations	18

List of Abbreviations

ACM All-Cause Mortality
DFE Disease-Free Equilibrium
EMD Empirical Mode Decomposition
IA Immune Amnesia
LBoM London Bills of Mortality
ODE Ordinary Differential Equation
PDFE Partial Disease-Free Equilibrium
RGWR Registrar General's Weekly Returns
SEIR Susceptible-Exposed-Infectious-Recovered
SIR Susceptible-Infectious-Recovered
SSA Stochastic Simulation Algorithm
WC Whooping Cough

1 Introduction

Before the development of vaccines, airborne infectious diseases such as measles and whooping cough (WC) contributed to a significant proportion of childhood mortality. For example, measles was estimated to cause about 4 million deaths per year before the introduction of vaccines in 1963 [1]. Despite the implementation of vaccinations, some infectious diseases remain endemic across the world. Recently, measles was found to cause more than 140000 deaths in 2018 [2], while more than 160000 WC deaths were estimated in 2014 [3]. In addition, the emergence of new infectious diseases such as COVID-19 and their global impact emphasize the continual need to investigate these types of diseases.

A natural way to study infectious diseases is to analyze population-level data, such as disease incidence or mortality. These data provide insight into how epidemiological patterns and disease dynamics changed over time, which could be applied when trying to control newly identified infectious diseases [4]. Furthermore, epidemiological data can be used for the development of mathematical models in attempts to explain or predict epidemic patterns and dynamics [5, 6]. Previous studies were able to successfully describe the dynamics of measles using relatively simple models [5, 7]. However, some diseases, such as WC, have imposed challenges when trying to model their patterns, especially during the pre-vaccination era [8, 9]. Hence, it is crucial that high quality data is curated to generate accurate models and conclusions. Using these models, the role of factors such as age structure, spatial dynamics, and contact patterns on disease dynamics could be investigated [10]. Another relationship that can be investigated through models is the immunological interaction between multiple infectious diseases [11, 12, 13].

1.1 Measles-induced Immune Amnesia

Measles is a highly contagious respiratory disease caused by the measles virus, which leads to symptoms such as fever, rash, coughs, and potentially death [1]. Measles infections have also been thought to cause immunosuppression for many years [14], and secondary infections brought on after measles infections were described in the 18th and 19th century [15, 16]. Charles Creighton's tome from 1894 reported that children recovering from measles in greatly weakened conditions were easier targets for smallpox, and some years of measles epidemics were followed by high mortality of smallpox and WC [16, pp.640, 674-675]. Similarly, recent retrospective and cohort studies have reported increased rates of hospital admission and risk of rehospitalization due to infectious disease after hospitalization for measles [14, 17, 18, 19]. Furthermore, studies analyzing population-level data found that measles incidence and mortality was positively correlated with that of other infectious diseases, and the reduction of measles due to vaccinations was temporally coupled with the reduction of other infec-

tious diseases [19, 20, 21, 22, 23]. This correlation may be caused by measles-induced immune amnesia (IA). Specifically, measles infections have been found to result in the depletion of memory B cells, reduced B cell diversity, and decreased antibody repertoire [24, 25, 26], leading to diminished pre-existing immunological memory. These immunological changes may be accompanied by increased susceptibility to diseases for which immunity has previously been developed.

IA is an emerging concern as measles is considered endemic in some regions [27], and declining vaccination rates due to vaccine hesitancy may reintroduce measles to countries where it has been previously controlled [28, 29]. Through analytical and computational analysis, Morales and Munoz [12] found that relaxing measles vaccination could lead to the disappearance of herd immunity for the secondary infectious disease, leading to severe outbreaks despite extensive vaccination for the secondary disease. Yet, how IA influences the dynamics and epidemiological patterns of other diseases, such as their recurrent patterns, is still not well understood. By fitting a model incorporating measles-induced immunosuppression, Noori and Rohani found that simulations with the fitted model had variable agreement with weekly London WC incidence and mortality data across three time periods in the 20th century [13]. However, they suggested that stochastic models may better explain periods with irregular oscillations and emphasized the need for further work on understanding IA. Despite consistent findings supporting this effect, studies have reported varying estimates for how long measles may increase susceptibility to other diseases, ranging between 1 month to 5 years [14, 17, 18, 20, 19, 21, 23]. In addition, the strength of this effect is not known, as it may not fully deplete all memory B cells to fight against immunity-developed diseases [12].

1.2 Objectives

Section 2 will introduce the weekly London mortality time series of measles and WC spanning 150 years, and their long-term dynamics will be analyzed using spectral analysis. Section 3 will present a two-disease model that includes measles-induced IA, and investigate the role of IA on the recurrent epidemics of WC through stochastic simulations. Finally, in Section 4, time-varying birth and death rates, pertaining to the time period of the mortality time series in Section 2, will be incorporated into the model to see if IA could have played a role in the observed dynamics of WC during this period.

2 Measles and Whooping Cough Mortality in London

2.1 London Bills of Mortality

To explore the long-term patterns of measles and WC, weekly mortality data of these diseases in London were analyzed. Previous studies looking at the dynamics of these diseases in London used annual data or weekly data mainly from the 20th century [6, 7, 8, 9, 30, 31, 32, 33, 34]. We used the London Bills of Mortality (LBoM) which reported the number of baptisms, and church burials categorized by the cause of death. The LBoM was aggregated from individual Anglican parish registers, with weekly statistics reliably available starting in the 17th century [4]. However, there are several factors which may have contributed to inaccuracies and underreporting in the LBoM. Some of these summarized by Krylova and Earn [4] include:

- Omission of births or deaths outside of Anglican grounds, such as dissenters and poor families unable to pay related fees [4, 35].
- Excluding the growth of certain parishes and failing to account for London’s increasing geographic boundaries [4, 16, 36].
- The progressive collapse of the parish registration system starting in the early 19th century as the civil registration system took over [4, 16, 36]. However, accompanying this collapse was the establishment of the Registrar General’s Weekly Return (RGWR) in 1837, which included all births and deaths with better geographical coverage by 1841 [4].

Even though LBoM may not perfectly represent the true disease mortality due to these issues, the LBoM was probably the most accurate account of London baptisms and burials during its time [30]. For further analysis, we assume that temporal patterns in burials reported by the LBoM were roughly proportional to the true mortality, and that changes in the degree of underreporting were slow [4].

2.2 Classification of Diseases in LBoM

A key feature of the LBoM is that burials are categorized by cause of death, including deaths due to diseases. However, due to the limitations of diagnostic techniques and changes in medical conventions, the reliability of this categorization may be questioned. For example, due to similarities in symptoms, measles was commonly confused with scarlatina during the late 18th century [16, p. 633]. Meanwhile, WC was initially included under general “coughs” until its own category was created in the early 1700s [16, p. 668]. In addition, a lot of infant deaths in the early 1700s may not reflect actual

disease cases, as a majority of deaths under two years of age were listed under “convulsions” and “teeth” [16, p. 669]. In fact, there was a substantial increase in recorded WC deaths along with the decline of convulsion deaths in the latter half of the 18th century, and Creighton suggests this is likely due to better classification [16, p. 669]. Aside from diagnostic issues, LBoM was also affected by changes in naming conventions. For example, measles was listed jointly under “flox, smallpox and measles” from 1687 to 1700 [16, p. 640], whereas WC was first listed under “chincough” [16, p. 668].

2.3 Data Processing

Considering the problems with classification before the late 1700s, measles and WC mortality data from the LBoM between 1750–1842 was used. Additionally, we joined the LBoM data with the data from the RGWR between 1842–1900. Even though the LBoM data was available until around 1845, the RGWR was more representative of true London disease mortality during this overlap as mentioned in Section 2.1. The time period used to analyze these diseases was also decided by that fact that previous studies have reported both diseases to be endemic in London starting in the 1700s [6, 30]. Weeks that were missing from the time series were identified manually, and linearly interpolated since the gaps were only between 1 to 3 weeks (Figure 1).

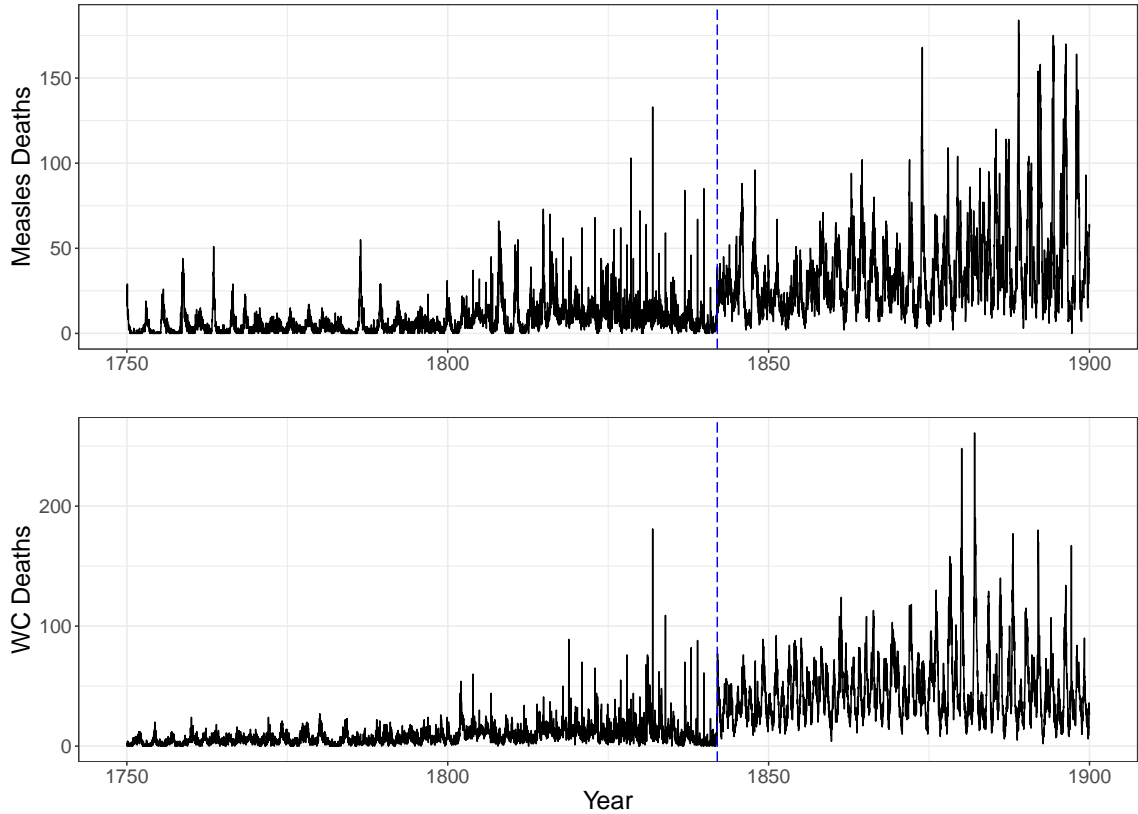


Figure 1: Weekly disease mortality of measles (top panel) and WC (bottom panel) in London, 1750–1900. Data from the LBoM was used between 1750–1842, and data from the RGWR was used between 1842–1900. The blue dashed line represents the year which the data switches from LBoM to RGWR. Missing weeks were linearly interpolated as gaps were at most three weeks.

The methodology of Krylova and Earn [4] was used to study the historical patterns of these diseases. To check the quality of the data, the weekly data was aggregated by year, then cross-validated with the annual disease mortality tabulated by Creighton [16] from the annual Bills of Mortality and Registrar General’s Returns. Creighton’s data was available from 1750 to 1837 for measles, and from 1750 to 1812 for WC. For the respective time intervals, the annual mortality data aligned well between both sources and showed little variation (Figure 2).

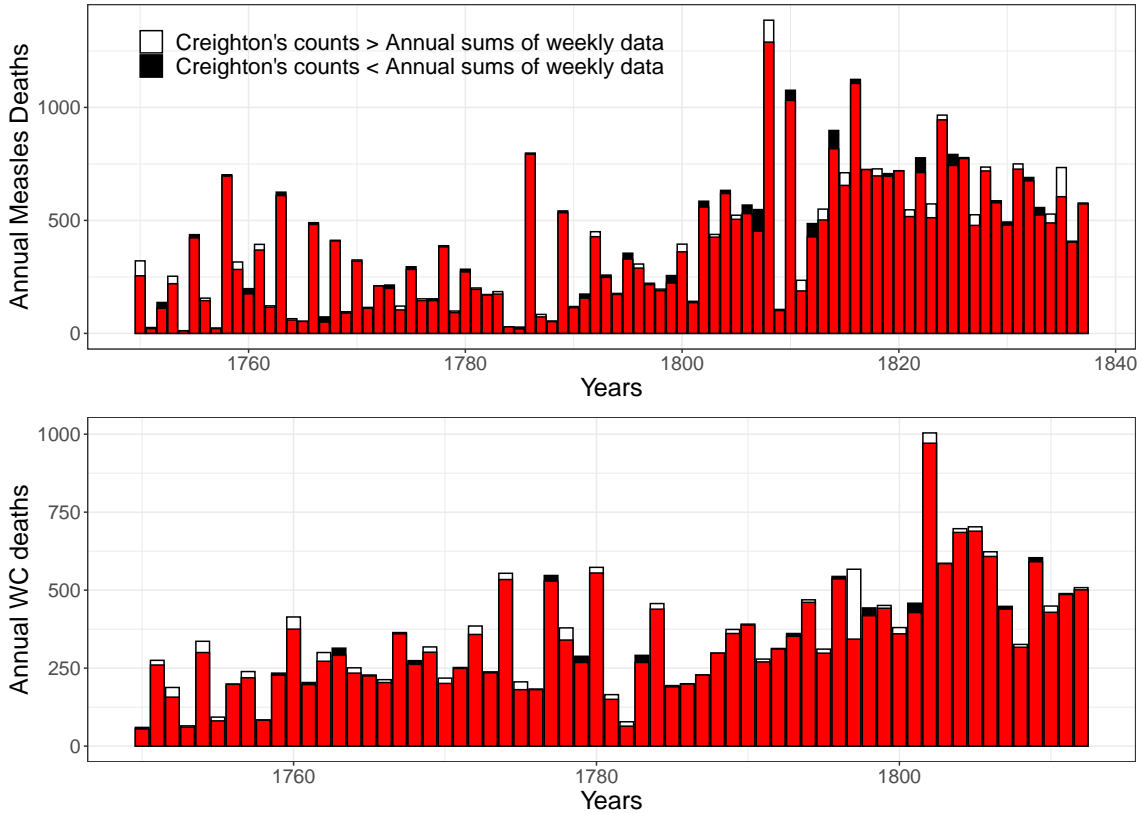


Figure 2: Validation of aggregated weekly disease mortality against Creighton’s annual tabulations [16]. White bars on the top means Creighton’s counts were larger, whereas black bars means the aggregated weekly sums were larger for that year. Data consistency was checked for both measles (top panel) and WC (bottom panel).

The weekly mortality series was then normalized to control for external factors that may have affected the observed trends, such as population growth, changes in geographic sample area, and changes in registration system [4]. It is reasonable to assume that these factors would have also affected the reporting of other causes of deaths in a similar way, so we first extracted the trend in all-cause mortality (ACM) using the EMD package in R [37, 38]. The package performs empirical mode decomposition (EMD), which is well-suited for breaking down nonlinear and nonstationary signals into intrinsic mode functions and an overall trend [38, 39]. The disease mortality time series was then divided by the ACM trend for normalization (Figure 3). Note that the ACM trends for the LBoM and RGWR sampling periods were calculated separately, as a huge jump in reported mortality was seen during this transition.

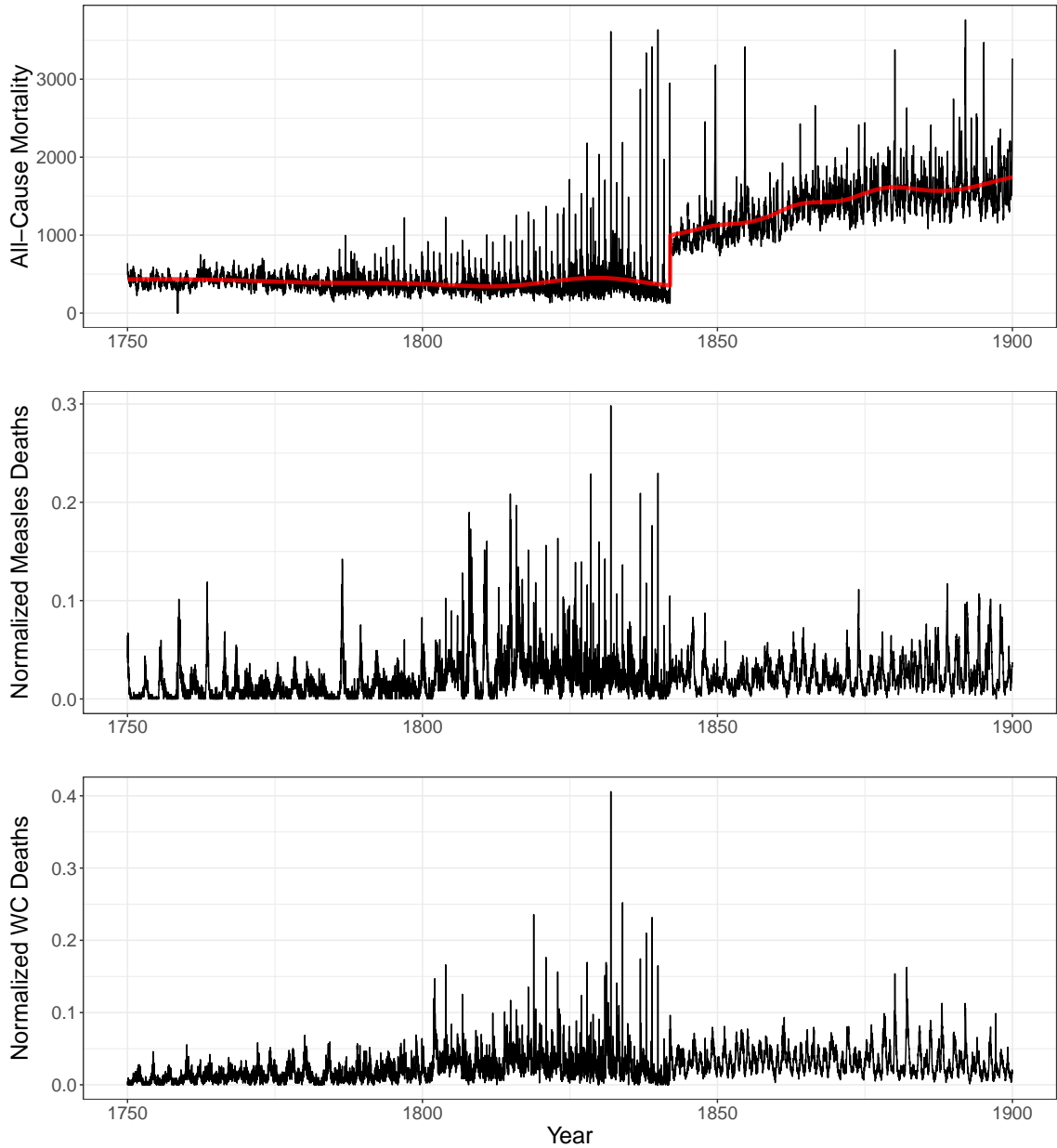


Figure 3: All-cause mortality and normalized weekly disease mortality of London, 1750–1900. Top panel shows the weekly all-cause mortality and the trend (red line) computed using empirical mode decomposition, as done previously by Krylova and Earn [4]. The weekly measles (middle panel) and WC (bottom panel) disease mortality was normalized by dividing by the trend in all-cause mortality.

2.4 Spectral Analysis

Both diseases exhibited recurrent epidemics, as repeated peaks were seen in the time series (Figure 1 & 3). However, the structure of these temporal patterns may differ between diseases and vary over time [40]. This is hard to observe using just the time series, so we used spectral methods to analyze the periodicity of measles and WC.

Spectral analysis involves decomposing a signal in terms of periodic functions such as sines and cosines. For example, the time series $\{x_t\}$ may be written as a Fourier series:

$$x_t = a_0 + \sum_{p=1}^{(N/2)-1} [a_p \cos(2\pi pt/N) + b_p \sin(2\pi pt/N)] + a_{N/2} \cos \pi t \quad (1)$$

for $t = 1, 2, \dots, N$ [41]. Usually, the Fourier transform of the correlogram, known as the periodogram, is computed

$$I(\omega_p) = \frac{1}{\pi} \left(r_0 + 2 \sum_{k=1}^{N-1} r_k \cos \omega_p k \right) \quad (2)$$

for $\omega_p = 2\pi p/N$ and $p = 1, \dots, N/2$ [40, 41]. This gives an estimate of the power spectral density function, revealing information about periodicities in the data that are hard to observe directly [40].

The period periodogram of the normalized, square-root-transformed mortality time series was computed to understand the global dominant periods. This was done through the `spec.pgram` function in R [37] which uses a fast Fourier transform with a standard modified Daniell smoother.

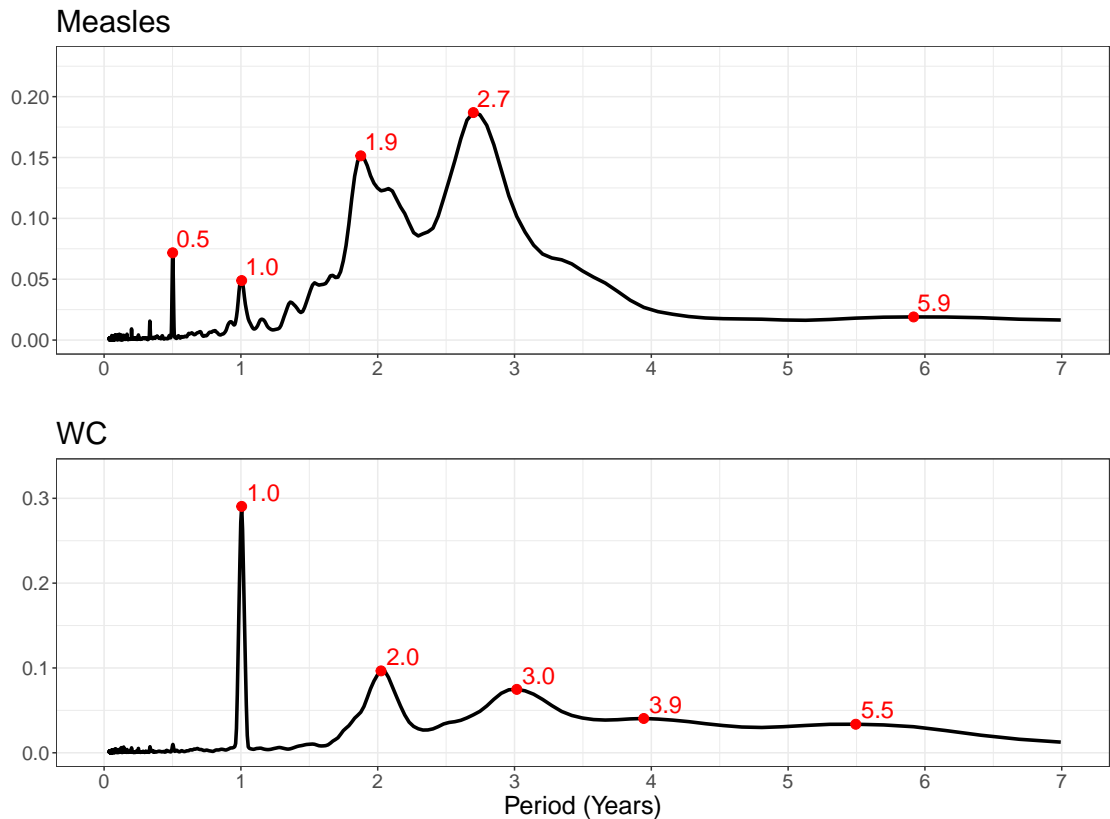


Figure 4: Periodogram of weekly measles and WC mortality time series in London, 1750–1900. The square-root-transformed normalized time series was used to calculate the periodograms for measles (top panel) and WC (bottom panel). Red points indicate prominent peaks in the periodogram.

Both periodograms showed a strong signal near 1 year indicating annual periodicity (Figure 4). This was likely due to seasonality of epidemics corresponding to yearly weather patterns or other seasonal factors (e.g., school terms) that influenced contact patterns [42]. Furthermore, measles showed peak signals near 0.5, 1.8, 2.7 and 5.9 years, whereas WC showed peaks near 2.0, 3.0, 3.9 and 5.5 years. Despite both being respiratory diseases that affect similar age groups [13], these diseases showed differing complex dynamics (as found for 20th century incidence data for these diseases [32]).

Although periodograms provide a useful overview of global patterns, they do not show how these recurring patterns change over time [40, 43]. Traditional spectral methods also assume the time series is stationary, which is usually not the case for epidemiological data [43]. To address these concerns, we generated the wavelet spectra of the disease mortality time series using the `WaveletComp` package in R [37, 44]. The wavelet transform decomposes signals over wavelet functions which can vary in width,

where narrower signals correspond to higher frequencies [4, 43, 45]. For a signal $x(t)$ and wavelet function $\psi(t)$, it is defined as

$$W_x(a, \tau) = \frac{1}{\sqrt{a}} \int_{-\infty}^{\infty} x(t) \psi^*((t - \tau)/a) dt \quad (3)$$

where a is the scaling factor and τ is the time shift, and gives the local wavelet power spectrum by $\|W_x(f, \tau)\|^2$ [43, 45]. The transform can roughly be interpreted as the correlation between a signal and a set of functions with different widths [45]. It also gives good localization of signals in the time-frequency domain with optimal trade-off in resolution [43, 45], making it better suited for spectral analysis. The `WaveletComp` package computes the wavelet transform using a Morlet wavelet for $\psi(t)$:

$$\psi(t) = \pi^{-1/4} \exp(i2\omega_0 t) \exp(-t^2/2) \quad (4)$$

where ω_0 is the central angular frequency [43, 44]. The package assessed the significance of signals by comparing against a white noise surrogate time series [44]. In the wavelet spectra, the cone of influence was included, which indicates areas near the edges where spectral information may be less accurate due to zero padding [43].

Early in the time series, measles showed strong signals near 3-year periods, which progressively shifted to 2-year periods over time (Figure 5). Signals at 1- and 0.5-year periods were also consistently present starting near 1870. Meanwhile, WC showed strong signals at 1-year periods throughout most of the time series. Peaks also varied greatly between 2- to 5-year periods before the late 19th century, suggesting multi-ennial dynamics. Starting in the late 19th century, signals at longer periods were localized near 2 and 3 years.

Overall, the spectral analysis that was performed describes the differing long term patterns of measles and WC. Not only could the information be used for future studies on measles and WC dynamics, but will be used as a reference when analyzing the dynamics of the IA model in Section 3 and Section 4.

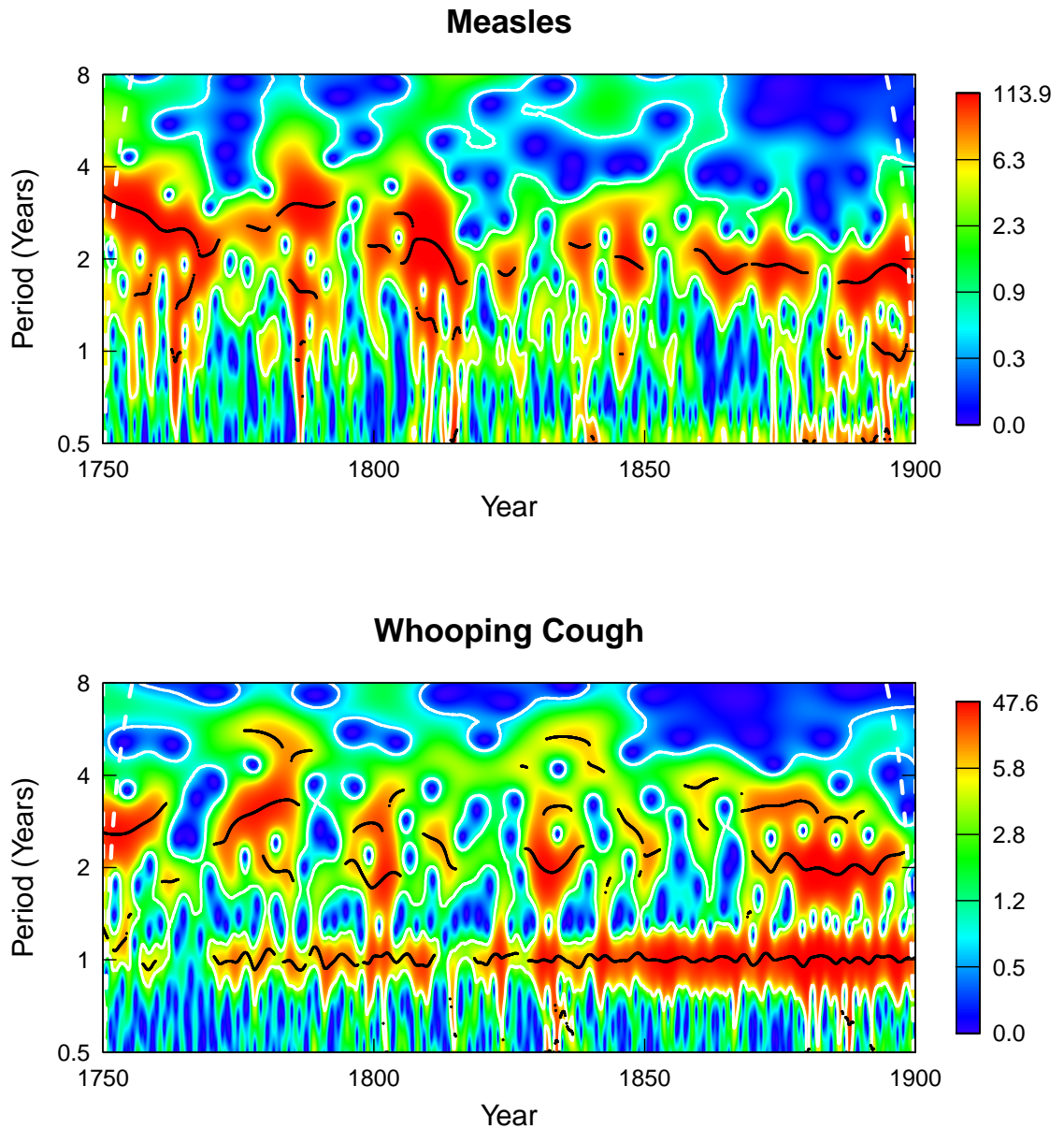


Figure 5: Wavelet spectrum of weekly measles and WC mortality time series in London, 1750–1900. The square-root-transformed normalized time series was used to calculate the wavelet spectra for measles (top panel) and WC (bottom panel). Black curves indicate local peaks in wavelet power, and white solid curves indicate 95% confidence contours. White dashed lines near the edges indicate the cone of influence.

3 Modelling Immune Amnesia

To investigate how measles-induced IA affects the dynamics of secondary infectious diseases, specifically with regards to recurrent epidemics, a two-disease model based on the SEIR model [40, 46] was constructed.

3.1 The SEIR Model

The SEIR model is commonly used when modelling an infectious disease within a population. It assumes that a host population can be divided into compartments based on the progression of an infection for an individual [40]:

- Susceptible (S) individuals who may become infected.
- Exposed (E) individuals who have been infected, but are not yet infectious themselves
- Infectious (I) individuals who can now transmit the infection to a susceptible individual
- Removed (R) individuals who have recovered and are now immune to the infection. This means that they cannot become infected nor spread the infection.

According to the above assumption, $N = S + E + I + R$ represents the total population size. The model also incorporates transition rates between the sequence of compartments as shown in Figure 6.

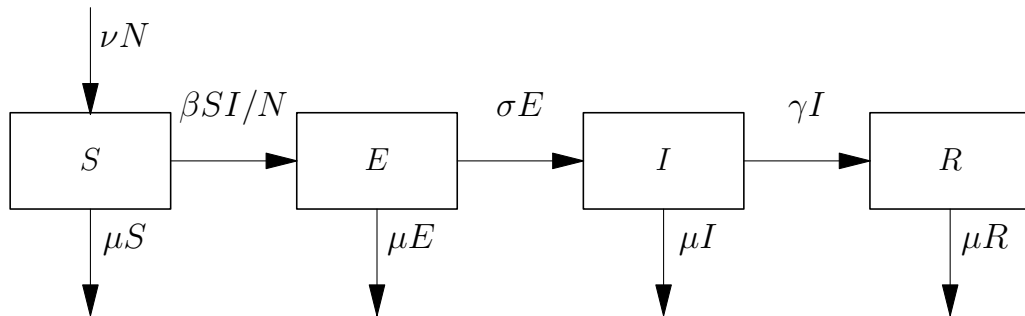


Figure 6: Flow diagram of SEIR model

β represents the transmission rate, or the average number of contacts between S and I individuals that lead to new infections per unit time per susceptible per infective. $1/\sigma$

and $1/\gamma$ represent the mean latent and infectious periods, respectively. The model may also incorporate vital statistics, specifically the *per capita* birth rate (ν) and natural death rate (μ).

If it is further assumed that the population is large and homogeneously mixed, a system of ordinary differential equations (ODEs) can be constructed to represent the rate of change in each compartment ¹:

$$\frac{dS}{dt} = \nu N - \frac{\beta SI}{N} - \mu S \quad (5a)$$

$$\frac{dE}{dt} = \frac{\beta SI}{N} - \sigma E - \mu E \quad (5b)$$

$$\frac{dI}{dt} = \sigma E - \gamma I - \mu I \quad (5c)$$

$$\frac{dR}{dt} = \gamma I - \mu R \quad (5d)$$

An important quantity when determining the potential spread of an infectious disease is the basic reproduction number (\mathcal{R}_0). It is defined as the average number of secondary cases generated by one infective individual introduced into a population of susceptibles [40, 48]. For the SEIR model, the formula for \mathcal{R}_0 is given by:

$$\mathcal{R}_0 = \frac{\nu}{\mu} \frac{\sigma}{\mu + \sigma} \frac{\beta}{\mu + \gamma} \quad (6)$$

[48]. Practically, \mathcal{R}_0 provides a threshold which dictates the trajectory of the disease. If $\mathcal{R}_0 < 1$, then the exposed and infectious population fades out and approaches a disease-free equilibrium. If $\mathcal{R}_0 > 1$, the disease persists and there exists an endemic equilibrium with nonzero exposed and infectious populations [40, 48].

Another common extension of the SEIR model is to account for seasonal changes in the transmission rate $\beta(t)$. However, it is difficult to exactly know the structure of $\beta(t)$. Even when contact patterns can be deduced, a representative function for $\beta(t)$ may include abrupt changes (e.g., $\beta(t)$ based on school term summarized in [49]), making analysis difficult. Hence, an approximation with a sinusoidal function is commonly used:

¹Note that in these equations N refers to $N(t)$, the total population size at time t . An alternative would be to use $N(t_0)$, where t_0 is an ‘‘anchor time’’ at which \mathcal{R}_0 is well estimated; see [47, §1.2].

$$\beta(t) = \langle \beta \rangle (1 + \alpha \cos(2\pi t)) \quad (7)$$

where $\langle \beta \rangle$ represents the mean transmission rate and α between 0 and 1 represents the seasonal forcing amplitude.

Papst and Earn [49] have shown that the sinusoidally-forced $\beta(t)$ with an appropriately chosen α can result in similar qualitative dynamics compared to other forcing functions of radically different shapes (e.g., school term-time forced $\beta(t)$). Hence, studying qualitative patterns in dynamics using eq. (7) is still relevant to epidemics in the real world.

3.2 The Two-Disease Immune Amnesia Model

We construct a two-disease IA model to study the dynamics of WC under the influence of measles-induced IA. Hypothetically, WC would have been influenced by IA as both diseases affect similar age groups, and there exists historical records of their association [13, 16].

A flow diagram of the IA model is shown in Figure 7. For state variables with two-letter subscripts, the first letter represents the stage of infection for measles, while the second letter represents the stage of infection for WC. Along with the assumptions for the SEIR model, the IA model assumes that an individual recovers from one disease before becoming susceptible once again to another disease. Individuals infected with both diseases were likely rare in comparison due to relatively short recovery periods [12]. Furthermore, co-infection of both diseases may be hindered by ecological interference, such as convalescence where infected individuals self-isolate and are shielded from exposure to other diseases [50].

From the X_{SS} compartment, the left path represents those who first had measles before WC, whereas the right path represents those who had WC before measles. However, individuals from the right path may become susceptible to WC again after measles infection due to IA, and this is represented by a separate X_A compartment (A for amnesia). θ is the proportion of measles-recovered individuals who experience IA as measles may compromise WC immunity to varying degrees. $1/\kappa$ describes the mean duration of reduced immunity experienced due to IA. We refer to θ and $1/\kappa$ as **IA strength** and **IA duration** respectively throughout the thesis.

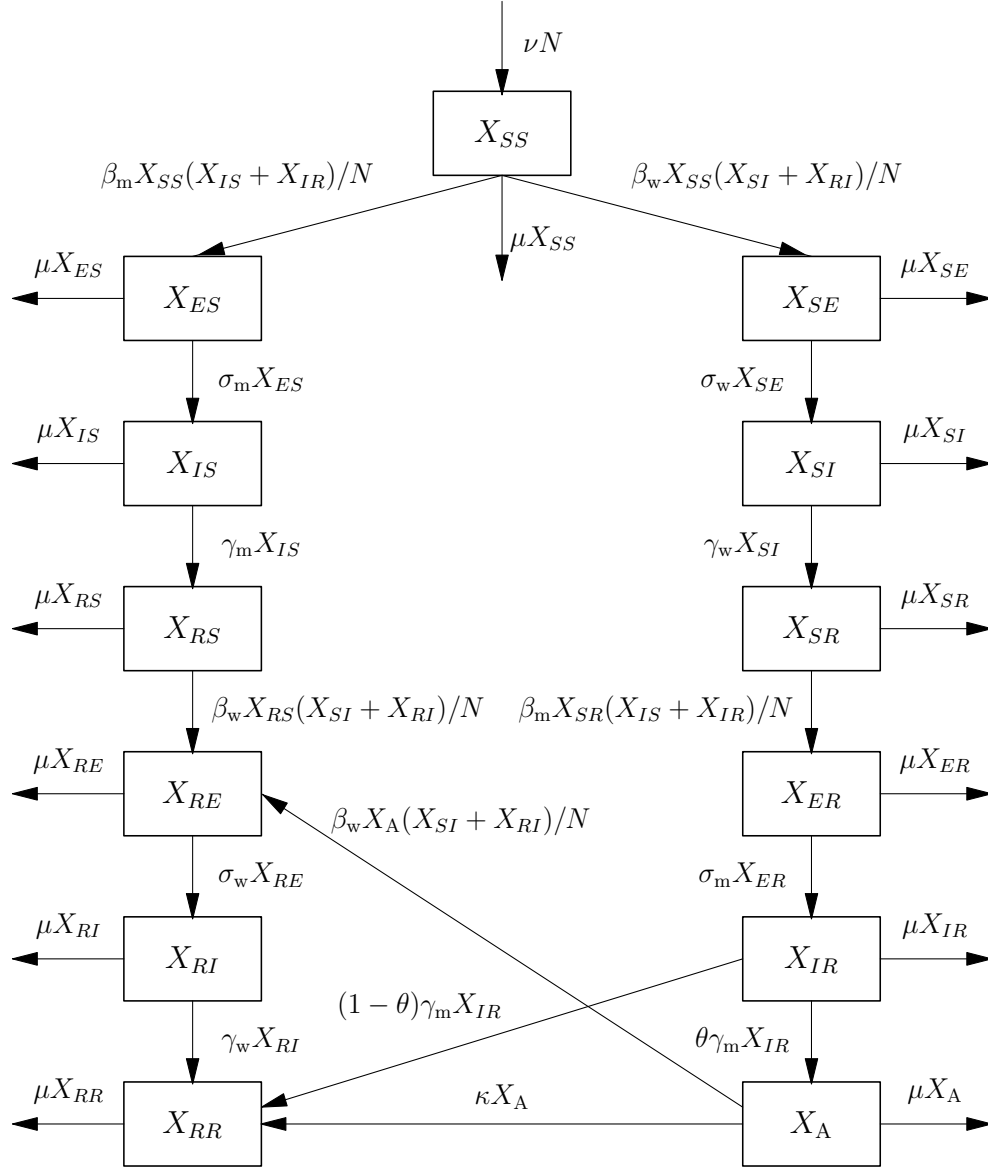


Figure 7: Flow diagram of the two-disease immune amnesia model. For two-letter compartments, the first letter represents the stage in measles infection, and the second letter represents the stage in WC infection. The X_A compartment represents those with decreased immunity to WC due to measles-induced immune amnesia. Parameters with subscript m are those pertaining to measles, and subscript w are those pertaining to WC.

With these considerations, we can construct a system of ODEs for the IA model. Note that the total number of infectious individuals for measles and WC are denoted as $I_m = X_{IS} + X_{IR}$ and $I_w = X_{SI} + X_{RI}$ respectively.

$$\frac{dX_{SS}}{dt} = \nu N - \frac{\beta_m I_m X_{SS}}{N} - \frac{\beta_w I_w X_{SS}}{N} - \mu X_{SS} \quad (8a)$$

$$\frac{dX_{SE}}{dt} = \frac{\beta_w I_w X_{SS}}{N} - \sigma_w X_{SE} - \mu X_{SE} \quad (8b)$$

$$\frac{dX_{SI}}{dt} = \sigma_w X_{SE} - \gamma_w X_{SI} - \mu X_{SI} \quad (8c)$$

$$\frac{dX_{SR}}{dt} = \gamma_w X_{SI} - \frac{\beta_m I_m X_{SR}}{N} - \mu X_{SR} \quad (8d)$$

$$\frac{dX_{ER}}{dt} = \frac{\beta_m I_m X_{SR}}{N} - \sigma_m X_{ER} - \mu X_{ER} \quad (8e)$$

$$\frac{dX_{IR}}{dt} = \sigma_m X_{ER} - \gamma_m X_{IR} - \mu X_{IR} \quad (8f)$$

$$\frac{dX_{ES}}{dt} = \frac{\beta_m I_m X_{SS}}{N} - \sigma_m X_{ES} - \mu X_{ES} \quad (8g)$$

$$\frac{dX_{IS}}{dt} = \sigma_m X_{ES} - \gamma_m X_{IS} - \mu X_{IS} \quad (8h)$$

$$\frac{dX_{RS}}{dt} = \gamma_m X_{IS} - \frac{\beta_w I_w X_{RS}}{N} - \mu X_{RS} \quad (8i)$$

$$\frac{dX_{RE}}{dt} = \frac{\beta_w I_w (X_{RS} + X_A)}{N} - \sigma_w X_{RE} - \mu X_{RE} \quad (8j)$$

$$\frac{dX_{RI}}{dt} = \sigma_w X_{RE} - \gamma_w X_{RI} - \mu X_{RI} \quad (8k)$$

$$\frac{dX_A}{dt} = \theta \gamma_m X_{IR} - \frac{\beta_w I_w X_A}{N} - \kappa X_A - \mu X_A \quad (8l)$$

$$\frac{dX_{RR}}{dt} = \gamma_w X_{RI} + \kappa X_A + (1 - \theta) \gamma_m X_{IR} - \mu X_{RR} \quad (8m)$$

3.3 The Adaptive Tau Algorithm

When simulating epidemiological models, one consideration that arises is whether to include noise, such as demographic stochasticity. Initial work by Barlett [51] showed that the introduction of noise can sustain oscillations in a stochastic model. In fact, noise may sustain transient oscillations at a period different from an attractor [40], and better explain the dynamics of some diseases such as WC [32, 33]. Furthermore, demographic stochasticity recognizes the discrete nature of populations during simulations.

A simple way of incorporating demographic stochasticity to compartmental models is

by using Gillespie's stochastic simulation algorithm (SSA) [40, 52, 53]. Let a_j be the rate at which a process involving a change in state occurs, and let $a_0 = \sum a_j$ be the sum of the rates associated with the current system. Then, the probability that an event associated with rate a_j occurs in a small time interval $[t, t + dt)$ is $a_j dt$. The time at which the next event occurs is given by $t + \tau$ with $\tau = \frac{1}{a_0} \ln(1/u)$, where u is sampled from a uniform distribution on $(0, 1)$. The associated i th event that occurs is selected by generating a point a_r from a uniform distribution on $(0, a_0)$ and finding the smallest integer i such that $\sum_{l=1}^i a_l > a_r$. Despite this algorithm providing correct realizations of stochastic processes that may occur, it is very slow since only one event occurs at each time step [53].

To improve computational efficiency, Gillespie also proposed tau-leaping methods to accelerate SSA [53, 54]. Specifically, the number of times an event occurs between $[t, t + \tau)$ is approximated by a Poisson random variable $P(a_j \tau)$ for a small enough τ . A value k_j is then sampled from this distribution for the j th process, and the current state is updated by $k_j v_j$ for all possible processes where v_j represents the state change that occurs [53]. This is analogous to the explicit Euler formula, meaning it also suffers from similar concerns such as the selection of a suitable τ , potential to drive certain populations to negative values, and inefficient handling of stiff problems [53]. Stiffness is a major concern as the taken step size when using explicit methods needs to be restricted to maintain numerical stability, but may lead to significantly longer computational time [53]. To address this, implicit tau-leaping methods and different tau selection algorithms have been proposed. However, it is difficult to determine which method to use without initial knowledge about the system. Cao *et al.* [53] proposed an adaptive tau-leaping algorithm that chooses either a non-negative explicit or implicit method, by comparing the calculated τ 's of each method to determine if the problem is stiff or not for that timestep. Since we do not know whether our system is stiff and the adaptive tau method can perform simulations faster than regular SSA or explicit tau-leaping methods [53], this method was used to simulate the IA model.

3.4 Methods

Stochastic simulations of the IA model with seasonal forcing were performed using the `adaptivetau` package in R [37, 55]. The parameter values that were used are summarized in Table 1, and the state changes are summarized in Table 2.

Parameter	Measles	WC
Mean latent period ($1/\sigma$)	8 days	8 days
Mean infectious period ($1/\gamma$)	5 days	14 days
<i>Per capita</i> birth rate & natural death rate (ν, μ)	0.02 year ⁻¹	
Basic reproduction number (\mathcal{R}_0)	17	17
Mean transmission rate ($\langle\beta\rangle$)	Calculated using eq. (6) (\mathcal{R}_0 for the SEIR model)	
Seasonal forcing amplitude (α)	0.1	0.1
Initial population size (N)	800000	
Immigration rate (η)	0.00005 year ⁻¹	
IA strength (θ) & duration ($1/\kappa$)	Varied for different simulations	

Table 1: Parameters used in stochastic simulations unless specified otherwise.

Event	Change	Rate
Exposure	$(X_{SZ}, X_{EZ}) \rightarrow (X_{SZ} - 1, X_{EZ} + 1)$	$\beta_m I_m X_{SZ}/N$
	$(X_{ZS}, X_{ZE}) \rightarrow (X_{ZS} - 1, X_{ZE} + 1)$	$\beta_w I_w X_{ZS}/N$
	$(X_A, X_{RE}) \rightarrow (X_A - 1, X_{RE} + 1)$	$\beta_w I_w X_A/N$
Infection	$(X_{EZ}, X_{IZ}) \rightarrow (X_{EZ} - 1, X_{IZ} + 1)$	$\sigma_m X_{EZ}$
	$(X_{ZE}, X_{ZI}) \rightarrow (X_{ZE} - 1, X_{ZI} + 1)$	$\sigma_w X_{ZE}$
Recovery	$(X_{IS}, X_{RS}) \rightarrow (X_{IS} - 1, X_{RS} + 1)$	$\gamma_m X_{IS}$
	$(X_{IR}, X_{RR}) \rightarrow (X_{IR} - 1, X_{RR} + 1)$	$(1 - \theta)\gamma_m X_{IR}$
	$(X_{ZI}, X_{ZR}) \rightarrow (X_{ZI} + 1, X_{ZR} + 1)$	$\gamma_w X_{ZR}$
Immune amnesia	$(X_{IR}, X_A) \rightarrow (X_{IR} - 1, X_A + 1)$	$\theta\gamma_m X_{IR}$
Immune restoration	$(X_A, X_{RR}) \rightarrow (X_A - 1, X_{RR} + 1)$	κX_A
Birth	$X_{SS} \rightarrow X_{SS} + 1$	νN
Death	$X_Y \rightarrow X_Y - 1$	μX_Y
Immigration	$X_{IZ} \rightarrow X_{IZ} + 1$	ηN
	$X_{ZI} \rightarrow X_{ZI} + 1$	ηN

Table 2: List of state changes and rates in stochastic simulations of the IA model. $Z = S$ or R , and Y represents any compartment in the model.

The IA strength ($\theta \in [0, 1]$) and duration ($1/\kappa \in [0 \text{ months}, 24 \text{ months}]$) were varied for the same set of parameters to investigate their effect on overall epidemic patterns. Simulations were also carried out after varying the initial total population size, seasonal forcing amplitude, and mean transmission rate to investigate how these parameters influence the effect IA has on WC patterns.

An immigration term that introduces a small number of infectious individuals to the system was included, preventing the disease from fading out. This also reflected the high immigration to London that occurred during the time periods which we

focus on [36]. The immigration rate was chosen manually such that the diseases consistently persisted in multiple simulations. In the simulations, the calculated rate of immigration (ηN) with the parameter values used was small compared to the unforced incidence rates ($\langle\beta\rangle SI$) of the associated SEIR model at endemic equilibrium for both diseases.

A total of 30 realizations were run for each set of parameters. For each realization, we ran the simulation for 100 years initially to ensure that the system was near a stationary state, then simulation data from the next 200 years were used for spectral analysis. Using a long time series aimed to prevent spurious peaks [41], and avoid aliasing where frequencies within the sampled time series may be captured at another frequency in the power spectrum [41, 56].

To construct a weekly disease incidence time series from these simulations, an accumulator compartment was included for each disease to keep track of the number of new infectious individuals that entered the respective compartments. As the time steps for the adaptive tau algorithm were not constant, we assumed the state was constant between τ -leaps to get an evenly-spaced weekly time series of the accumulator compartment. Finally, taking the first difference of the accumulator series gave an incidence series reflected by the model (Figure 8). For future comparisons, we assumed that the disease incidence from simulations was roughly proportional to disease mortality from the real data.

Similar to how the disease mortality time series were normalized in Section 2.3, the simulated incidence time series was normalized by dividing by the EMD trend. Then, the square-root transform was applied to the normalized time series before calculating the period periodogram. The average periodogram and the 95% confidence interval of the 30 realizations were calculated for each set of parameters.

3.5 Results

Initially, along with parameters from Table 1, an initial population size of $N = 8 \times 10^5$ was used, which is close to the population of London in the late 18th century [4]. With no measles-induced IA, the average periodogram for measles showed peaks near 1 and 2 years, while WC showed peaks near 1 year and in between 2.5–3 years (Figure 9). The periodogram for measles did not show significant changes when IA was introduced to the system as expected (Figure 10 & Appendix B.1). However, for WC, we observed a new peak at around 2 years, while the signal for the peak between 2.5–3 years decreased (Figure 9 & Appendix B.1). This shift in peak signal was greater when the IA duration increased, and the shift was more prominent for shorter IA durations when IA strength increased (Figure 11, Appendix B.1). With high IA strength and duration, the magnitude of the new peak at around 2 years in the WC periodogram

became comparable to the 2-year peak in the measles periodogram (Figure 10, 11, Appendix B.1). Interestingly, the signal at 1 year did not change greatly for the WC periodogram across different IA parameters. This suggests that the seasonality of the disease is not overwhelmed by the effects of IA, and IA affects longer periodicities and more complex dynamics.

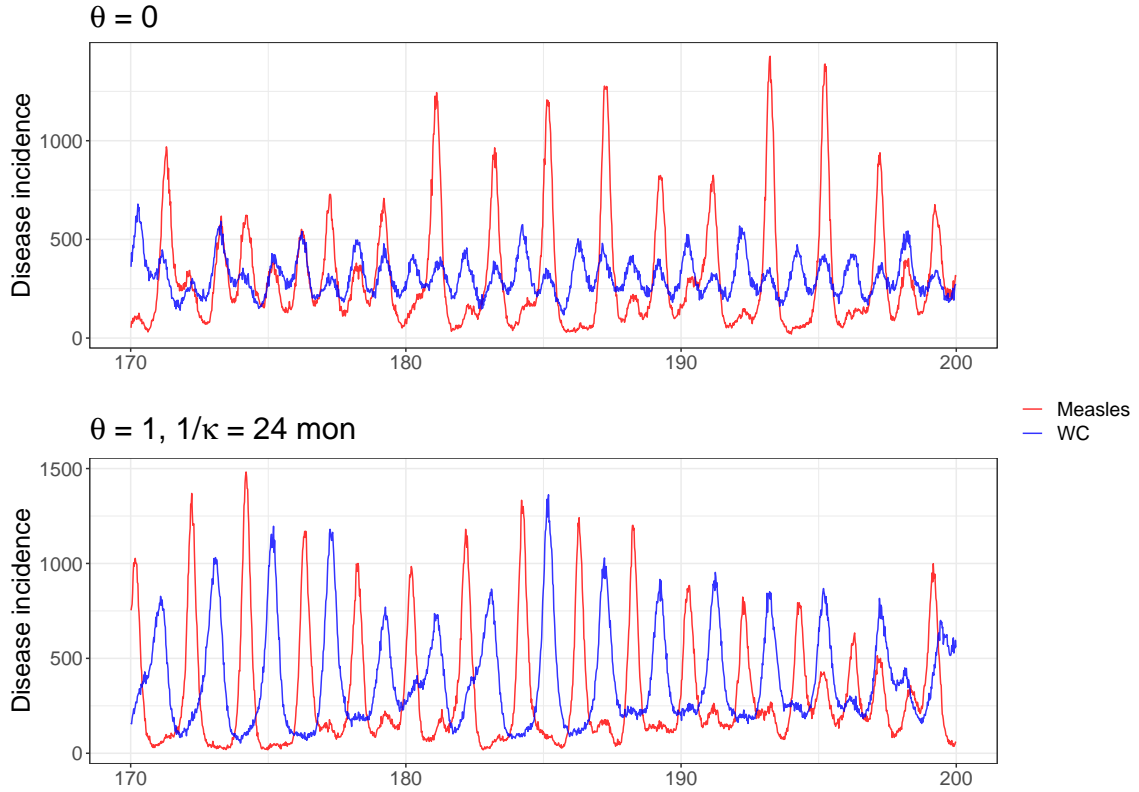


Figure 8: Disease incidence time series generated from one realization of the stochastic IA model. Model parameters from Table 1 were used. The calculated weekly incidence of measles (red) and WC (blue) for one stochastic simulation of IA model with no IA effects ($\theta = 0$, top panel) and strong IA effects ($\theta = 1, 1/\kappa = 24 \text{ mon}$, bottom panel) are shown.

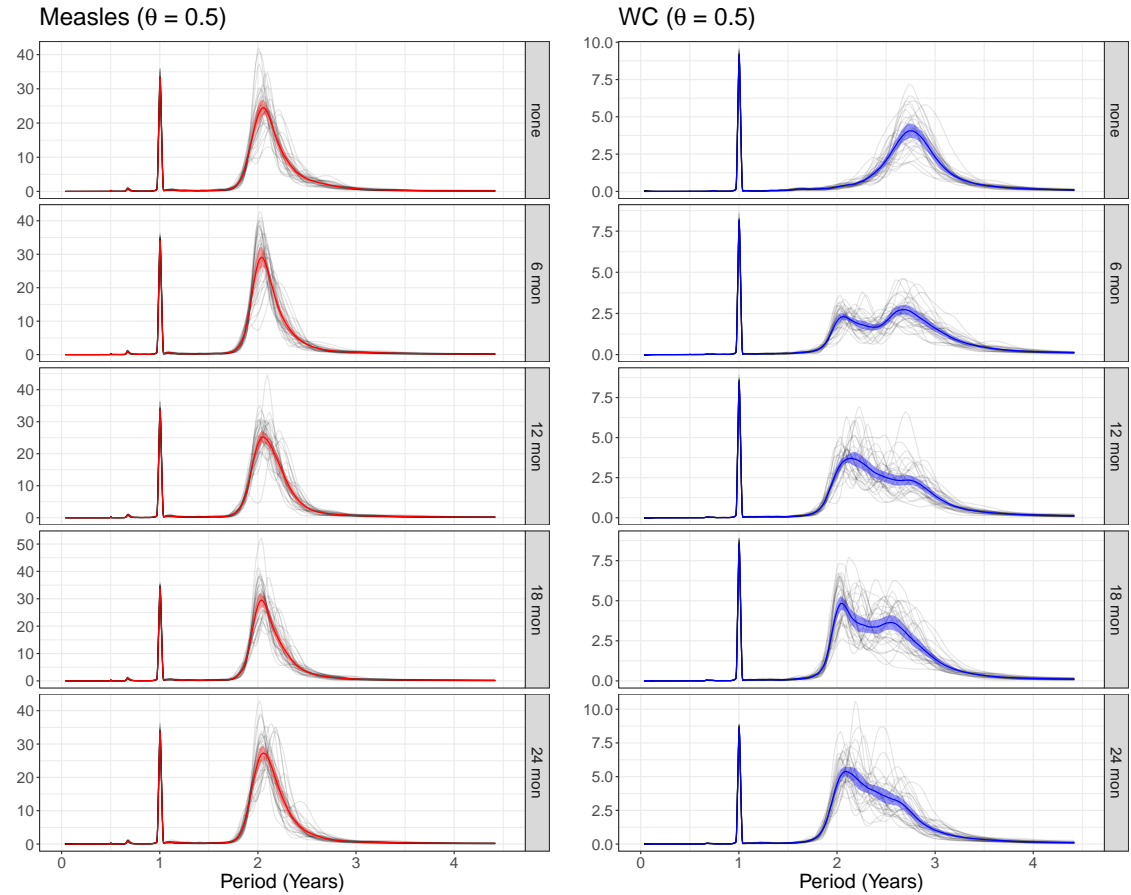


Figure 9: Power spectra of disease incidence generated from IA model with $N = 8 \times 10^5$ and $\theta = 0.5$. Power spectra were computed using the square-root-transformed normalized measles (left panels, red) and WC (right panels, blue) incidence weekly series extracted from stochastic simulations of IA model with fixed $\theta = 0.5$ (IA strength) and different $1/\kappa$ (IA duration) between 6 to 24 months. The top panels represent simulations with no IA effects ($\theta = 0$). Grey lines represent the power spectra of 30 different realizations, while solid colored lines indicate the average periodogram and colored bands represent 95% confidence intervals.

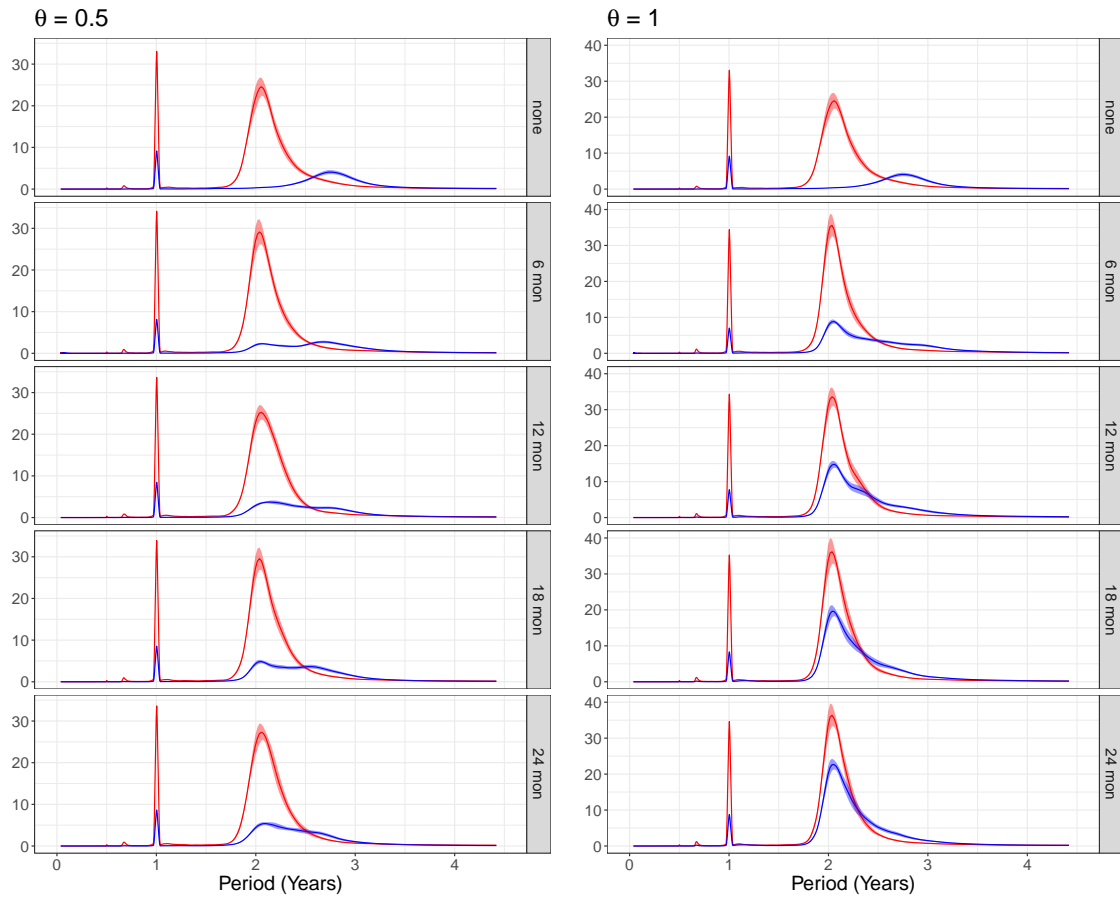


Figure 10: Average power spectra of disease incidence generated from IA model with $N = 8 \times 10^5$ and $\theta = 0.5, 1$. Power spectra were computed using the square-root-transformed normalized measles (red) and WC (blue) incidence weekly series extracted from stochastic simulations of IA model with fixed IA strength $\theta = 0.5$ (left) and 1 (right), and different $1/\kappa$ (IA duration) between 6 to 24 months. The top panels represent simulations with no IA effects ($\theta = 0$). Solid colored lines indicate the average periodogram and colored bands represent 95% confidence intervals.

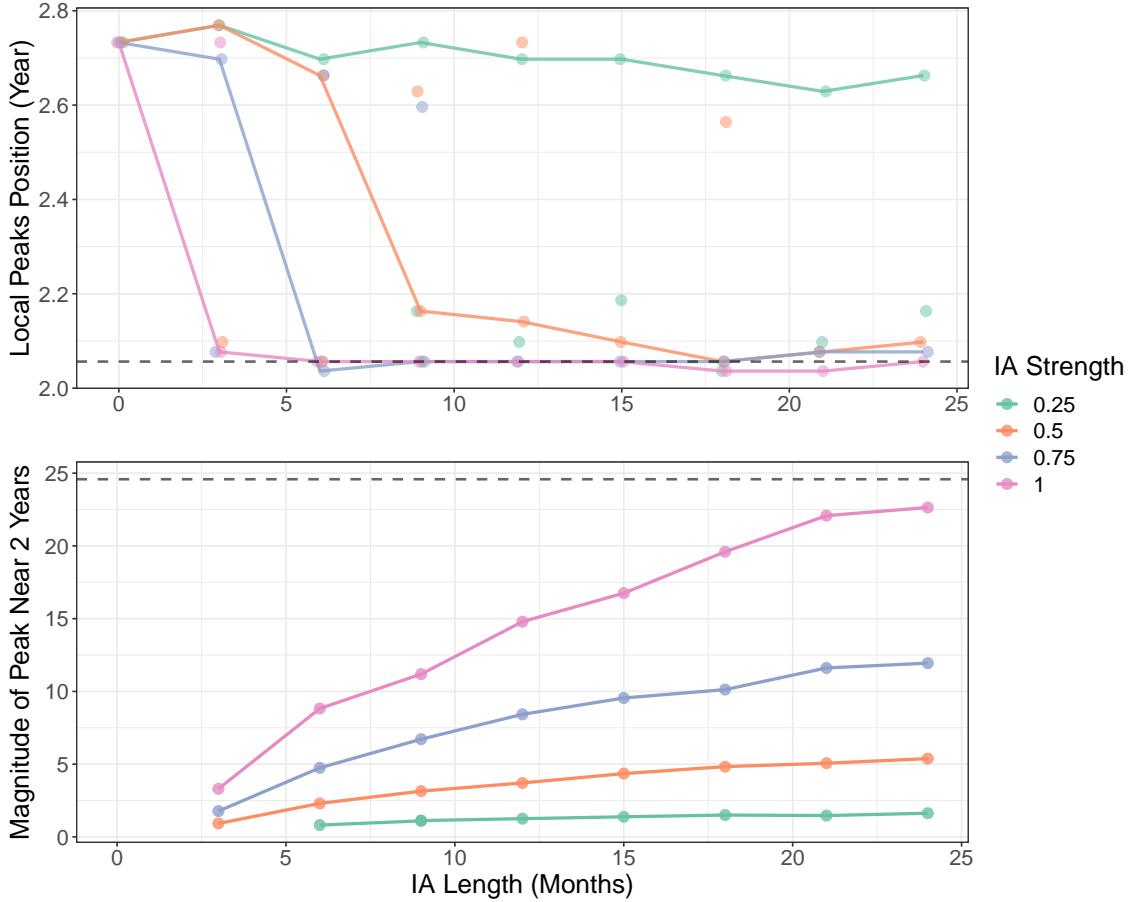


Figure 11: Longer period spectral structure of WC periodogram from the IA model using $N = 8 \times 10^5$ with varying θ and $1/\kappa$. Power spectra were computed using the square-root-transformed normalized WC incidence weekly series extracted from stochastic simulations of IA models. The top panel shows the locations of the peaks in the average periodogram of 30 realizations between 2 and 3 years. The points connected by the bold line represent the highest peak between this range for the associated pair of IA strength and duration, and points not connected by this line represent other local peaks of lower magnitude that were observed. The bottom panel shows the magnitude of the peak near 2 years in the WC periodogram. In both panels, the dotted line represents the characteristics of the peak near 2 years in the measles periodogram with no IA effects.

One disadvantage of using a periodogram to analyze a time series is that different temporal patterns in periodicities may lead to the same traditional periodogram [43]. Hence, to get a better picture of the temporal patterns in WC dynamics, the WC wavelet spectrum was computed for one realization of simulations with no IA ($\theta = 0$), weaker IA ($\theta = 0.5$, $1/\kappa = 6$ months), and stronger IA effects ($\theta = 1$, $1/\kappa = 24$ months). The WC wavelet spectrum with no IA effects mainly showed a strong signal

at around 3 years throughout time. However, when IA was introduced, the spectrum frequently showed regions with peak signals near both 2 and 3 years (Figure 12). These coexisting signals were analogous to the ones observed in the wavelet spectrum of weekly WC mortality in London, especially during the latter half of the 19th century (Figure 5). Note that these patterns were also regularly observed in other realizations.

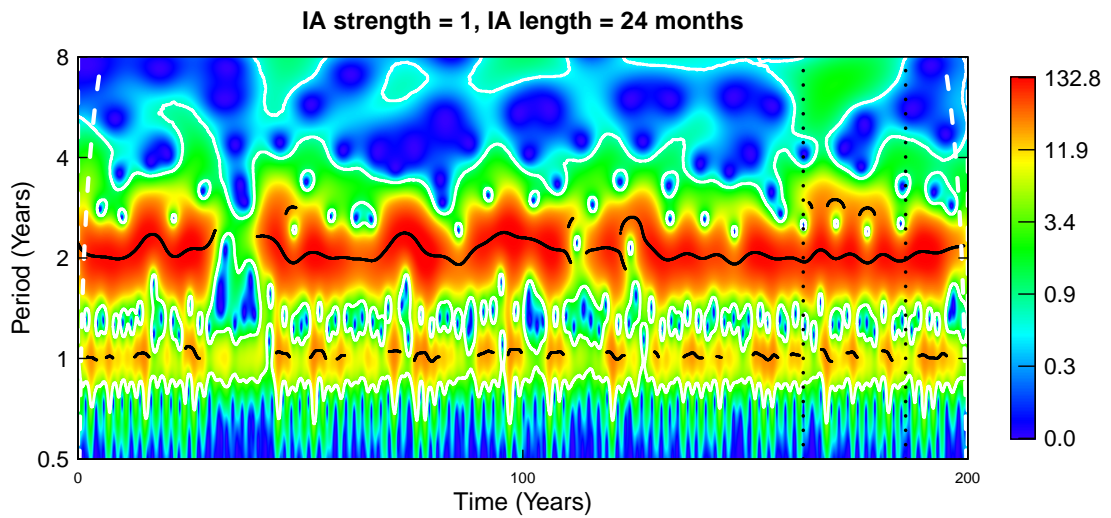
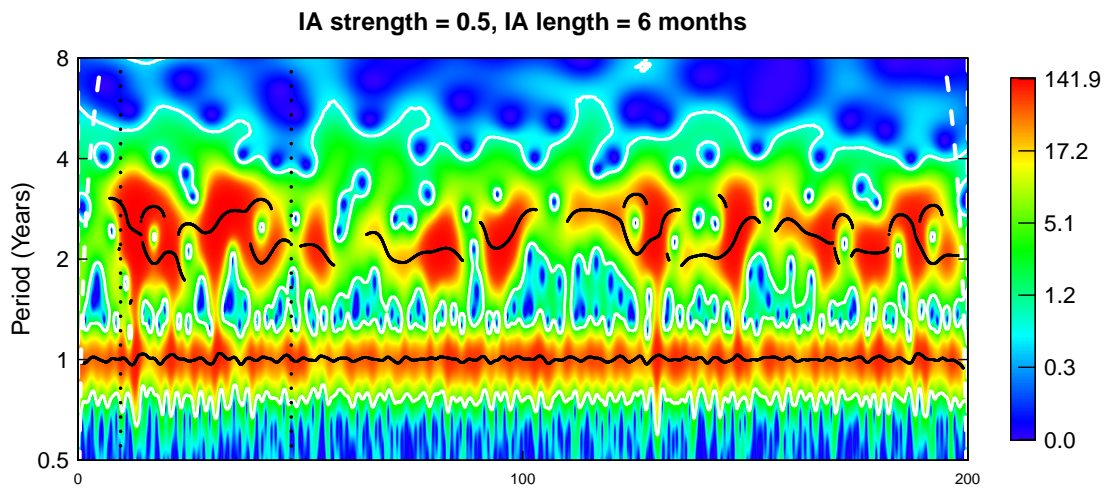
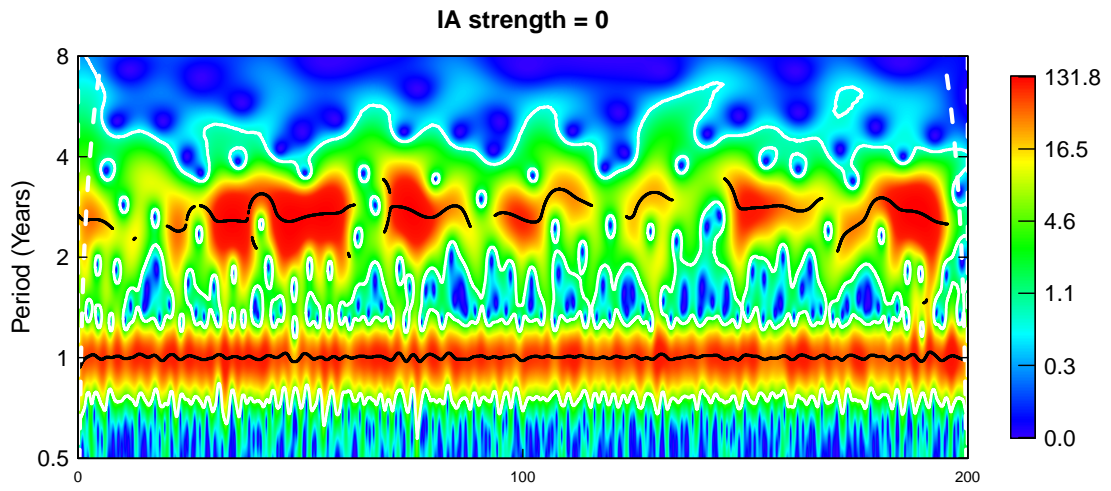


Figure 12: Wavelet spectra of WC weekly incidence from stochastic simulations with $N = 8 \times 10^5$. The wavelet spectra of the square-root-transformed normalized WC weekly incidence series were calculated for one realization of three simulated scenarios: no IA effects ($\theta = 0$), weak IA effects ($\theta = 0.5$, $1/\kappa = 6$ months), and strong IA effects ($\theta = 1$, $1/\kappa = 24$ months). Solid black curves indicate local peaks in wavelet power, and white solid curves indicate 95% confidence contours. White dashed lines near the edges indicates the cone of influence. Portions of the wavelet spectra between the black dotted lines display coexisting signals near 2- and 3-year periods.

As population size determines the magnitude of demographic stochasticity, and has been found to result in different qualitative features in the power spectra [57, 32, 56, 58], the same simulations were done using $N = 2.5 \times 10^6$. This reflects the approximate population of London in the late 19th century [4]. Despite sharper peaks, the observed trends for this population size were similar to that of $N = 8 \times 10^5$. With increasing IA strength and duration, the signal of the peak between 2.5–3 years decreased for the WC periodogram, whereas the peak around 2 years increased to almost match the signal in the measles periodogram (Figure 13, Appendix B.2). Meanwhile, the measles periodogram, and the signal at 1 year in the WC periodogram remained unaffected.

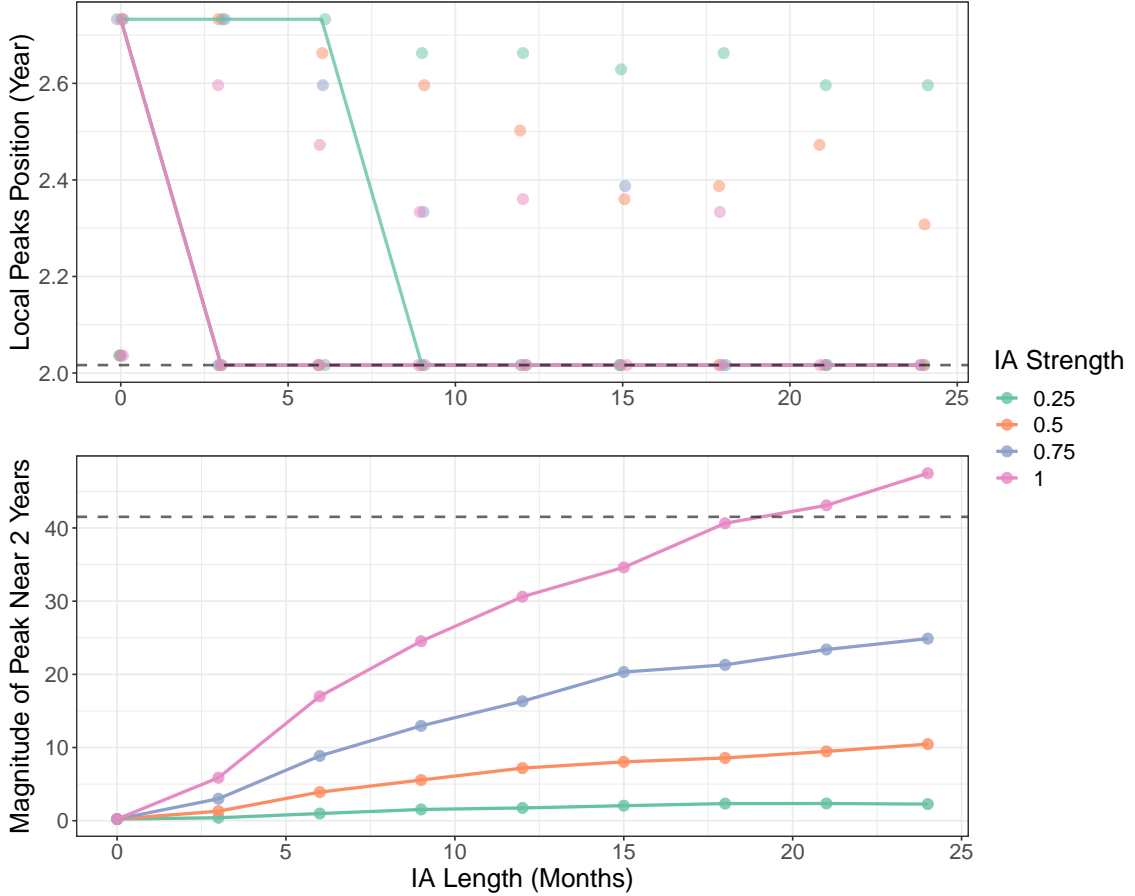
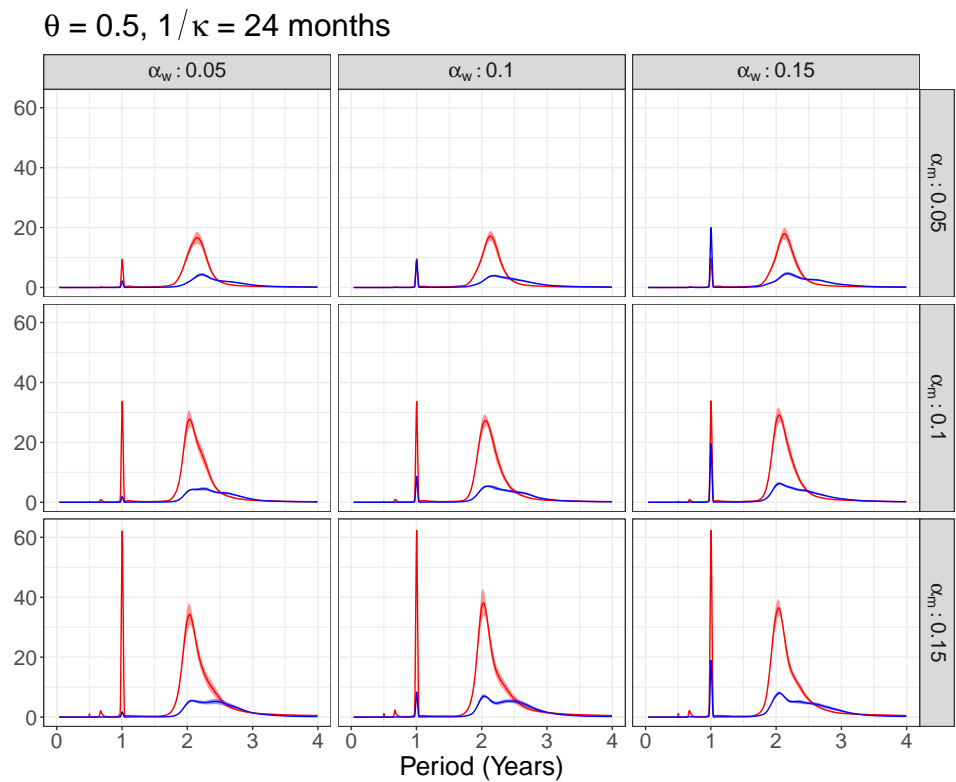
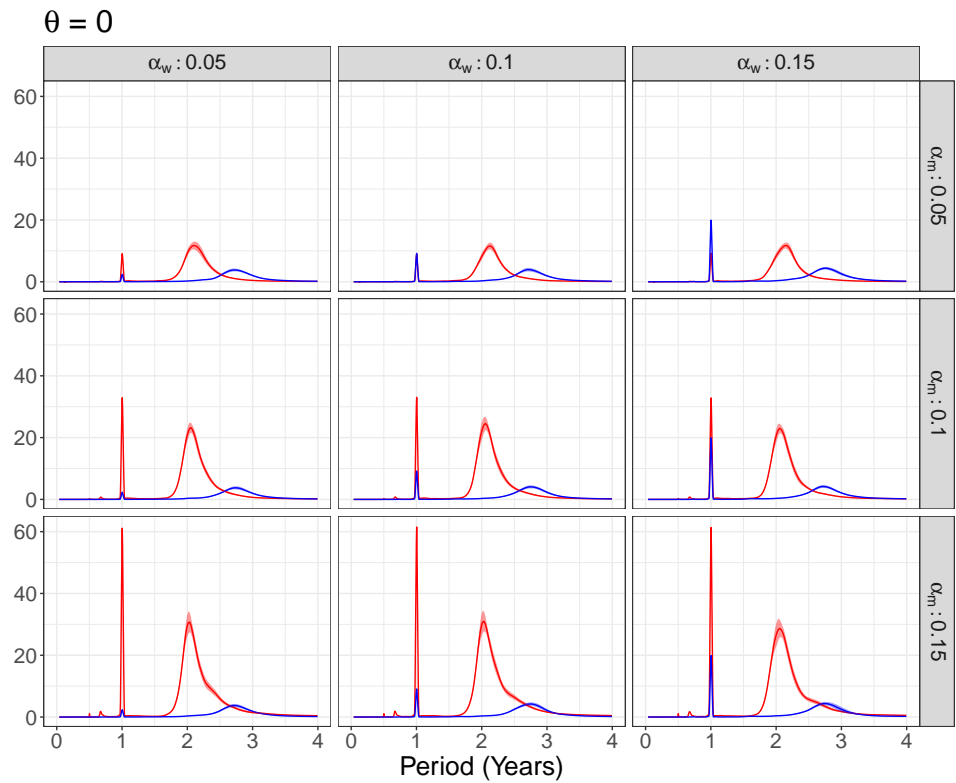
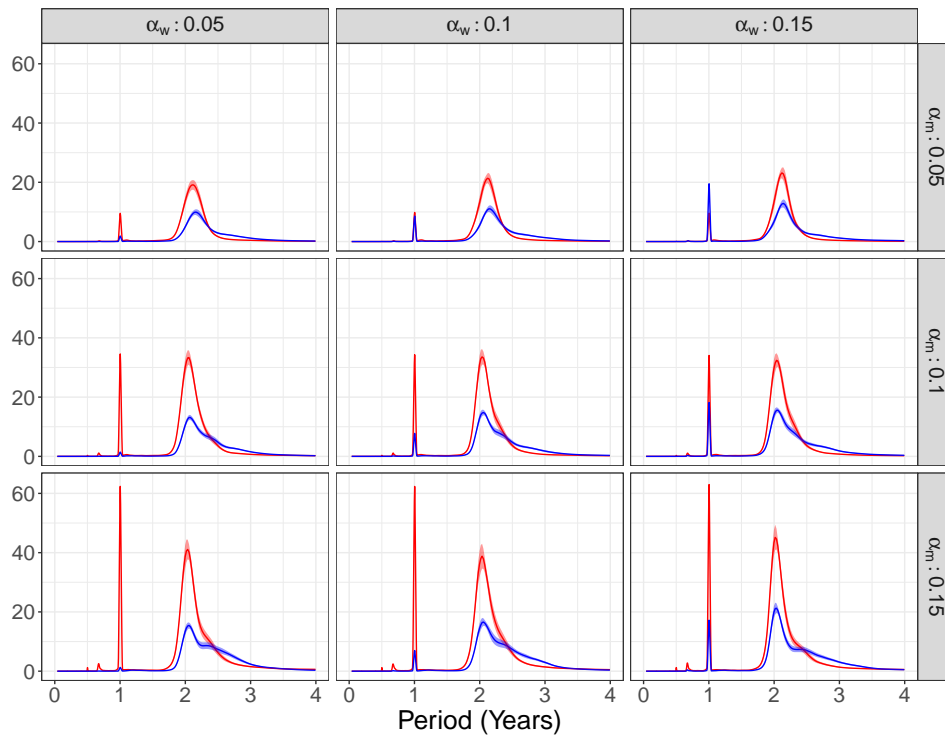


Figure 13: Longer period spectral structure of WC periodogram from the IA model using $N = 2.5 \times 10^6$ with varying θ and $1/\kappa$. Power spectra were computed using the square-root-transformed normalized WC incidence weekly series extracted from stochastic simulations of IA models. The top panel shows the peaks of the average periodogram of 30 realizations between 2 and 3 years. The points connected by the bold line represent the highest peak between this range for the associated pair of IA strength and duration, and points not connected by this line represent other local peaks of lower magnitude that were observed. The bottom panel shows the magnitude of the peak near 2 years in the WC periodogram. In both panels, the dotted line represents the characteristics of the 2-year peak in the measles periodogram with no IA effects.

Up to now, we assumed that the seasonal forcing amplitude for both diseases was 0.1. However, stochastic simulations using different seasonal forcing amplitudes [32, 59] have been found to result in different qualitative features in the power spectra. To investigate whether this would influence the patterns that were observed, simulations were run with $N = 8 \times 10^5$ for different pairs of seasonal forcing amplitudes where $\alpha_m, \alpha_w \in [0.05, 0.1, 0.15]$.



$\theta = 1, 1/\kappa = 12$ months



$\theta = 1, 1/\kappa = 24$ months

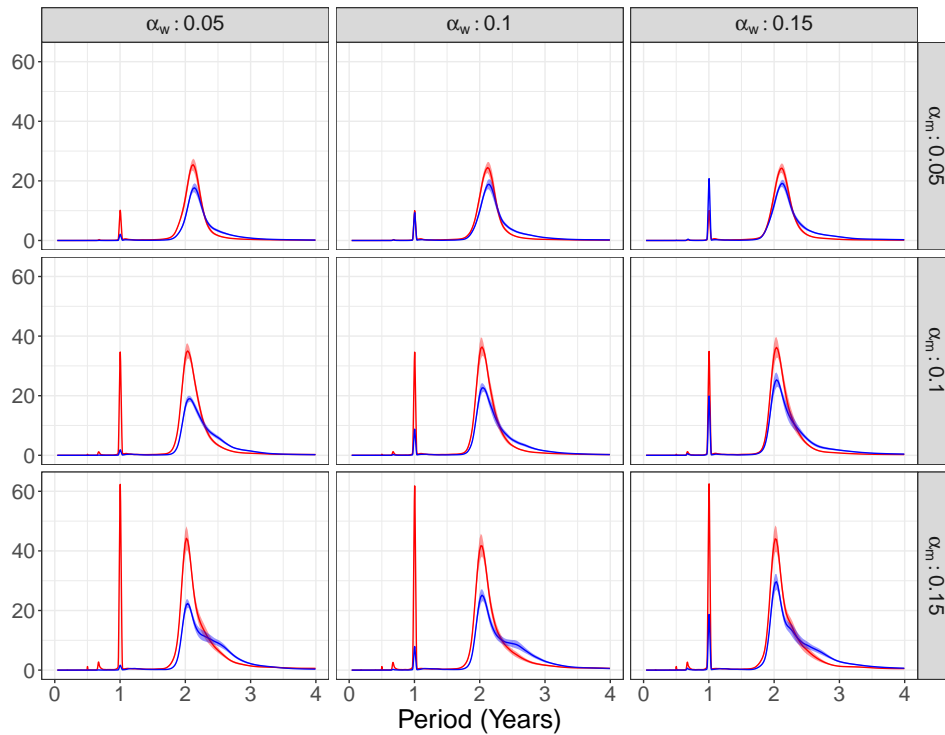


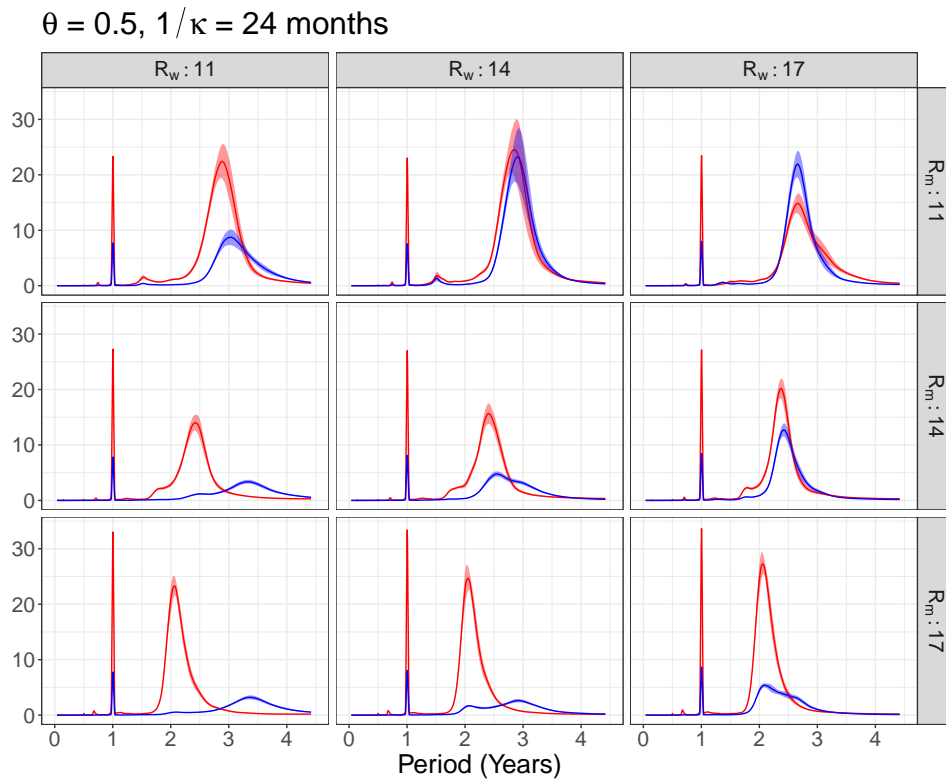
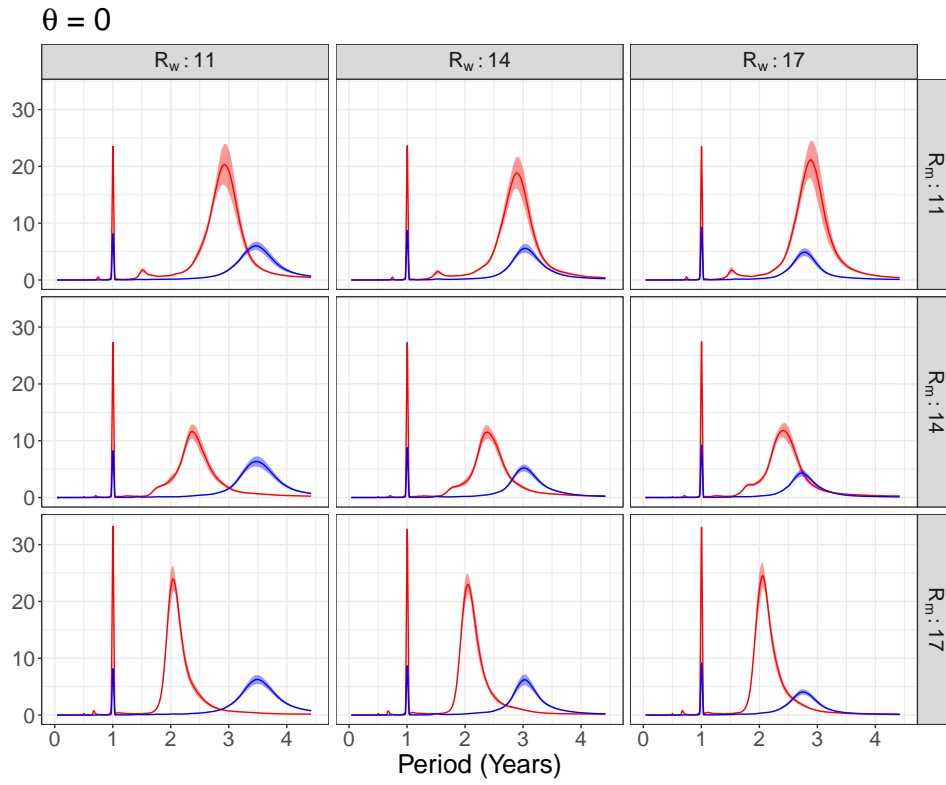
Figure 14: Average power spectra of disease incidence from IA model with different seasonal forcing amplitudes. Power spectra were computed using the square-root-transformed normalized measles (red) and WC (blue) incidence weekly series extracted from stochastic simulations of IA model for different scenarios: no IA effect ($\theta = 0$), partial IA effect ($\theta = 0.5, 1/\kappa = 24$ months and $\theta = 1, 1/\kappa = 12$ months), and strong IA effect ($\theta = 1, 1/\kappa = 24$ months). α_m was varied across columns of panels, whereas α_w was varied across rows of panels. A total of 30 realizations were done for each set of parameters. Solid colored lines indicate the average periodogram and colored bands represent 95% confidence intervals

As expected, the magnitude of the periodogram peaks increased as the seasonal amplitude increased for the corresponding disease [32], especially at the 1 year peak. Nevertheless, similar to the previous simulations, we saw an emergence of a 2-year peak which increased with IA strength and duration, while the peak between 2.5 and 3 year decreased for the WC periodogram (Figure 14). However, the peak near 2.5 years in the WC periodogram was more prominent at greater IA strengths and durations with a larger α_m . Meanwhile, the measles periodogram consistently displayed peaks in the 1- and 2-year periods.

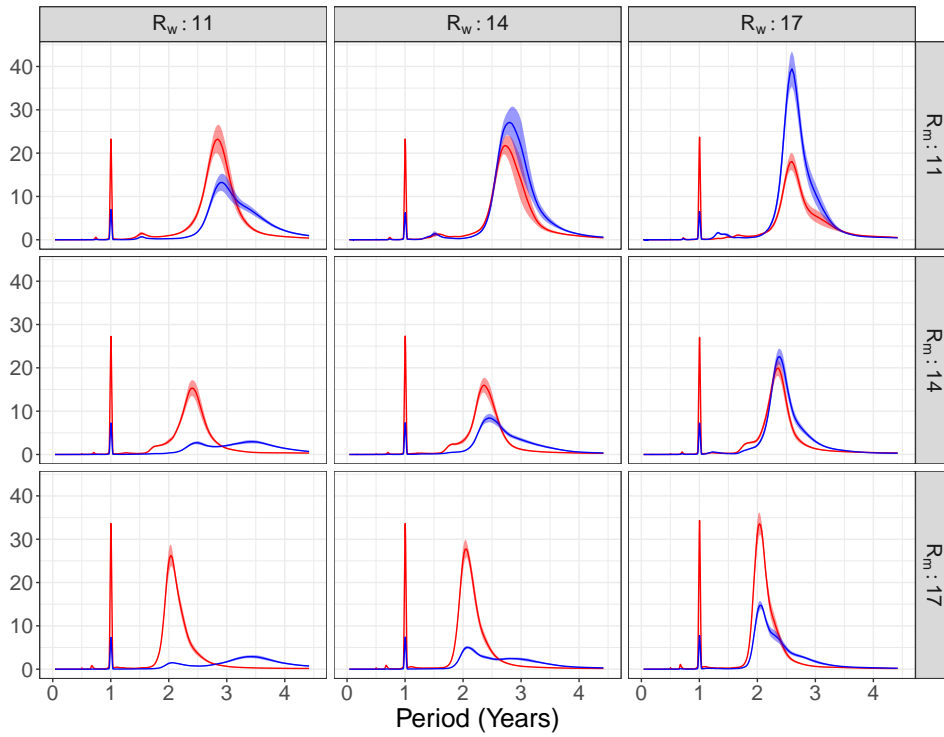
Another parameter that affects the dynamics of diseases and the qualitative features of the power spectra is the mean transmission rate [7, 32]. Hence, simulations with $N = 8 \times 10^5$ were performed using different pairs of mean transmission rate with $\mathcal{R}_{0,m}, \mathcal{R}_{0,w} \in [11, 14, 17]$. Note that \mathcal{R}_0 refers to the basic reproduction number for the SEIR model of the associated disease, and the mean transmission rate was calculated using eq. (6).

Without IA effects, increasing the mean transmission rate shifted the dominant longer period spectral peak towards shorter periods in the periodogram for both diseases (Figure 15). Similar to previous simulations, with greater IA strength and duration, the position of the peaks in the measles periodogram remained roughly the same. Meanwhile, in the WC periodogram, a new peak arose at the same location as the longer period peak in the measles periodogram, while the already existing longer period peak decreased in magnitude. The newly formed peak in the WC periodogram had a relatively weaker magnitude with a smaller transmission rate for WC, or a larger transmission rate for measles.

Nevertheless, in all sets of parameters analyzed, introducing measles-induced IA made the longer period spectral structure of WC resemble that of measles. However, the extent to which this resemblance occurs may depend on the value of the parameters, such as seasonal forcing or transmission rate.



$\theta = 1, 1/\kappa = 12$ months



$\theta = 1, 1/\kappa = 24$ months

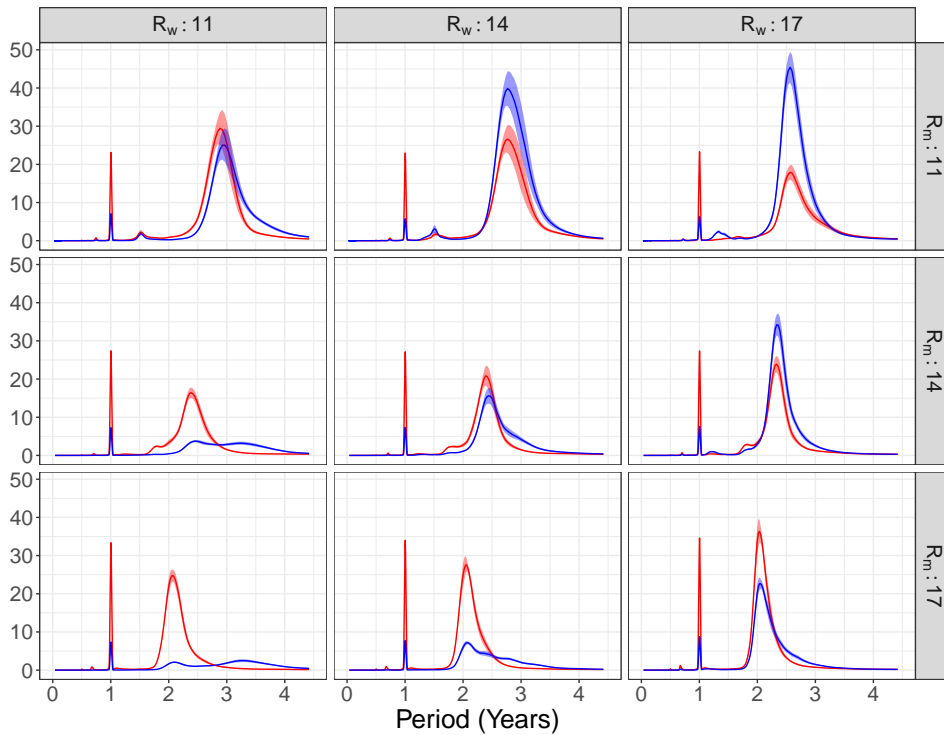


Figure 15: Average wavelet spectra of disease incidence from IA model with varying mean transmission rate. Power spectra were computed using the square-root-transformed normalized measles (red) and WC (blue) incidence weekly series extracted from stochastic simulations of IA model for different scenarios: no IA effect ($\theta = 0$), partial IA effect ($\theta = 0.5, 1/\kappa = 24$ months and $\theta = 1, 1/\kappa = 12$ months), and strong IA effect ($\theta = 1, 1/\kappa = 24$ months). $\mathcal{R}_{0,m}$ was varied across columns of panels, whereas $\mathcal{R}_{0,w}$ was varied across rows of panels.. A total of 30 realizations were done for each set of parameters. Solid colored lines indicate the average periodogram and colored bands represent 95% confidence intervals

4 Modelling Immune Amnesia with Time-Varying ν & μ

We have so far assumed that the parameters of the IA model were constant. However, this is not reflective of what happens in the real world, making comparisons between the simulations and real data questionable. Instead, time-varying parameters may be needed to better understand how IA affected disease dynamics during the time period in London discussed in section 2.

4.1 London Birth and Death Rates 1750–1900

As described in Section 2, the LBoM and RGWR reported the weekly number of baptisms/births and burials/deaths between 1750 to 1900. Hence, these data were used to estimate the *per capita* birth and death rates of London during this time period. First, the overall trend in births and ACM was calculated using EMD (Figure 16) as previously done by Krylova and Earn [4]. This was done since the data were noisy and likely affected by sampling errors such as heaping² [4].

²**Heaping** refers to instances where backlogged entries were submitted together, resulting in an unusually high number of deaths near the end of the reporting year.

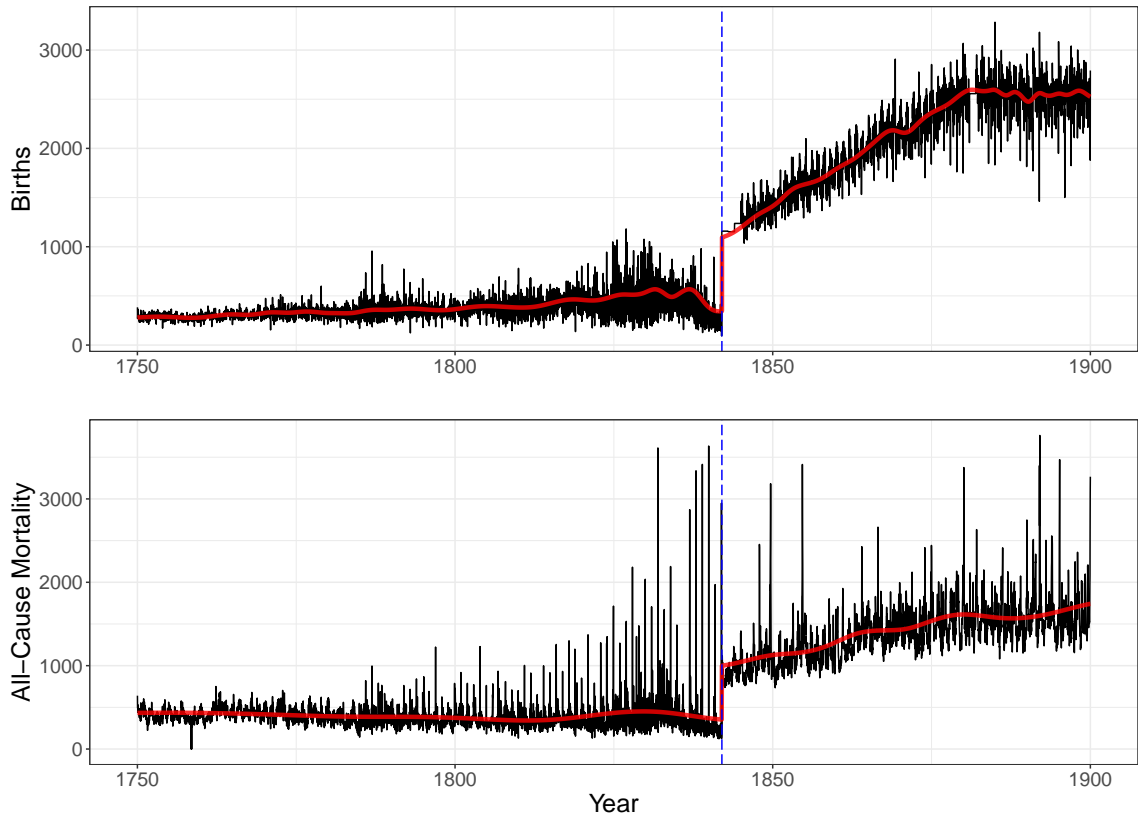


Figure 16: Weekly births (top panel) and all-cause mortality (bottom panel) in London, 1750–1900. Data from the LBoM was used between 1750–1842, and data from the RGWR was used between 1842–1900. The blue dashed line represents the year which the data switches from LBoM to RGWR. The solid red line represents the trend in the raw birth and ACM data calculated using empirical mode decomposition, as done previously by Krylova and Earn [4].

The trend was then divided by the London population size (Figure 17) to calculate the weekly *per capita* birth and death rates. The population size estimates at these time points were linearly interpolated from the annual London population data compiled and estimated by Krylova and Earn (assuming that these values were reported at the beginning of the year) [4]. To account for differences in geographical sampling area between LBoM and RGWR, we used the inner London population for the LBoM sampling period, and the total population for the RGWR sampling period (Figure 18).

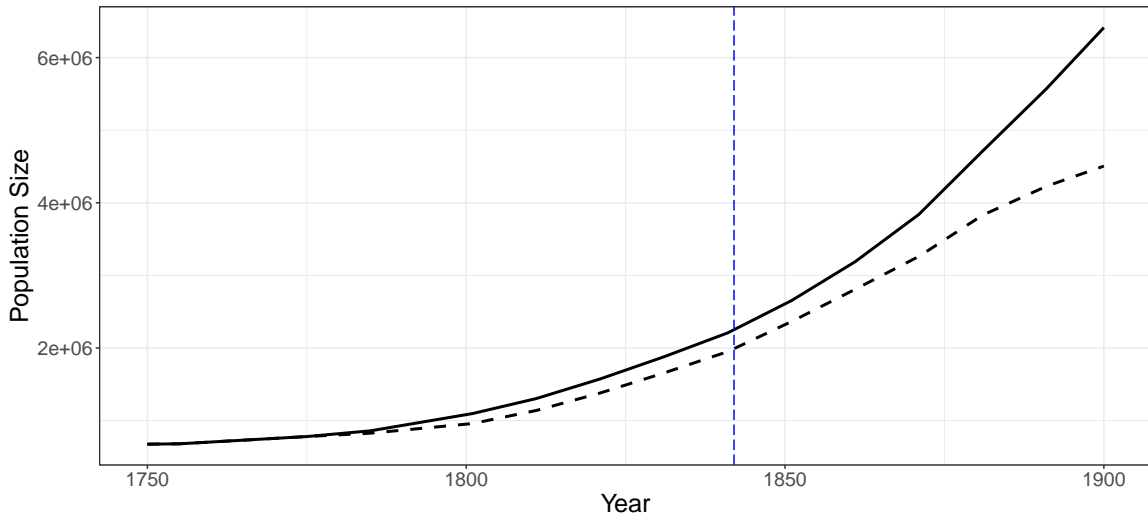


Figure 17: Population size of London, 1750–1900 estimated by Krylova and Earn [4]. The annual population size of inner London (dashed black line) and London (solid black line) is shown. To calculate *per capita* vital rates, the population of inner London was used before 1842 (indicated by dashed blue line), then all of London was used after 1842.

However, a sudden jump in both birth and ACM rate was found at the start of 1842 where the data transitioned from LBoM to RGWR. As discussed previously, this is likely attributed to underreporting during the LBoM period, especially in the early 19th century as the parish system collapsed [4, 16]. Hence, the birth and ACM rates from the LBoM period were transformed to produce a plausible continuous function over time.

To do so, a linear function connecting the first point of the time series and the last time point before the sudden jump in vital rates was fitted ($l_{\text{old}}(t)$). This function was then subtracted from the vital rates during this period, so that we were left with $y_t = x_{t,\text{old}} - l_{\text{old}}(t)$ where $x_{t,\text{old}}$ is the original vital rate time series. Finally, a linear function connecting the first point of the time series and the first point after the sudden jump was fitted ($l_{\text{new}}(t)$). This was then added to y_t to get a new vital rates time series for the LBoM period $x_{t,\text{new}} = y_t + l_{\text{new}}(t)$. The resulting series should bridge the gap during the transition, and address the excessive downward trend at the end of the LBoM period (Figure 18).

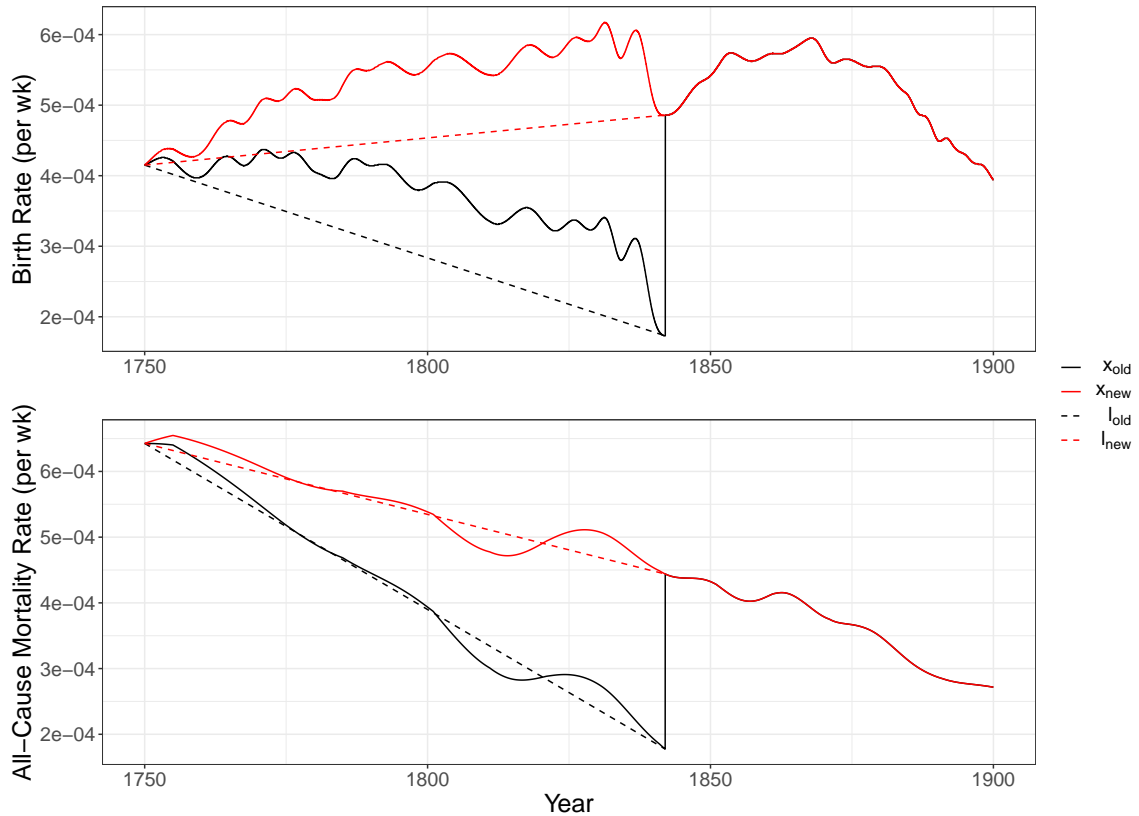


Figure 18: The *per capita* rates after dividing the birth and ACM trends by the population are shown with a solid black line ($x_{t,old}$). To address the sudden jump in 1842, two linear functions l_{old} (black dashed line) and l_{new} (red dashed line) were derived to generate newly transformed *per capita* rates ($x_{t,new}$, red solid line) as described in the main text.

However, the transformed birth rates still showed a sudden step decrease near 1842 which was not necessarily tied with a historic event. It may instead be attributed to the initial reluctance of the RGWR to report births, leading to the underreporting of births when the RGWR first took over [16, p.195]. Hence, this was addressed by replacing it with a linear trend fitted between the closest two peaks (Figure 19).

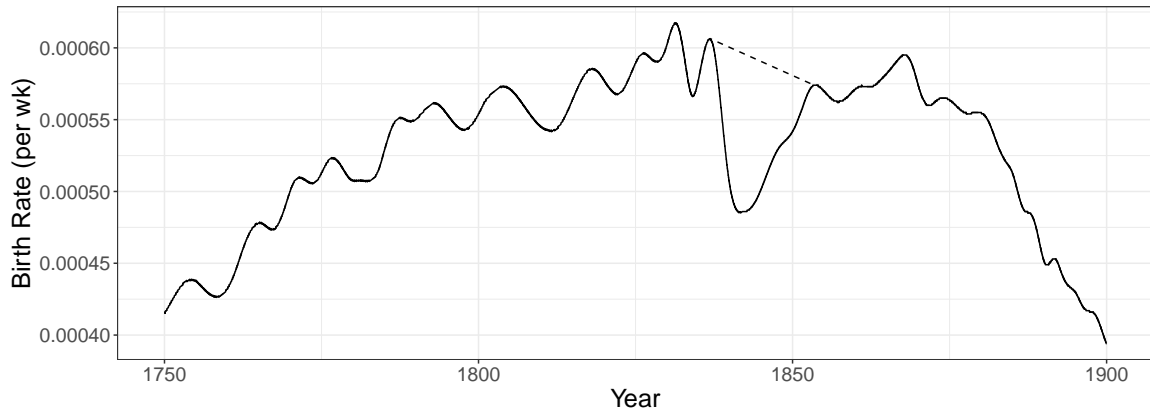


Figure 19: Correction of calculated *per capita* birth rate in London, 1750–1900. The solid line shows the *per capita* weekly birth rate that was estimated from the data. The dotted line was fitted to replace the sudden decrease in birth rate that may be due to sampling errors.

The newly generated vital rates were compared with the annual England *per capita* birth and death rates calculated by Wrigley and Schofield [36] to assess their plausibility. The transformed London *per capita* ACM rate followed a similar downward trajectory as the England rates (Figure 20). The transformed *per capita* birth rate also followed a similar trend compared to the England rates, but was lower in value. As a result, we decided to try two different measures of birth rate for further simulations (Figure 20):

- The original transformed *per capita* birth rate calculated from the data ($\nu_{\text{low}}(t)$).
- The same *per capita* birth rate translated horizontally up to approximately coincide with the England rates. This assumes regional homogeneity within England ($\nu_{\text{high}}(t)$).

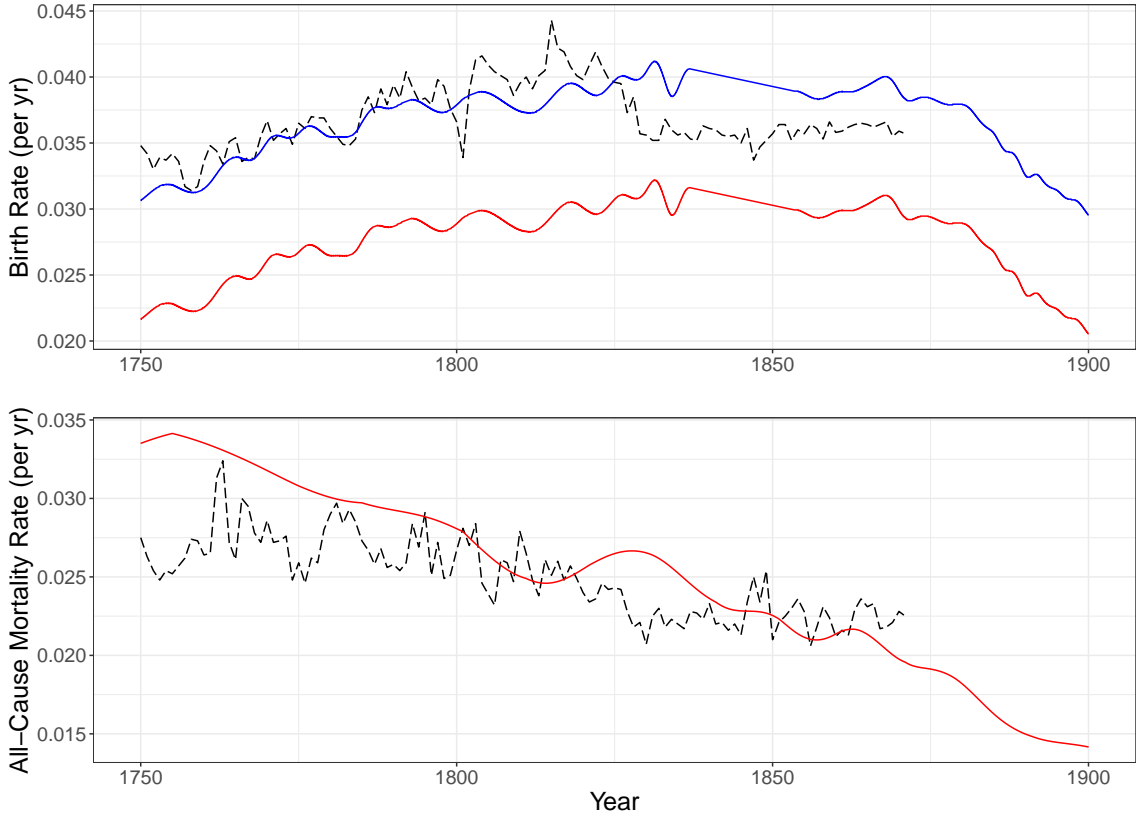


Figure 20: Comparing calculated *per capita* vital rates of London with estimated vital rates of England. The dashed line represents the annual *per capita* birth (top panel) and death (bottom panel) rates of England estimated by Wrigley and Schofield [36]. The solid red line shows the *per capita* vital rates of London estimated as described in the main text. Note for birth rate (top panel), another birth rate of London was obtained (ν_{high} , blue line) by horizontal translation of the original rate (ν_{low} , red line) such that ν_{high} coincided closely with the England rates.

4.2 Methods

Stochastic simulations of the IA model with time-varying $\nu(t)$ (birth rate) and $\mu(t)$ (ACM rate) were performed using the same procedure from Section 3.4. All other parameter values were taken from Table 1 while varying $1/\kappa$ and θ . When necessary, $\nu(t)$ and $\mu(t)$ were linearly interpolated from the London birth and ACM rates when calculating the transition rates in the adaptive tau algorithm. Separate simulations were carried out using ν_{low} and ν_{high} for each set of parameters as well. Along with the periodogram of the whole time series, periodograms were calculated separately for the time intervals that correspond to the LBoM period (1750–1842) and RGWR period (1842–1900) in the simulations.

4.3 Results

For both ν_{low} and ν_{high} , increasing IA strength (θ) and IA duration ($1/\kappa$) increased the magnitude of the signal at 2 years in the WC periodogram, corresponding to the location of the longer period peak in the measles periodogram (Figure 21, 22, 23 & Appendix B.3, B.4). Meanwhile, increasing IA strength and duration decreased the signal at periods greater than 2 years, but did not affect the signal near 1 year. Furthermore, the magnitude of the signal near 2 years in the WC periodogram approached the magnitude of the peak near 2 years in the measles periodogram. Peaks of comparable magnitude at the 2-year period for measles and WC were also observed in the periodograms of the London mortality data as well, especially during the RGWR sampling period (Figure 24).

Compared to simulations with the same parameters but using constant ν and μ (Figures 9, 10, 11 & Appendix B.1), the WC periodograms when IA was absent showed different spectral structures. While the WC periodograms from simulations with constant vital rates showed a peak near 2.7 years, substituting the vital rates for the London birth and ACM rate between 1750–1900 resulted in a dominant peak near 2 years. When IA was introduced, a similar change in the longer period spectral structure of the WC periodogram was observed regardless of the ν and μ used, where signals at 2 years became more prominent.

Simulations with time-varying ν and μ during the LBoM sampling period showed significantly different periodogram structure compared to the real data for both diseases regardless of the presence of IA (Figure 22, Appendix B.3.2, B.4.2). However, simulations corresponding to the RGWR period showed local peaks near the same position in the WC periodogram as the London data when a weak IA strength or IA duration of less than 1 year was used, especially for ν_{high} (Figure 23, 25, Appendix B.3.3, B.4.3).

The described trends in the periodogram were found for both ν_{low} and ν_{high} . However, comparing the total number of individuals N in the system over time, we found that the trajectory of N for ν_{high} was closer to the growth of London population compared to ν_{low} (Figure 26).

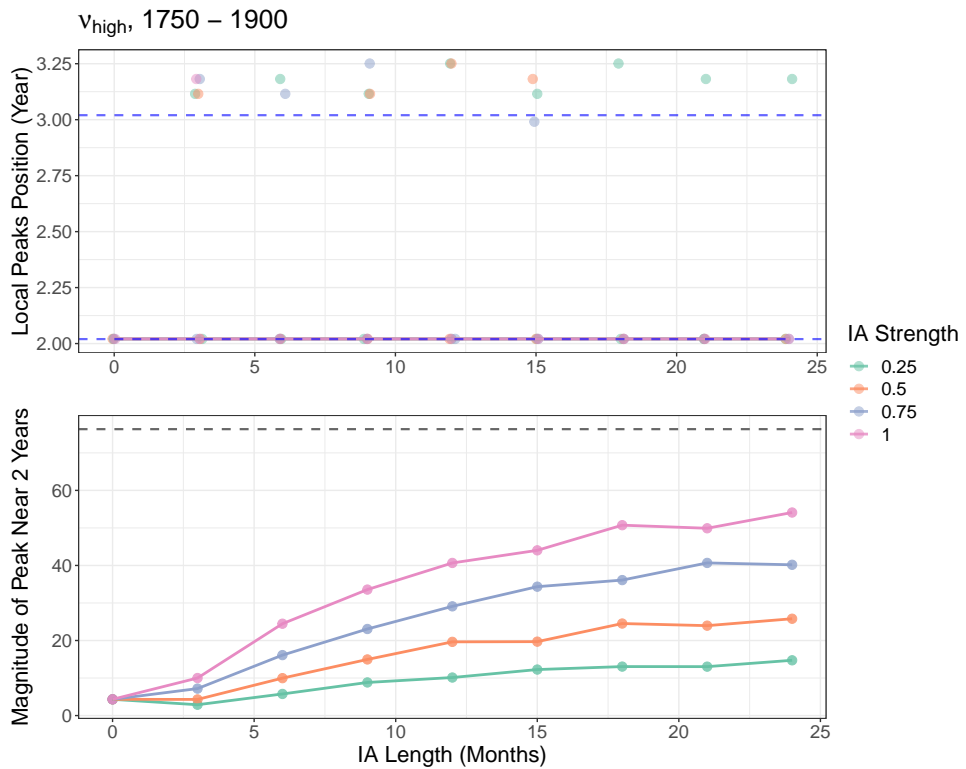
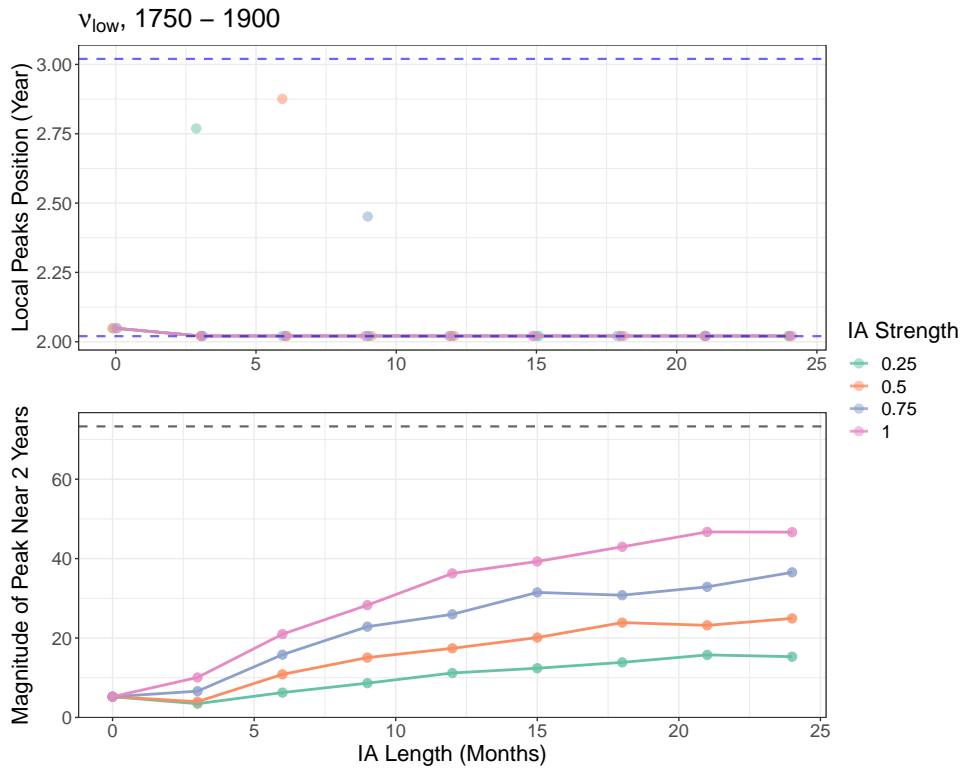
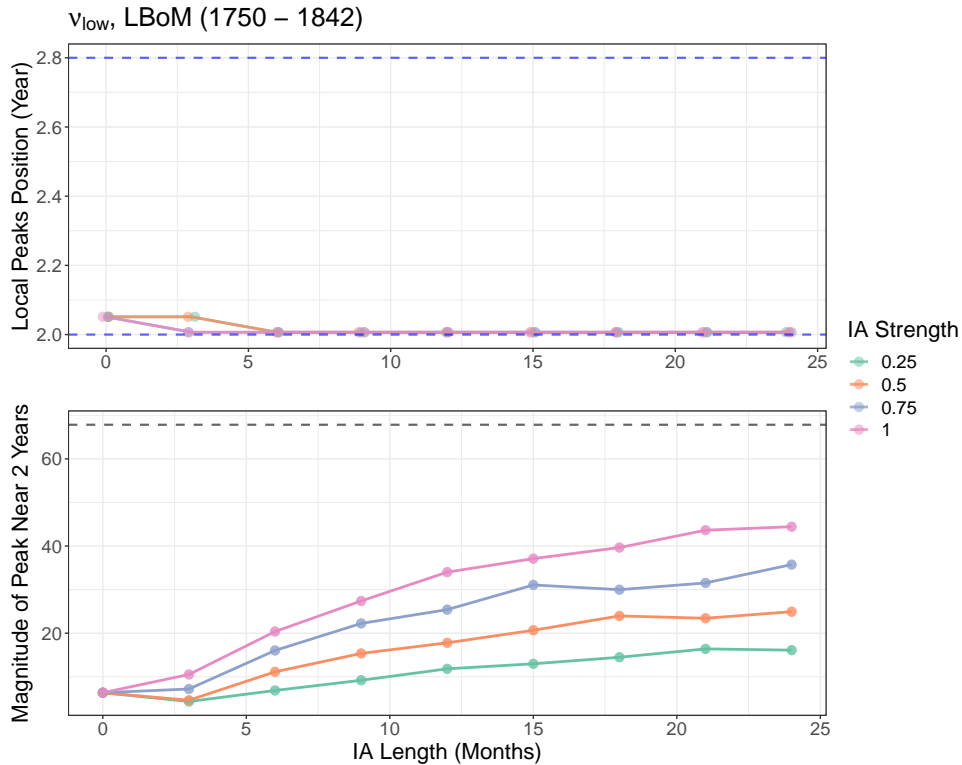


Figure 21: Longer period spectral structure of WC periodogram from the IA model using time-varying $\nu(t)$ and $\mu(t)$ (estimated from section 4.1) and different θ and $1/\kappa$. Power spectra were computed using the square-root-transformed normalized WC incidence weekly series extracted from stochastic simulations of IA models. The simulations were performed for both ν_{low} (top two panels) and ν_{high} (bottom two panels). For each set of two panels, the top panel shows the peaks of the average periodogram of 30 realizations between 2 and 3 years. The points connected by the bold line represent the highest peak between this range for the associated pair of IA strength and duration, and points not connected by this line represent other local peaks of lower magnitude that were observed. The blue dashed lines represent the peaks of the periodogram for the London WC mortality series. The bottom panel shows the magnitude of the peak near 2 years in the WC periodogram. The dotted black line represents the 2-year peak in the measles periodogram with no IA effects.



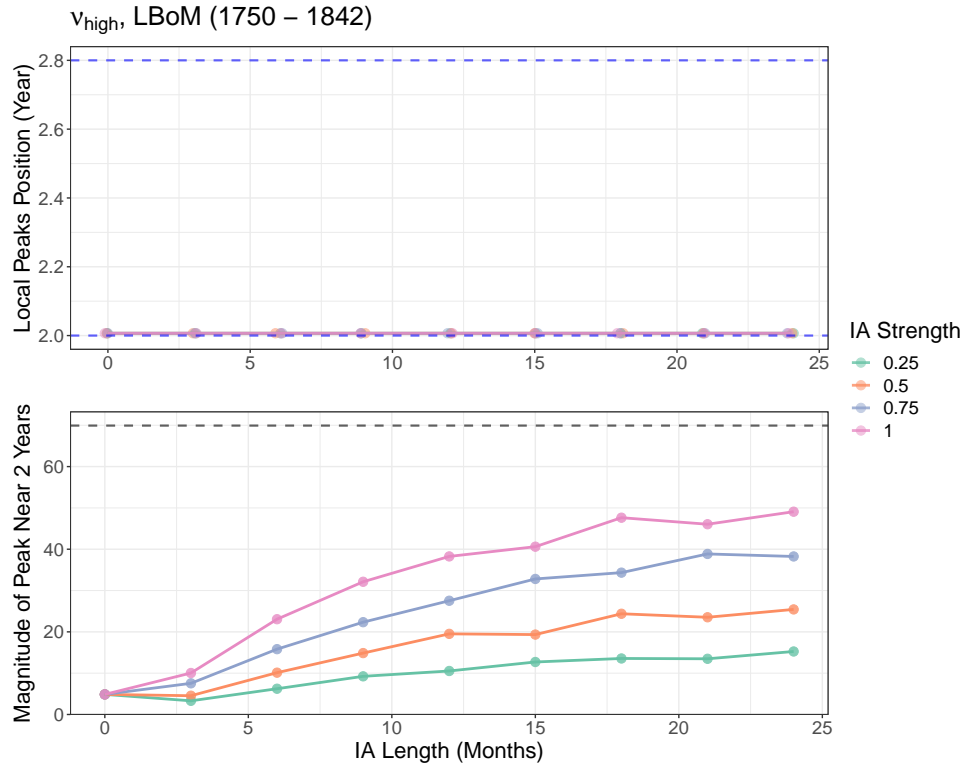


Figure 22: Longer period spectral structure of WC periodogram from the IA model using time-varying $\nu(t)$ and $\mu(t)$ in LBoM sampling period (estimated from section 4.1) and different θ and $1/\kappa$. Power spectra were computed using the square-root-transformed normalized WC incidence weekly series extracted from stochastic simulations of IA models. The simulations were performed for both ν_{low} (top two panels) and ν_{high} (bottom two panels) between 1750–1842. For each set of two panels, the top panel shows the peaks of the average periodogram of 30 realizations between 2 and 3 years. The points connected by the bold line represent the highest peak between this range for the associated pair of IA strength and duration, and points not connected by this line represent other local peaks of lower magnitude that were observed. The blue dashed lines represent the peaks of the periodogram for the London WC mortality series. The bottom panel shows the magnitude of the peak near 2 years in the WC periodogram. The dotted black line represents the 2-year peak in the measles periodogram with no IA effects.

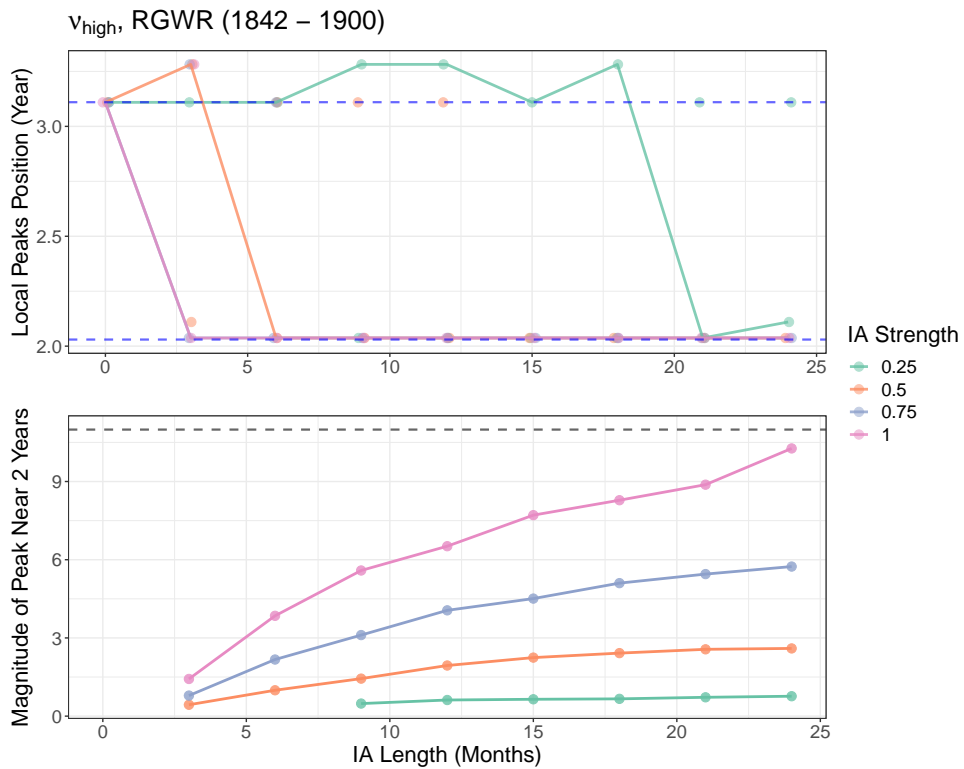
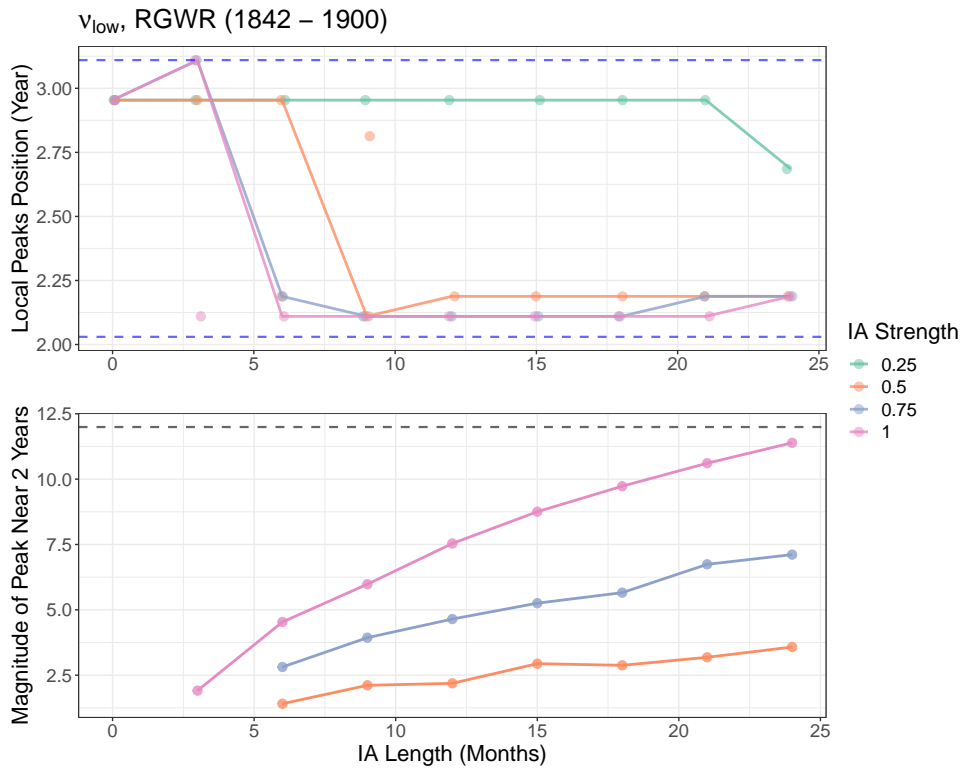


Figure 23: Longer period spectral structure of WC periodogram from the IA model using time-varying $\nu(t)$ and $\mu(t)$ in RGWR sampling period (estimated from section 4.1) and different θ and $1/\kappa$. Power spectra were computed using the square-root-transformed normalized WC incidence weekly series extracted from stochastic simulations of IA models. The simulations were performed for both ν_{low} (top two panels) and ν_{high} (bottom two panels) between 1842–1900. For each set of two panels, the top panel shows the peaks of the average periodogram of 30 realizations between 2 and 3 years. The points connected by the bold line represent the highest peak between this range for the associated pair of IA strength and duration, and points not connected by this line represent other local peaks of lower magnitude that were observed. The blue dashed lines represent the peaks of the periodogram for the London WC mortality series. The bottom panel shows the magnitude of the peak near 2 years in the WC periodogram. The dotted black line represents the 2-year peak in the measles periodogram with no IA effects.

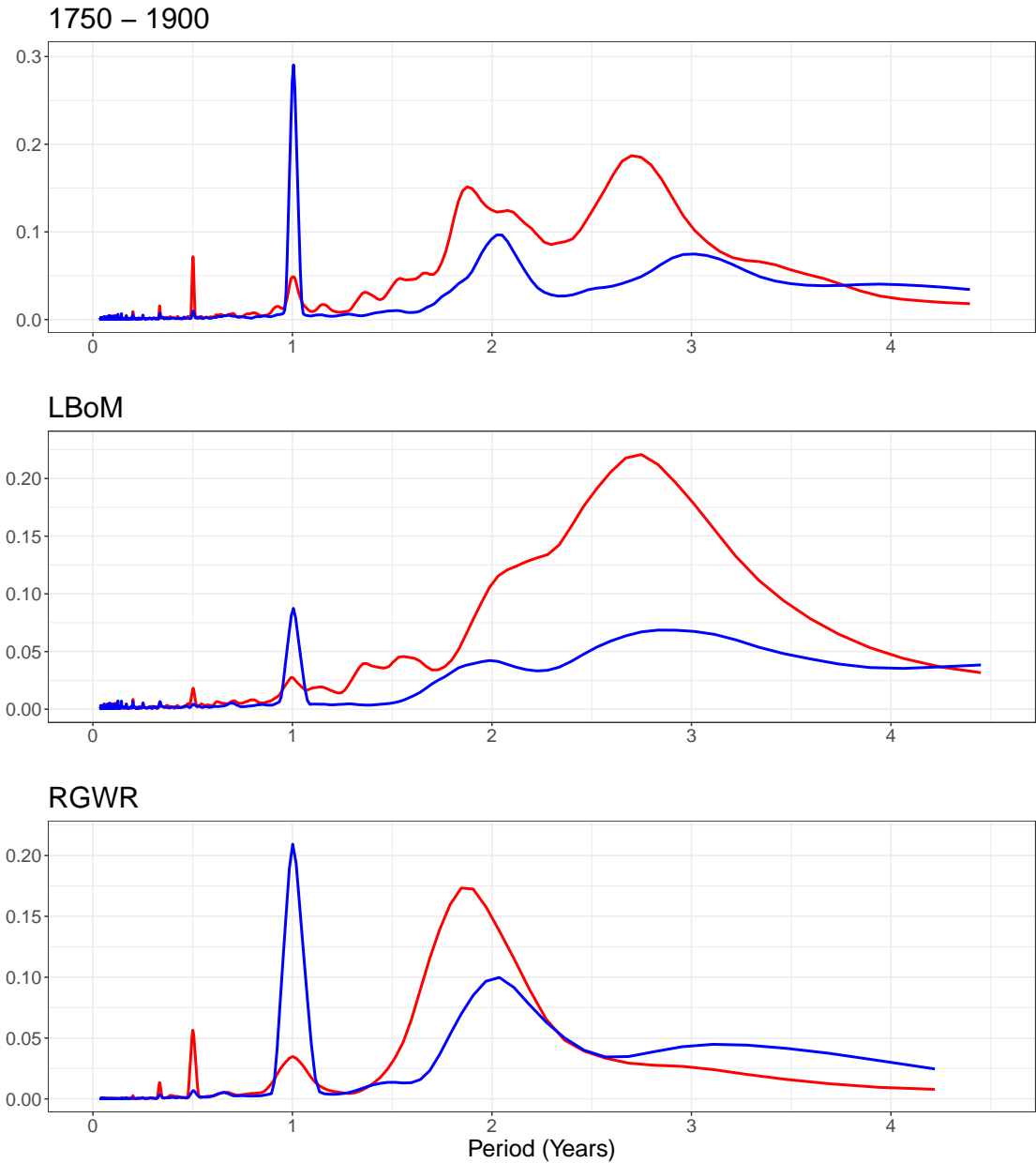


Figure 24: Periodogram of weekly measles and WC mortality time series in London for different time periods. The square-root-transformed normalized disease mortality time series was used to calculate the periodograms for measles (red) and WC (blue). Top panel used all the data between 1750–1900, middle panel used the LBoM sampling period (1750–1842), and the bottom panel used the RGWR sampling period (1842–1900).

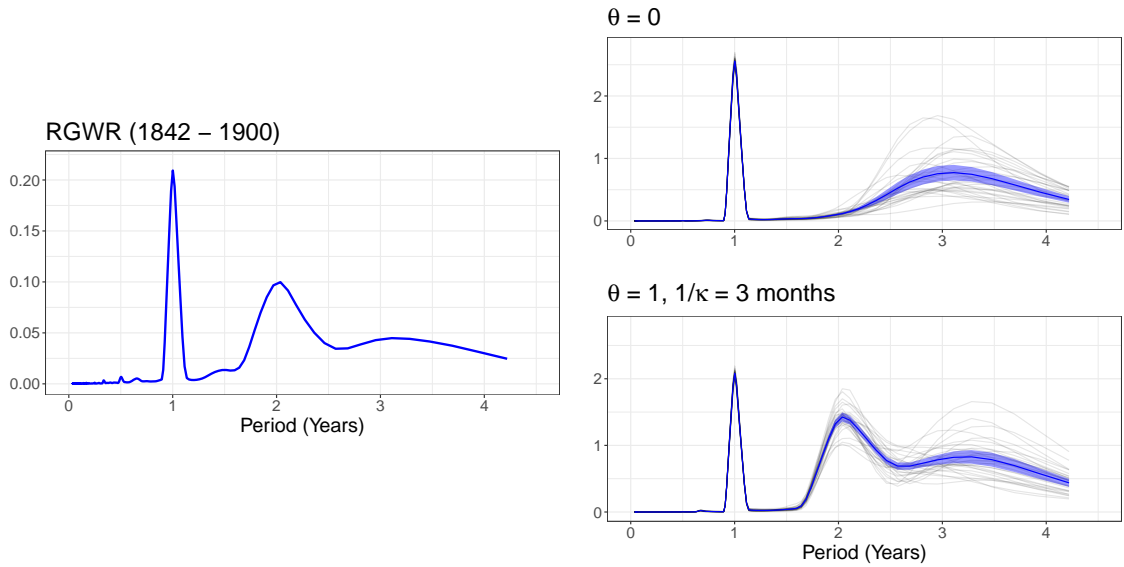


Figure 25: Periodogram of weekly WC mortality in London and WC incidence from simulations using time-varying $\nu_{\text{high}}(t)$ and $\mu(t)$ during the RGWR sampling period. The square-root-transformed normalized WC mortality and incidence time series was used to calculate the periodograms. The left panel shows the periodogram for the real London mortality data during the RGWR sampling period, and the right panels show the periodograms from simulations with no IA effects ($\theta = 0$, top panel) and weak IA effects ($\theta = 1, 1/\kappa = 3$ months, bottom panel). For periodograms of the simulations, grey lines represent the power spectra of 30 different realizations, while solid colored lines indicate the average periodogram and colored bands represent 95% confidence intervals.

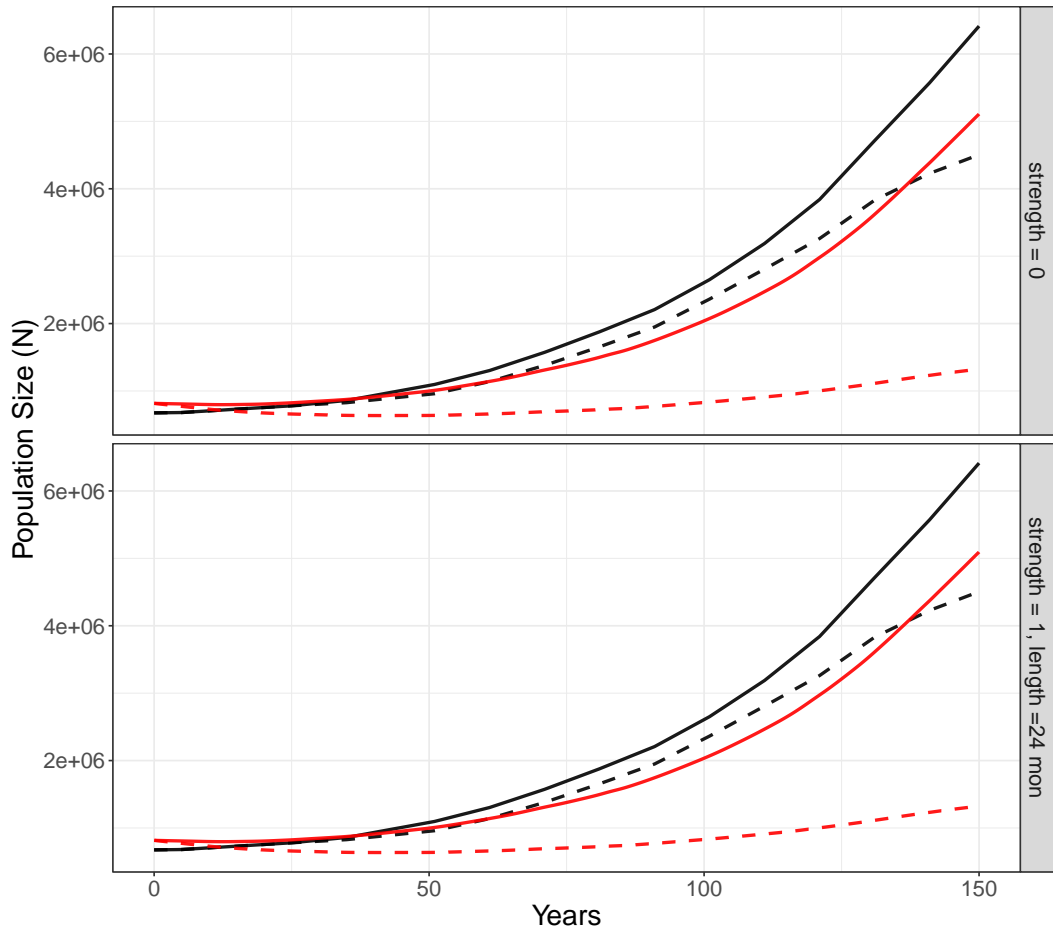


Figure 26: Total individuals within the system during stochastic simulations for ν_{low} and ν_{high} . The sum of all the compartments (N) over time were averaged over 30 realizations for the model with no IA effects ($\theta = 0$) and strong IA effects ($\theta = 1, 1/\kappa = 24$ months). The red dashed line is the N for the simulation with ν_{low} , and the red solid line is the N for the simulation with ν_{high} . The black dashed line is the population of inner London starting 1750, and the black solid line is the population of total London starting 1750.

5 Discussion & Future Directions

5.1 Discussion

5.1.1 London measles and WC mortality, 1750–1900

We first analyzed the recurrent patterns of measles and WC mortality in London between 1750–1900. Our analysis of the London data provides a weekly measles and WC mortality time series which spans 150 years during the pre-vaccination era. Previous work on the epidemic patterns of measles and WC in London during this time period was carried out by Duncan *et al.* with a shorter annual time series [6, 30]. For WC, Duncan *et al.* [30] reported an interepidemic period of 3 years between 1750–1785, and a basic periodicity of 5 years between 1785–1812. For measles, Duncan *et al.* [6] reported a 3-year period beginning in 1750, which progressively decreased to 2 years at the beginning of the 19th century. The reported results agree with our wavelet analysis of the two diseases, except for WC between 1785–1812 (Figure 5, 27). The WC wavelet spectrum showed peaks near 1 year and between 2 and 3 years between 1785–1812, but not at 5 years. Beyond these time periods, the periodicities of the diseases in the late 19th century were consistent with previous investigations of recurrent patterns during the 20th century pre-vaccination era [34, 57]. The observed changes in dynamical patterns over time may have resulted from a combination of different factors such as population size, temperature, malnutrition, contact patterns, and birth rates [5, 6, 7, 30, 32, 40, 60]. Overall, the organized data and the spectral analysis could be used as resources for further studies on changes in epidemiological and dynamical patterns.

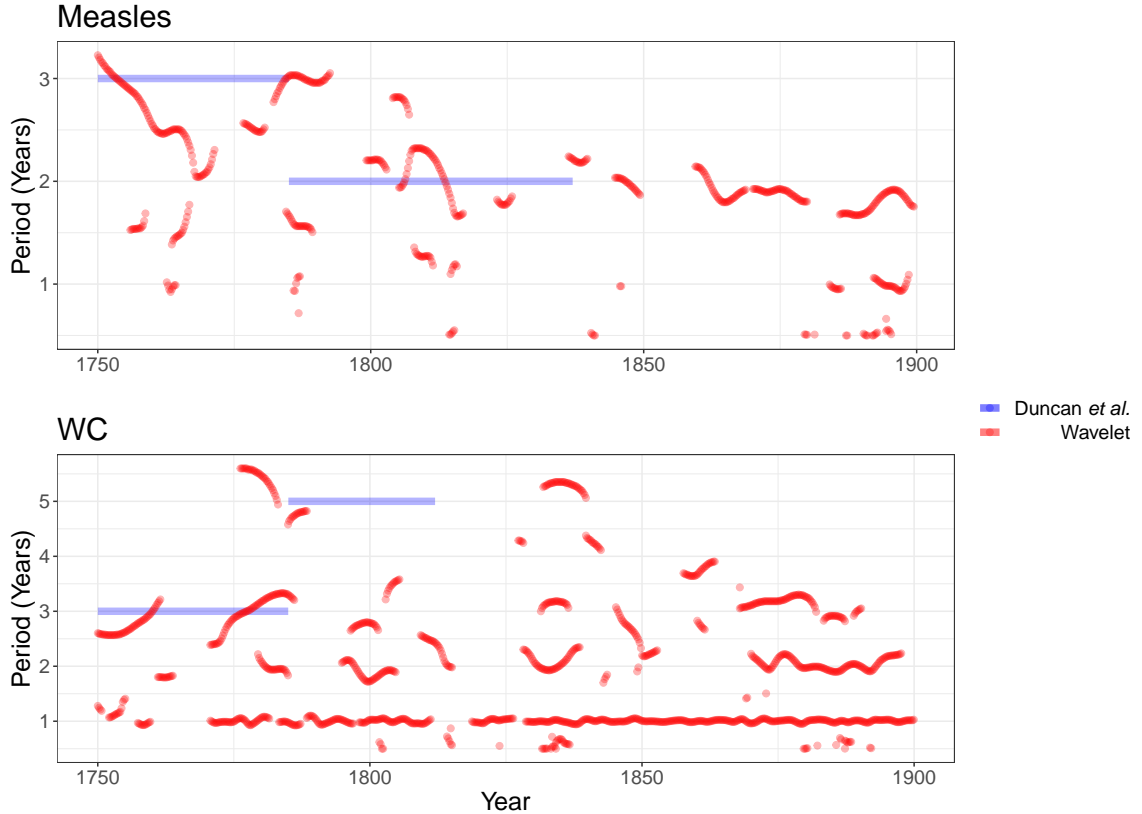


Figure 27: Comparison of wavelet analysis performed using London measles and WC data with previous studies. The red dots show ridges found by the `WaveletComp` [44] package in the wavelet spectra of the London disease mortality time series (computed in Section 2.4). Blue lines represent the interepidemic intervals computed by Duncan *et al.* [6, 30].

5.1.2 IA and WC spectral structure

By running simulations incorporating demographic stochasticity, we found that measles-induced IA influenced the complex recurrent epidemics of WC in our model. Simple deterministic models have had difficulties predicting the multiannual dynamics of WC during the pre-vaccination era [32, 56], as it mainly predicted annual dynamics. Adding noise to the system was previously found to better account for longer periodicities in WC [9, 32, 34, 56], where dominant cycles between 2–2.5 years or near 2.7 years were usually reported apart from annual patterns. When similar parameters were used, the analyzed two disease model with no IA effects showed WC periodograms that agreed with these previous findings (Figure 9 & 11). However, when partial IA strength or a short IA duration was introduced to the system, the WC periodogram showed a dominant peak at 2 years along with peaks between 2.5–3 years, exhibiting more complex patterns between 2–3-year periods (Figure 9 & 11).

These two signals were also seen when the wavelet spectra of WC incidence was generated for simulations with IA effects (12). Interestingly, these spectra more resembles what was seen in the WC periodogram and wavelet spectra of the London mortality data, especially near the late 19th century (Figure 24). Furthermore, the magnitude of the signal at 2 years in the WC periodogram became comparable to that of measles when IA strength or duration increased (Figure 10 & 11), which is what was observed in the London data. These results suggest that IA may better explain the observed longer period recurrent patterns of WC in the real data, compared to other simple models without this effect.

A possible explanation for this trend is that the IA compartment provides another compartment of WC-susceptible individuals, the size of which depends on measles dynamics. This may introduce a new flow of individuals controlled indirectly by measles parameters into the wc-infected compartments, which is detected by signal decomposition in Fourier or wavelet analysis [45]. The “mixing” of measles and WC dynamics with IA may also be supported by wavelet analysis of some realizations which showed coexisting signals near 2 and 3 years, as opposed to regions alternating between 2 and 3 year signals (Figure 12).

5.1.3 IA with different disease parameters

The new longer period spectral structure of WC with the introduction of IA was also observed when a larger population size was used for simulations (Figure 13). Smaller population sizes increase the impact of demographic stochasticity [57], and studies [32, 56, 58] have shown different population size lead to differing signal magnitudes and potential shifts in peak location during spectral analysis. As expected, the ratio between the signals of the peaks differed with larger population size [32], but increased signal at 2-year period was still preserved in the WC periodograms of the simulations. The effect of population size on IA has been commented by Mina *et al.* [61] previously, suggesting that IA is hard to detect in small populations with large fluctuations of mortality, where measles endemics cannot be sustained. All of the simulations performed sustained a nonzero number of measles infectious individuals, so this is likely not applicable to our results.

These trends were also found when the seasonal forcing amplitude of the disease transmission rate was altered (Figure 14). It was very unlikely for the transmission rate to be the same as contact patterns change, especially over the 150 years of weekly disease mortality data that was previously described. For example, when considering childhood infectious diseases, the seasonal forcing amplitude likely changed as more students attended schools [31] due to changes in policies. Previous studies have assessed the interplay between stochastic processes and seasonal forcing amplitude in epidemiological models [33, 56, 62]. In our stochastic simulations, the relative magnitudes of the resonant peaks in the periodograms increased compared to nonresonant

peaks as expected [32], especially at annual periods. Nevertheless, the increased signal at 2-year periods along with decreased signal between 2.5–3 years in the WC periodogram was found to be robust to seasonal amplitude. However, with a larger amplitude of seasonal forcing for measles transmission (α_m), the signal between 2.5–3 years persisted for greater IA strengths and durations.

Similar patterns were observed when the mean transmission rate of the diseases were altered (Figure 15). Regardless of the value of $\langle\beta\rangle$ that was chosen for measles and WC, the emergence of a peak at a new location was found in the WC periodogram with increased IA strength and duration. Furthermore, the location of the new peak in the WC periodogram corresponded to the location of the longer period peak in the measles periodogram, which varied with differing $\langle\beta_m\rangle$. However, the amplitude of the newly formed peak was relatively greater compared to the measles peak with higher $\langle\beta_w\rangle$ and/or smaller $\langle\beta_m\rangle$. Overall, this demonstrates that the structure of the altered WC recurrent epidemics depended on measles recurrent epidemics.

Previous studies analyzing immunological assays, population-level data, and hospital records have provided evidence for the immunomodulatory effect of measles in various countries and communities [14, 17, 18, 19, 20, 21, 22, 23, 26]. Similarly, the analyses performed show that the resemblance of WC recurrent patterns to measles with the introduction of IA can manifest in settings represented by different population sizes and contact patterns.

5.1.4 IA with time-varying ν and μ

Using calculated vital rates of London in the simulations, the WC periodogram of the simulated data with partial IA effects corresponding to the RGWR period had similar peak locations between 2 and 3 years as the London mortality data. (Figure 23, 25). Furthermore, the magnitude of the signal at 2 years approached that of measles when IA was introduced, similar to what was seen in the real data. However, the resemblance occurred when IA strength was very weak, or the duration of reduced immunity was less than a year. This duration was short compared to what some experimental studies have reported [14, 18, 19, 20], but there are other studies which have reported a duration of immunosuppression spanning less than a year [17, 21, 23]. Nevertheless, in conjunction with historic accounts noting the temporal association between measles and WC epidemics [15, 16] and correlation studies providing evidence for the immunosuppressive effect of measles [19, 20, 21, 22, 23], our results suggest IA may have contributed to the observed epidemic patterns of WC to a certain extent.

Contrastingly, the WC periodogram for the simulations using vital rates in the LBoM time period only showed a dominant 2-year peak regardless of IA, whereas the real data showed peaks near both 2 and 3 years (Figure 22, 24). One reason for this disagreement may be due to the demographic characteristics of London during this time

period. Mina *et al.* [61] showed that IA effects were especially evident in countries with low mortality and large populations such that outbreaks were associated with biological drivers and not stochastic events. However, in our case, it may also be because of the discrepancies in the parameters used, especially for measles. While simulations predicted a strong 2-year peak for the measles periodogram, the periodogram of the real data during this time period showed a dominant peak near 2.7 years. As the position of the peaks in the WC periodogram depend on the peaks in the measles periodogram when IA is introduced (Figure 15), any differences in simulated measles dynamics may have resulted in discrepancies in the WC periodograms.

5.1.5 Birth rate of London, 1750–1900

We calculated two estimates for the *per capita* birth rate of London (ν_{low} and ν_{high} , Figure 20) and found that similar trends in the periodograms were observed regardless of which birth rate was used in the simulation. However, the total number of individuals in the system over time for ν_{high} more resembled the population growth of London compared to ν_{low} (Figure 26). Even though ν_{low} better represented the actual reported baptisms from the aggregated data, the simulations suggested that ν_{high} was more plausible in this case. This may suggest the LBoM greatly underestimates baptisms, likely attributed to the bills excluding individuals not part of the established church, overlooking the increasing London geographic boundaries, and other potential factors as the parish registration system progressively collapsed [4]. In fact, questions regarding the reported baptisms and all-cause burials during the LBoM period were raised by Creighton, stating that the bills may be inadequate to representing the whole metropolitan area [16, p. 133].

According to the LBoM data, the total burials exceeded baptisms until the beginning of the 19th century. Wrigley and Schofield [36, p. 166] suggested that this difference was consistent with patterns of massive immigration and high mortality that occurred in London during this time. However, they also believed that this deficit may be reflected by under-registration between births and deaths. Other areas of England such as Manchester, Sheffield, and York reported that births exceeded deaths at an earlier time point than London [16, pp. 38, 64, 536]. As some demographic measures such as marital fertility showed little regional variation in the pre-industrial era [63], it may be more plausible that London also followed a similar trend as the other regions.

5.2 Future Directions

One main limitation when comparing the stochastic simulations to the real data was that the used parameters may not reflect the true values during that time, especially in the case of measles during the LBoM sampling period. For example, the \mathcal{R}_0 's used were estimated from recent pre-vaccination data [46], whereas this quantity may differ for the LBoM period, due to contrasting population characteristics such as birth rates

or contact patterns. In addition, a constant value was chosen for the seasonal forcing amplitude, but it likely varied throughout time. Another potential concern is that we used the trends for vital statistics, but the raw values showed some oscillations which may influence disease dynamics [60]. The model was also simplified by assuming certain parameters were constant and lead to the same overall results for simplicity, such as the case reporting probability and proportion of disease deaths. Furthermore, we assumed similar qualitative results would be obtained when excluded from the model as the general trend from the incidence time series would be retained. Overall, using more representative parameters would help better understand whether IA played an important role during this long pre-vaccination era. For example, obtaining a good prior for $\beta(t)$ using the SI method by Jagan *et al.* [64].

Alternatively, the model could be fitted to the London mortality data using methods such as maximum likelihood [13, 65, 66]. Comparing the fitted two-disease IA model to a regular SEIR model would help determine if IA explains the observed WC dynamics better, and estimate the IA strength and duration if so. Initial work by Noori and Rohani [13] found that their IA model did not explain the WC patterns in the pre-vaccination era better compared to a regular SIR model. However, they suggested that the additional challenge of fitting the model to both measles and WC data may have contributed to their findings.

6 Conclusion

Overall, we described a measles and WC mortality series in London which spanned a time period that was not analyzed thoroughly before to our knowledge. Furthermore, a plausible estimate of the *per capita* birth and ACM rate were calculated for this time period. These may function as tools when exploring the long-term dynamics of these diseases and investigating how dynamical transitions may be linked to certain historical events. It also provides a large data set to investigate better methods in predicting dynamical transitions of diseases.

The analysis on IA showed that this measles-induced effect can have significant impacts on the recurrent patterns of other diseases across different disease parameters. It may provide a plausible alternative explanation for the longer periodicities of diseases such as WC. However, further work is needed to better understand this mechanism in other epidemiological contexts, so that it can be considered when implementing vaccination and control strategies against non-measles infectious diseases under the influence of IA.

References

- [1] J Hubschen, I Gouandjika-Vasilache, and J Dina. Measles. *The Lancet*, 399 (10325):678–690, Feb 12 2022. doi: 10.1016/S0140-6736(21)02004-3.
- [2] Measles, Dec 2019. URL <https://www.who.int/news-room/fact-sheets/detail/measles>. Accessed: 2023-02-01.
- [3] KHT Yeung, P Duclos, EAS Nelson, and RCW Hutubessy. An update of the global burden of pertussis in children younger than 5 years: a modelling study. *The Lancet infectious diseases*, 17(9):974–980, 2017.
- [4] O Krylova and David JD Earn. Patterns of smallpox mortality in London, England, over three centuries. *PLOS Biology*, 18(12):1–27, 12 2020. doi: 10.1371/journal.pbio.3000506.
- [5] K Hempel and DJD Earn. A century of transitions in New York City’s measles dynamics. *Journal of the Royal Society of London, Interface*, 12(106):20150024, 2015. doi: 10.1098/rsif.2015.0024.
- [6] CJ Duncan, SR Duncan, and S Scott. The dynamics of measles epidemics. *Theoretical Population Biology*, 52(2):155–163, 1997. doi: <https://doi.org/10.1006/tpbi.1997.1326>.
- [7] DJD Earn, P Rohani, BM Bolker, and BT Grenfell. A simple model for complex dynamical transitions in epidemics. *Science*, 287(5453):667–670, 2000. doi: 10.1126/science.287.5453.667.
- [8] HTH Nguyen and P Rohani. Noise, nonlinearity and seasonality: the epidemics of whooping cough revisited. *Journal of the Royal Society interface*, 5(21):403–413, 2008.
- [9] G Rozhnova and A Nunes. Modelling the long-term dynamics of pre-vaccination pertussis. *Journal of the Royal Society interface*, 9(76):2959–2970, 2012.
- [10] CI Siettos and L Russo. Mathematical modeling of infectious disease dynamics. *Virulence*, 4(4):295–306, 2013.
- [11] RS Ostfeld, F Keesing, and VT Eviner. *Infectious Disease Ecology: Effects of Ecosystems on Disease and of Disease on Ecosystems*. Princeton University Press, Princeton, 2010.
- [12] GB Morales and MA Munoz. Immune amnesia induced by measles and its effects on concurrent epidemics. *Journal of the Royal Society Interface*, 18(179):20210153–20210153, 2021.
- [13] N Noori and P Rohani. Quantifying the consequences of measles-induced immune modulation for whooping cough epidemiology. *Philosophical transactions of*

- the Royal Society of London. Series B. Biological sciences*, 374(1775):20180270–20180270, 2019.
- [14] D Bühl, O Staudacher, S Santibanez, R Rossi, H Girschick, V Stephan, B Schmidt, P Hundsdorfer, A von Moers, M Lange, M Barker, MA Mall, U Heininger, D Matysiak-Klose, A Mankertz, and H von Bernuth. Specifically increased rate of infections in children post measles in a high resource setting. *Frontiers in pediatrics*, 10:896086–896086, 2022.
- [15] FM Galassi, E Varotto, C Mussini, and A Cossarizza. Measles-induced immune amnesia likely recorded in the 18th century. *Journal of clinical virology*, 141:104899–104899, 2021.
- [16] C Creighton. *A history of epidemics in Britain*. University Press, Cambridge, 1894.
- [17] NTH Le, NT Ho, B Grenfell, S Baker, and RB Geskus. Biphasic pattern in the effect of severe measles infection; the difference between additive and multiplicative scale. *BMC infectious diseases*, 21(1):1249–1249, 2021.
- [18] L Behrens, JD Cherry, and U Heininger. The susceptibility to other infectious diseases following measles during a three year observation period in Switzerland. *The Pediatric infectious disease journal*, 39(6):478–482, 2020.
- [19] K Gadroen, CN Dodd, GMC Masclee, MAJ de Ridder, D Weibel, MJ Mina, BT Grenfell, MCJM Sturkenboom, DAMC van de Vijver, and RL de Swart. Impact and longevity of measles-associated immune suppression: a matched cohort study using data from the THIN general practice database in the UK. *BMJ Open*, 8(11), 2018. doi: 10.1136/bmjopen-2017-021465.
- [20] MJ Mina, CJE Metcalf, R de Swart, A Osterhaus, and BT Grenfell. Long-term measles-induced immunomodulation increases overall childhood infectious disease mortality. *Science*, 348(6235):694–699, 2015.
- [21] S Xia, CC Gullickson, CJE Metcalf, BT Grenfell, and MJ Mina. Assessing the effects of measles virus infections on childhood infectious disease mortality in Brazil. *The Journal of infectious diseases*, 227(1):133–140, 2022.
- [22] R Sato and M Haraguchi. Effect of measles prevalence and vaccination coverage on other disease burden: evidence of measles immune amnesia in 46 African countries. *Human vaccines & immunotherapeutics*, 17(12):5361–5366, 2021.
- [23] P Aaby, A Bhuiya, L Nahar, K Knudsen, A de Francisco, and M Strong. The survival benefit of measles immunization may not be explained entirely by the prevention of measles disease: a community study from rural Bangladesh. *International Journal of Epidemiology*, 32(1):106–115, 2003.

- [24] VN Petrova, B Sawatsky, AX Han, BM Laksono, L Walz, E Parker, K Pieper, CA Anderson, RD de Vries, A Lanzavecchia, P Kellam, V von Messling, RL de Swart, and CA Russell. Incomplete genetic reconstitution of B cell pools contributes to prolonged immunosuppression after measles. *Science immunology*, 4(41), 2019.
- [25] B Laksono, R de Vries, J Verburgh, E Visser, A Jong, P Fraaij, WLM Ruijs, D Nieuwenhuijse, HJ Ham, M Koopmans, M van Zelm, A Osterhaus, and R de Swart. Studies into the mechanism of measles-associated immune suppression during a measles outbreak in the Netherlands. *Nature communications*, 9(1):4944–10, 2018.
- [26] MJ Mina, T Kula, YM Leng, MM Li, Rory de Vries, M Knip, H Siljander, M Rewers, DF Choy, MS Wilson, HB Larman, AN Nelson, DE Griffin, Rik de Swart, and SJ Elledge. Measles virus infection diminishes preexisting antibodies that offer protection from other pathogens. *Science*, 366(6465):599–606, 2019.
- [27] A Dabbagh, RL Laws, C Steulet, L Dumolard, MN Mulders, K Kretsinger, JP Alexander, PA Rota, and JL Goodson. Progress toward regional measles elimination — worldwide, 2000–2017. *Morbidity and mortality weekly report*, 67(47):1323–1329, 2018.
- [28] HJ Larson, E Gakidou, and CJL Murray. The vaccine-hesitant moment. *New England Journal of Medicine*, 387(1):58–65, 2022.
- [29] E Wilkinson. Is anti-vaccine sentiment affecting routine childhood immunisations? *BMJ*, 376, 2022.
- [30] CJ Duncan, SR Duncan, and S Scott. Whooping cough epidemics in London, 1701-1812: Infection dynamics, seasonal forcing and the effects of malnutrition. *Proceedings of the Royal Society. B, Biological sciences*, 263(1369):445–450, 1996.
- [31] AD Becker, A Wesolowski, ON Bjørnstad, and BT Grenfell. Long-term dynamics of measles in London: Titrating the impact of wars, the 1918 pandemic, and vaccination. *PLoS computational biology*, 15(9):e1007305, 2019.
- [32] T Bauch and DJD Earn. Transients and attractors in epidemics. *Proceedings of the Royal Society. B, Biological sciences*, 270(1524):1573–1578, 2003.
- [33] MJ Keeling, P Rohani, and BT Grenfell. Seasonally forced disease dynamics explored as switching between attractors. *Physica. D*, 148(3):317–335, 2001.
- [34] P Rohani, DJD Earn, and BT Grenfell. Opposite patterns of synchrony in sympatric disease metapopulations. *Science*, 286(286):968–971, 1999.
- [35] MK Matossian. Death in London, 1750-1909. *The Journal of interdisciplinary history*, 16(2):183–197, 1985.

- [36] EA Wrigley and R Schofield. *The population history of England, 1541-1871 : a reconstruction*. Studies in social and demographic history. Harvard University Press, Cambridge, Mass, 1981.
- [37] R Core Team. *R: A Language and Environment for Statistical Computing*. R Foundation for Statistical Computing, Vienna, Austria, 2021. URL <https://www.R-project.org/>.
- [38] D Kim and HS Oh. EMD: A package for empirical mode decomposition and Hilbert spectrum. *The R Journal*, 1(1):40–46, 2009. doi: 10.32614/RJ-2009-002.
- [39] A Stallone, A Cicone, and M Materassi. New insights and best practices for the successful use of empirical mode decomposition, iterative filtering and derived algorithms. *Scientific reports*, 10(1):15161–15161, 2020.
- [40] DJD Earn. Mathematical epidemiology of infectious diseases. In M. A. Lewis, M. A. J. Chaplain, J. P. Keener, and P. K. Maini, editors, *Mathematical Biology*, volume 14 of *IAS/Park City Mathematics Series*, pages 151–186. American Mathematical Society, 2009. doi: 10.1090/pcms/014/05.
- [41] C Chatfield. *The analysis of time series : an introduction*. Chapman & Hall, London, England, 5th ed. edition, 1996.
- [42] DN Fisman. Seasonality of infectious diseases. *Annual review of public health*, 28(1):127–143, 2007.
- [43] B Cazelles, M Chavez, GC de Magny, JF Guégan, and S Hales. Time-dependent spectral analysis of epidemiological time-series with wavelets. *Journal of the Royal Society interface*, 4(15):625–636, 2007.
- [44] A Roesch and H Schmidbauer. *WaveletComp: Computational Wavelet Analysis*, 2018. URL <https://CRAN.R-project.org/package=WaveletComp>. R package version 1.1.
- [45] B Cazelles, M Chavez, D Berteaux, F Ménard, JO Vik, S Jenouvrier, and NC Stenseth. Wavelet analysis of ecological time series. *Oecologia*, 156(2):287–304, 2008.
- [46] RM Anderson and RM. May. *Infectious diseases of humans: Dynamics and control*. Oxford University Press,, Oxford, 1992.
- [47] O Krylova and DJD Earn. Effects of the infectious period distribution on predicted transitions in childhood disease dynamics. *Journal of the Royal Society of London, Interface*, 10:20130098, 2013.
- [48] P van den Driessche. Reproduction numbers of infectious disease models. *Infectious disease modelling*, 2(3):288–303, 2017.

- [49] I Papst and DJD Earn. Invariant predictions of epidemic patterns from radically different forms of seasonal forcing. *Journal of the Royal Society interface*, 16(156):20190202, 2019.
- [50] P Rohani, DJD Earn, B Finkenstädt, and BT Grenfell. Population dynamic interference among childhood diseases. *Proceedings of the Royal Society. B, Biological sciences*, 265(1410):2033–2041, 1998.
- [51] MS Bartlett. Measles periodicity and community size. *Journal of the Royal Statistical Society. Series A. General*, 120(1):48–70, 1957.
- [52] DT Gillespie. A general method for numerically simulating the stochastic time evolution of coupled chemical reactions. *Journal of computational physics*, 22(4):403–434, 1976.
- [53] Y Cao, DT Gillespie, and LR Petzold. Adaptive explicit-implicit tau-leaping method with automatic tau selection. *The Journal of chemical physics*, 126(22):224101–9, 2007.
- [54] DT Gillespie. Approximate accelerated stochastic simulation of chemically reacting systems. *The Journal of chemical physics*, 115(4):1716–1733, 2001.
- [55] Philip J. *adaptivetau: Tau-Leaping Stochastic Simulation*, 2019. URL <https://CRAN.R-project.org/package=adaptivetau>. R package version 2.2-3.
- [56] AJ Black and AJ McKane. Stochasticity in staged models of epidemics: quantifying the dynamics of whooping cough. *Journal of the Royal Society interface*, 7(49):1219–1227, 2010.
- [57] BT Grenfell, ON Bjørnstad, and BF Finkenstädt. Dynamics of measles epidemics: scaling noise, determinism, and predictability with the tsir model. *Ecological Monographs*, 72(2):185–202, 2002.
- [58] M Simões, MM Telo da Gama, and A Nunes. Stochastic fluctuations in epidemics on networks. *Journal of the Royal Society interface*, 5(22):555–566, 2008.
- [59] G Rozhnova and A Nunes. Stochastic effects in a seasonally forced epidemic model. *Physical review. E, Statistical, nonlinear, and soft matter physics*, 82(4 Pt 1):041906–041906, 2010.
- [60] D He and DJD. Earn. Epidemiological effects of seasonal oscillations in birth rates. *Theoretical population biology*, 72(2):274–291, 2007.
- [61] MJ Mina, BT Grenfell, and CJE Metcalf. Response to comment on “long-term measles-induced immunomodulation increases overall childhood infectious disease mortality”. *Science*, 365(6449):134, 2019.
- [62] D Alonso, AJ McKane, and M Pascual. Stochastic amplification in epidemics. *Journal of the Royal Society interface*, 4(14):575–582, 2007.

- [63] C Wilson and R Woods. Fertility in England: A long-term perspective. *Population studies*, 45(3):399–415, 1991.
- [64] M Jagan, MS deJonge, O Krylova, and DJD Earn. Fast estimation of time-varying infectious disease transmission rates. *PLoS Computational Biology*, 16(9):e1008124, 2020.
- [65] AA King, D Nguyen, and EL Ionides. Statistical inference for partially observed Markov processes via the R package pomp. *Journal of Statistical Software*, 69(12):1–43, 2016.
- [66] D He, J Dushoff, T Day, JL Ma, and DJD Earn. Inferring the causes of the three waves of the 1918 influenza pandemic in England and Wales. *Proceedings of the Royal Society of London*, 280(1766):20131345, 2013.

A Analysis of Disease-Free Equilibria

In this section, preliminary numerical analysis is presented for the immune amnesia model used in the thesis. To do so, an SIR version of the model is considered for simplicity:

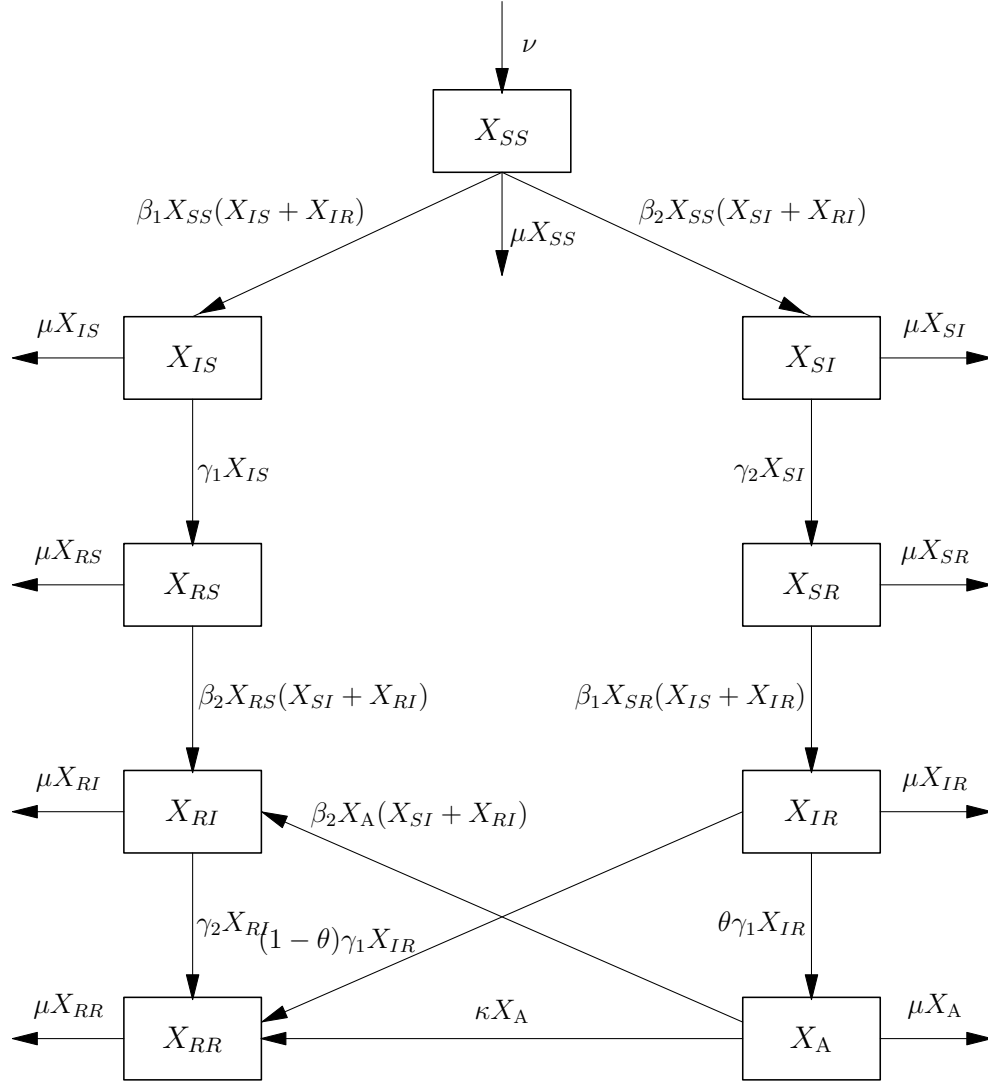


Figure 28: The SIR version of the two-disease immune amnesia model. For two-letter compartments, the first letter represents the stage in measles infection, and the second letter represents the stage in secondary disease infection. The X_A compartment represents those with decreased immunity to the secondary disease due to measles-induced immune amnesia. Parameters with subscript 1 are those pertaining to measles, and subscript 2 are those pertaining to the secondary disease affected by immune amnesia.

Let each compartment represent the proportion of the total population in that compartment, such that $N = X_{SS} + X_{IS} + X_{RS} + X_{RI} + X_{SI} + X_{SR} + X_{IR} + X_A + X_{RR} = 1$. Then, we have the system of ODEs:

$$\frac{dX_{SS}}{dt} = \nu - \beta_1(X_{IS} + X_{IR})X_{SS} - \beta_2(X_{SI} + X_{RI})X_{SS} - \mu X_{SS} \quad (9a)$$

$$\frac{dX_{SI}}{dt} = \beta_2(X_{SI} + X_{RI})X_{SS} - \gamma_2 X_{SI} - \mu X_{SI} \quad (9b)$$

$$\frac{dX_{SR}}{dt} = \gamma_2 X_{SI} - \beta_1(X_{IS} + X_{IR})X_{SR} - \mu X_{SR} \quad (9c)$$

$$\frac{dX_{IR}}{dt} = \beta_1(X_{IS} + X_{IR})X_{SR} - \gamma_1 X_{IR} - \mu X_{IR} \quad (9d)$$

$$\frac{dX_{IS}}{dt} = \beta_1(X_{IS} + X_{IR})X_{SS} - \gamma_1 X_{IS} - \mu X_{IS} \quad (9e)$$

$$\frac{dX_{RS}}{dt} = \gamma_1 X_{IS} - \beta_2(X_{SI} + X_{RI})X_{RS} - \mu X_{RS} \quad (9f)$$

$$\frac{dX_{RI}}{dt} = \beta_2(X_{SI} + X_{RI})(X_{RS} + X_A) - \gamma_2 X_{RI} - \mu X_{RI} \quad (9g)$$

$$\frac{dX_A}{dt} = \theta \gamma_1 X_{IR} - \beta_2(X_{SI} + X_{RI})X_A - \kappa X_A - \mu X_A \quad (9h)$$

$$\frac{dX_{RR}}{dt} = \gamma_2 X_{RI} + \kappa X_A + (1 - \theta) \gamma_1 X_{IR} - \mu X_{RR} \quad (9i)$$

Analyzing the equilibria of the system helps us understand the long-term behaviour of epidemics. When there are no infectious individuals such that $X_{IS} = X_{IR} = X_{SI} = X_{RI} = 0$, then there exists a disease-free equilibrium (DFE) of:

$$(X_{SS}^*, X_{SI}^*, X_{SR}^*, X_{IR}^*, X_{IS}^*, X_{RS}^*, X_{RI}^*, X_A^*, X_{RR}^*) = (\nu/\mu, 0, 0, 0, 0, 0, 0, 0, 0) \quad (10)$$

To analyze its local stability, the Jacobian of the system was calculated and the DFE was substituted to get

$$J(DFE) = \begin{bmatrix} -\mu & -\nu\beta_2/\mu & 0 & -\nu\beta_1/\mu & -\nu\beta_1/\mu & 0 & -\nu\beta_2/\mu & 0 & 0 \\ 0 & \nu\beta_2/\mu - \mu - \gamma_2 & 0 & 0 & 0 & 0 & \nu\beta_2/\mu & 0 & 0 \\ 0 & \gamma_2 & -\mu & 0 & 0 & 0 & 0 & 0 & 0 \\ 0 & 0 & 0 & -\mu - \gamma_1 & 0 & 0 & 0 & 0 & 0 \\ 0 & 0 & 0 & \nu\beta_1/\mu & \nu\beta_1/\mu - \mu - \gamma_1 & 0 & 0 & 0 & 0 \\ 0 & 0 & 0 & 0 & \gamma_1 & -\mu & 0 & 0 & 0 \\ 0 & 0 & 0 & 0 & 0 & 0 & -\mu - \gamma_2 & 0 & 0 \\ 0 & 0 & 0 & \gamma_1\theta & 0 & 0 & 0 & -\mu - \kappa & 0 \\ 0 & 0 & 0 & \gamma_1(1 - \theta) & 0 & 0 & \gamma_2 & \kappa & -\mu \end{bmatrix} \quad (11)$$

The eigenvalues λ of this matrix are:

$$\lambda_{1,2,3,4} = -\mu \quad (12a)$$

$$\lambda_5 = -\gamma_1 - \mu \quad (12b)$$

$$\lambda_6 = -\gamma_2 - \mu \quad (12c)$$

$$\lambda_7 = -\kappa - \mu \quad (12d)$$

$$\lambda_8 = \nu\beta_1/\mu - \gamma_1 - \mu \quad (12e)$$

$$\lambda_9 = \nu\beta_2/\mu - \gamma_2 - \mu \quad (12f)$$

As all parameters in the model are positive, the eigenvalues are always negative except for λ_8 and λ_9 . However, for $i = 1, 2$,

$$\nu\beta_i/\mu - \gamma_i - \mu < 0 \quad (13)$$

$$\iff \frac{\nu}{\mu} \frac{\beta_i}{\gamma_i + \mu} < 1 \quad (14)$$

$$\iff \mathcal{R}_{0,i} < 1 \quad (15)$$

where $\mathcal{R}_{0,i}$ is the basic reproduction number of the SIR model with vital dynamics for disease i . Hence, the DFE is asymptotically stable if the basic reproduction number of the SIR model is less than 1 for both diseases.

As the model features two diseases, another equilibria of interest are partial DFEs (PDFE), where only one disease is at DFE and the other disease has a nonzero amount of infected individuals. Suppose disease 2 (secondary disease such as WC) has no infectious individuals such that $X_{SI} = X_{RI} = 0$, then our system of equations for finding the equilibrium becomes

$$\nu - \beta_1(X_{IS} + X_{IR})X_{SS} - \mu X_{SS} = 0 \quad (16a)$$

$$-\beta_1(X_{IS} + X_{IR})X_{SR} - \mu X_{SR} = 0 \quad (16b)$$

$$\beta_1(X_{IS} + X_{IR})X_{SR} - \gamma_1 X_{IR} - \mu X_{IR} = 0 \quad (16c)$$

$$\beta_1(X_{IS} + X_{IR})X_{SS} - \gamma_1 X_{IS} - \mu X_{IS} = 0 \quad (16d)$$

$$\gamma_1 X_{IS} - \mu X_{RS} = 0 \quad (16e)$$

$$\theta\gamma_1 X_{IR} - \kappa X_A - \mu X_A = 0 \quad (16f)$$

$$\kappa X_A + (1 - \theta)\gamma_1 X_{IR} - \mu X_{RR} = 0 \quad (16g)$$

Combining eq. (16b) and eq. (16c) we have that $-\mu X_{SR} - (\gamma_1 + \mu)X_{IR} = 0$. Since $\mu, \gamma_1 > 0$ and $X_{SR}, X_{IR} \geq 0$, we have that $X_{SR} = X_{IR} = 0$. Substituting this into

eq. (16f) and eq. (16g) gives $X_A = 0$ and $X_{RR} = 0$, and the system now becomes

$$\nu - \beta_1 X_{IS} X_{SS} - \mu X_{SS} = 0 \quad (17a)$$

$$\beta_1 X_{IS} X_{SS} - \gamma_1 X_{IS} - \mu X_{IS} = 0 \quad (17b)$$

$$\gamma_1 X_{IS} - \mu X_{RS} = 0 \quad (17c)$$

However, these equations are just the SIR model with vital dynamics which is known to have an endemic equilibrium (EE). Solving this system gives PDFE₁ of

$$(X_{SS}^*, X_{SI}^*, X_{SR}^*, X_{IR}^*, X_{IS}^*, X_{RS}^*, X_{RI}^*, X_A^*, X_{RR}^*) = \left(\frac{\gamma_1 + \mu}{\beta_1}, 0, 0, 0, \frac{\nu}{\gamma_1 + \mu} - \frac{\mu}{\beta_1}, \frac{\gamma_1}{\mu} \left(\frac{\nu}{\gamma_1 + \mu} - \frac{\mu}{\beta_1} \right), 0, 0, 0 \right) \quad (18)$$

Similarly, suppose that disease 1 (measles) has no infectious individuals such that $X_{IS} = X_{IR} = 0$. Then the system of equations now becomes

$$\nu - \beta_2 (X_{SI} + X_{RI}) X_{SS} - \mu X_{SS} = 0 \quad (19a)$$

$$\beta_2 (X_{SI} + X_{RI}) X_{SS} - \gamma_2 X_{SI} - \mu X_{SI} = 0 \quad (19b)$$

$$\gamma_2 X_{SI} - \mu X_{SR} = 0 \quad (19c)$$

$$-\beta_2 (X_{SI} + X_{RI}) X_{RS} - \mu X_{RS} = 0 \quad (19d)$$

$$\beta_2 (X_{SI} + X_{RI}) (X_{RS} + X_A) - \gamma_2 X_{RI} - \mu X_{RI} = 0 \quad (19e)$$

$$-\beta_2 (X_{SI} + X_{RI}) X_A - \kappa X_A - \mu X_A = 0 \quad (19f)$$

$$\gamma_2 X_{RI} + \kappa X_A - \mu X_{RR} = 0 \quad (19g)$$

From eq. (19f), we get that either $X_A = 0$ or $\beta_2 (X_{SI} + X_{RI}) = -\kappa - \mu$. Combining the second equation with eq. (19b) gives $X_{SI} < 0$ at equilibrium, which we are not interested in. Alternatively, if $X_A = 0$, then combining eq. (19d) and eq. (19e) gives $-\mu X_{RS} - \gamma_2 X_{RI} - \mu X_{RI} = 0$. Since $\mu, \gamma_2 > 0$ and all the compartments are nonnegative, $X_{RS} = X_{RI} = 0$. This also means that $X_{RR} = 0$ according to eq. (19g). The system now simplifies to

$$\nu - \beta_2 X_{SI} X_{SS} - \mu X_{SS} = 0 \quad (20a)$$

$$\beta_2 X_{SI} X_{SS} - \gamma_2 X_{SI} - \mu X_{SI} = 0 \quad (20b)$$

$$\gamma_2 X_{SI} - \mu X_{SR} = 0 \quad (20c)$$

which is once again just the SIR model with vital dynamics. This gives us PDFE₂ of

$$(X_{SS}^*, X_{SI}^*, X_{SR}^*, X_{IR}^*, X_{IS}^*, X_{RS}^*, X_{RI}^*, X_A^*, X_{RR}^*) = \left(\frac{\gamma_2 + \mu}{\beta_2}, \frac{\nu}{\gamma_2 + \mu} - \frac{\mu}{\beta_2}, \frac{\gamma_2}{\mu} \left(\frac{\nu}{\gamma_2 + \mu} - \frac{\mu}{\beta_2} \right), 0, 0, 0, 0, 0, 0 \right) \quad (21)$$

The Jacobian of the system was used again to analyze local stability. Substituting $PDFE_1$ into the Jacobian gives the matrix:

$$J(PDFE_1) = \begin{bmatrix} -\mu - \beta_1 \Delta_1 & -\Delta_2 & 0 & -\mu - \gamma_1 & -\mu - \gamma_1 & 0 & -\Delta_2 & 0 & 0 \\ 0 & -\mu - \gamma_2 + \delta_2 & 0 & 0 & 0 & 0 & \Delta_2 & 0 & 0 \\ 0 & \gamma_2 & -\mu - \beta_1 \Delta_1 & 0 & 0 & 0 & 0 & 0 & 0 \\ 0 & 0 & \beta_1 \Delta_1 & -\mu - \gamma_1 & 0 & 0 & 0 & 0 & 0 \\ \beta_1 \Delta_1 & 0 & 0 & \mu + \gamma_1 & 0 & 0 & 0 & 0 & 0 \\ 0 & -\beta_2 \gamma_1 \Delta_1 / \mu & 0 & 0 & \gamma_1 & -\mu & -\beta_2 \gamma_1 \Delta_1 / \mu & 0 & 0 \\ 0 & \beta_2 \gamma_1 \Delta_1 / \mu & 0 & 0 & 0 & 0 & -\mu - \gamma_2 - \beta_2 \gamma_1 \Delta_1 / \mu & 0 & 0 \\ 0 & 0 & 0 & \gamma_1 \theta & 0 & 0 & 0 & -\mu - \kappa & 0 \\ 0 & 0 & 0 & \gamma_1 (1 - \theta) & 0 & 0 & \gamma_2 & \kappa & -\mu \end{bmatrix} \quad (22)$$

where $\Delta_1 = \frac{\nu}{\gamma_2 + \mu} - \frac{\mu}{\beta_1}$ and $\Delta_2 = \frac{\beta_2(\gamma_1 + \mu)}{\beta_1}$. The eigenvalues of this matrix are given by

$$\lambda_{1,2} = -\mu \quad (23a)$$

$$\lambda_3 = -\gamma_1 - \mu \quad (23b)$$

$$\lambda_4 = -\gamma_2 - \mu \quad (23c)$$

$$\lambda_5 = \kappa - \mu \quad (23d)$$

$$\lambda_6 = -\frac{\nu \beta_1}{\nu + \gamma_1} \quad (23e)$$

$$\lambda_7 = \frac{-\nu \beta_1 - \sqrt{\Delta_3}}{2(\beta_1 + \gamma_1)} \quad (23f)$$

$$\lambda_8 = \frac{-\nu \beta_1 + \sqrt{\Delta_3}}{2(\beta_1 + \gamma_1)} \quad (23g)$$

$$\lambda_9 = \frac{\beta_2 \mu^2 (\mu + \gamma_1) - \beta_1 (\mu (\mu + \gamma_1) (\mu + \gamma_2) - \nu \beta_2 \gamma_1)}{\beta_1 \mu (\mu + \gamma_1)} \quad (23h)$$

where $\Delta_3 = \nu^2 \beta_1^2 - 4\nu \beta_1 (\mu + \gamma_1)^2 + 4\mu (\mu + \gamma_1)^3$. As the parameters in the model are positive, eigenvalues $\lambda_1 \sim \lambda_6$ are always negative. We now consider sufficient conditions for $\lambda_7 \sim \lambda_9$ to be negative. λ_7 will either be a negative real value or have a negative real part depending on the sign of Δ_3 . Similarly, λ_8 has negative real part if $\Delta_3 \leq 0$. If $\Delta_3 > 0$, then λ_8 will be a negative real value if

$$\nu \beta_1 > \sqrt{\nu^2 \beta_1^2 - 4\nu \beta_1 (\mu + \gamma_1)^2 + 4\mu (\mu + \gamma_1)^3} \quad (24)$$

$$\iff 0 > -4\nu \beta_1 (\mu + \gamma_1)^2 + 4\mu (\mu + \gamma_1)^3 \quad (25)$$

$$\iff \nu \beta_1 > \mu (\mu + \gamma_1) \quad (26)$$

$$\iff \frac{\nu \beta_1}{\mu \gamma_1 + \mu} > 1 \quad (27)$$

$$\iff R_{0,1} > 1 \quad (28)$$

For λ_9 , assume that $\mathcal{R}_{0,1} > 1$ and $\mathcal{R}_{0,2} < 1$. Then we have that

$$\frac{\nu\beta_1}{\mu(\mu + \gamma_1)} > 1 \iff \nu\beta_1\beta_2\gamma_1 > \beta_2\mu\gamma_1(\mu + \gamma_1) \quad (29)$$

and similarly putting together both expression gives

$$\beta_1\mu\gamma_1(\mu + \gamma_2) > \nu\beta_1\beta_2\gamma_1 > \beta_2\mu\gamma_1(\mu + \gamma_1) \quad (30)$$

Hence, for $\lambda_9 < 0$, it should satisfy

$$\beta_2\mu^2(\mu + \gamma_1) < \beta_1\mu(\mu + \gamma_1)(\mu + \gamma_2) - \nu\beta_1\beta_2\gamma_1 \quad (31)$$

$$\iff \beta_2\mu^2(\mu + \gamma_1) < \beta_1\mu(\mu + \gamma_1)(\mu + \gamma_2) - \beta_2\mu\gamma_1(\mu + \gamma_1) \quad (32)$$

$$\iff \beta_2\mu < \beta_1(\mu + \gamma_2) - \beta_2\gamma_1 \quad (33)$$

$$\iff \beta_2(\mu + \gamma_1) < \beta_1(\mu + \gamma_2) \quad (34)$$

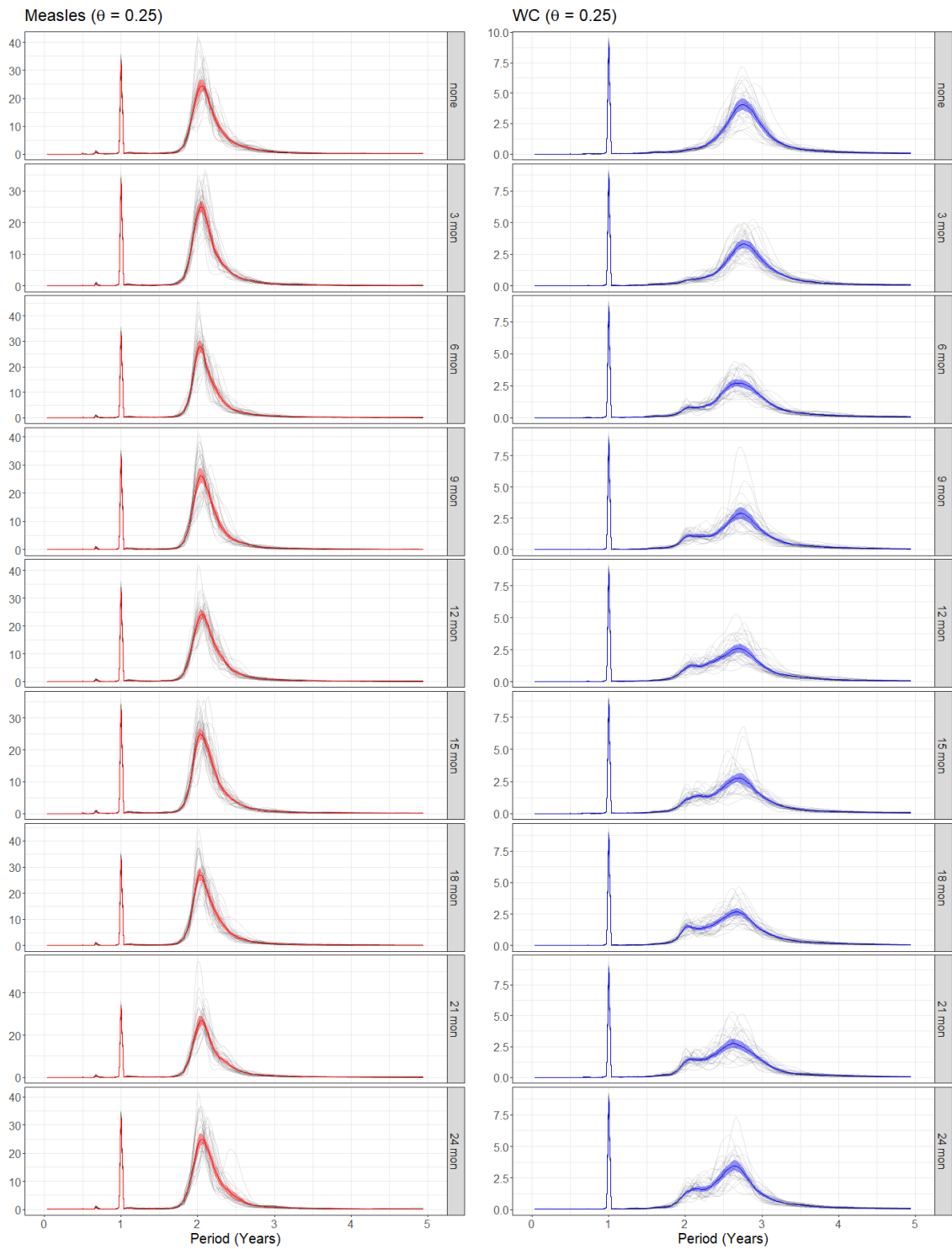
However, from the initial assumption, $\beta_1\mu\gamma_1(\mu + \gamma_2) > \beta_2\mu\gamma_1(\mu + \gamma_1) \iff \beta_1(\mu + \gamma_2) > \beta_2(\mu + \gamma_1)$. Hence, all eigenvalues have negative real parts when $\mathcal{R}_{0,1} > 1$ and $\mathcal{R}_{0,2} < 1$, meaning PDFE₁ is asymptotically stable when these conditions are met. Using similar reasoning, it can also be concluded that PDFE₂ is asymptotically stable if $\mathcal{R}_{0,1} < 1$ and $\mathcal{R}_{0,2} > 1$ (as it results in the eigenvalues of the same form with just a change of variables).

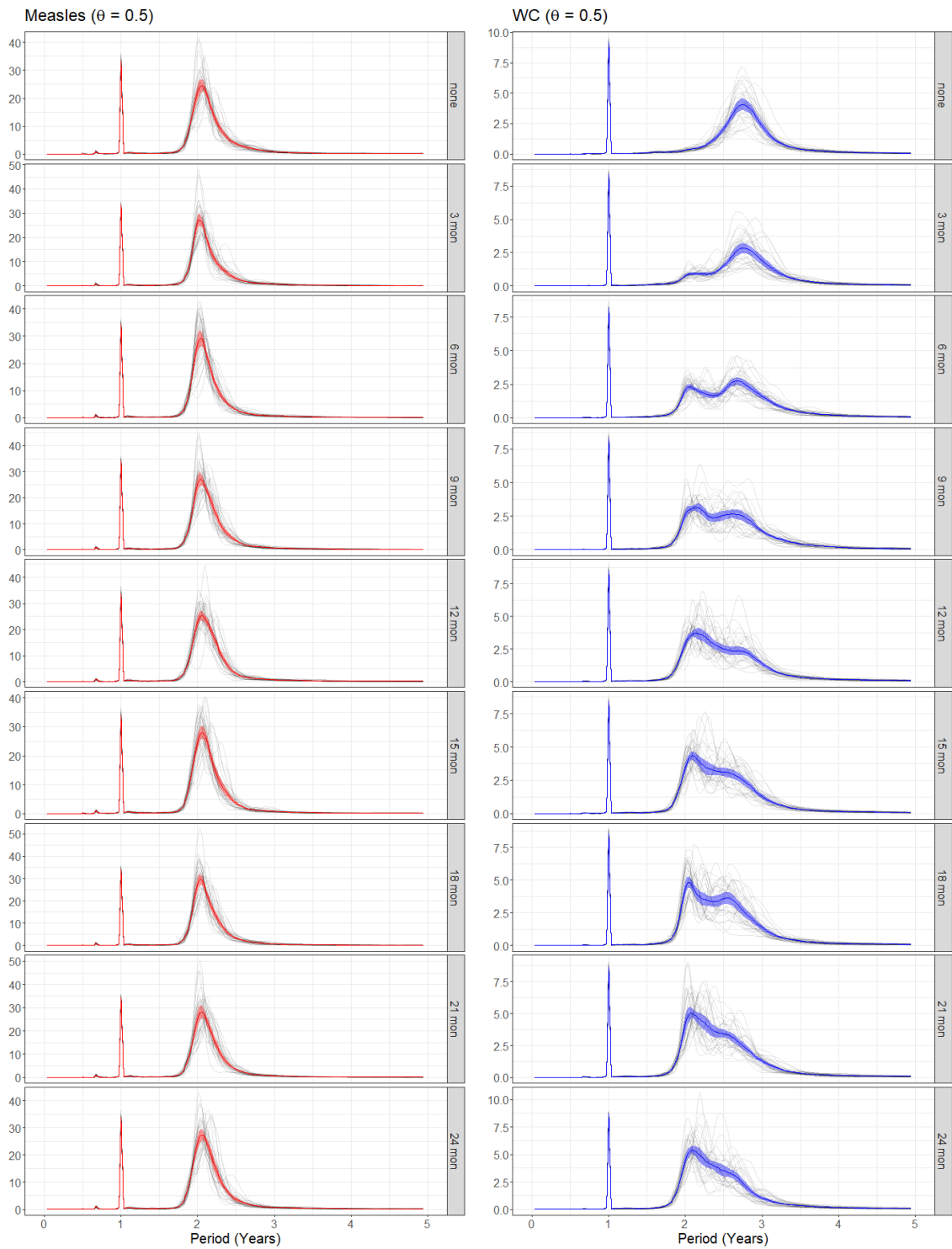
This analysis showed that it is possible to reach a DFE where only one of the the diseases, or both diseases, have faded out from the population. Furthermore, the criteria for local stability of the DFEs closely resembles that of a simple SIR model for these diseases.

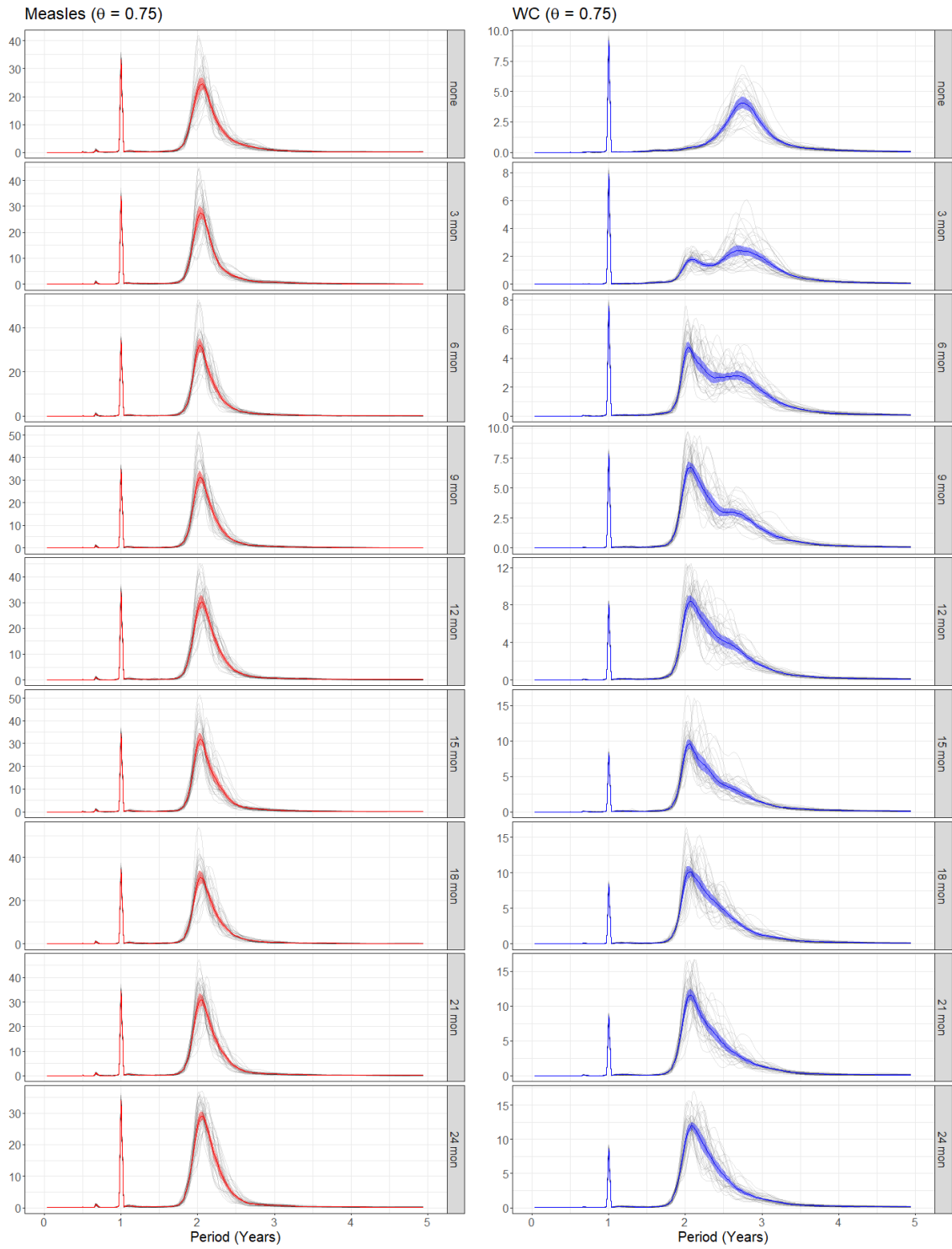
B Supplementary Figures

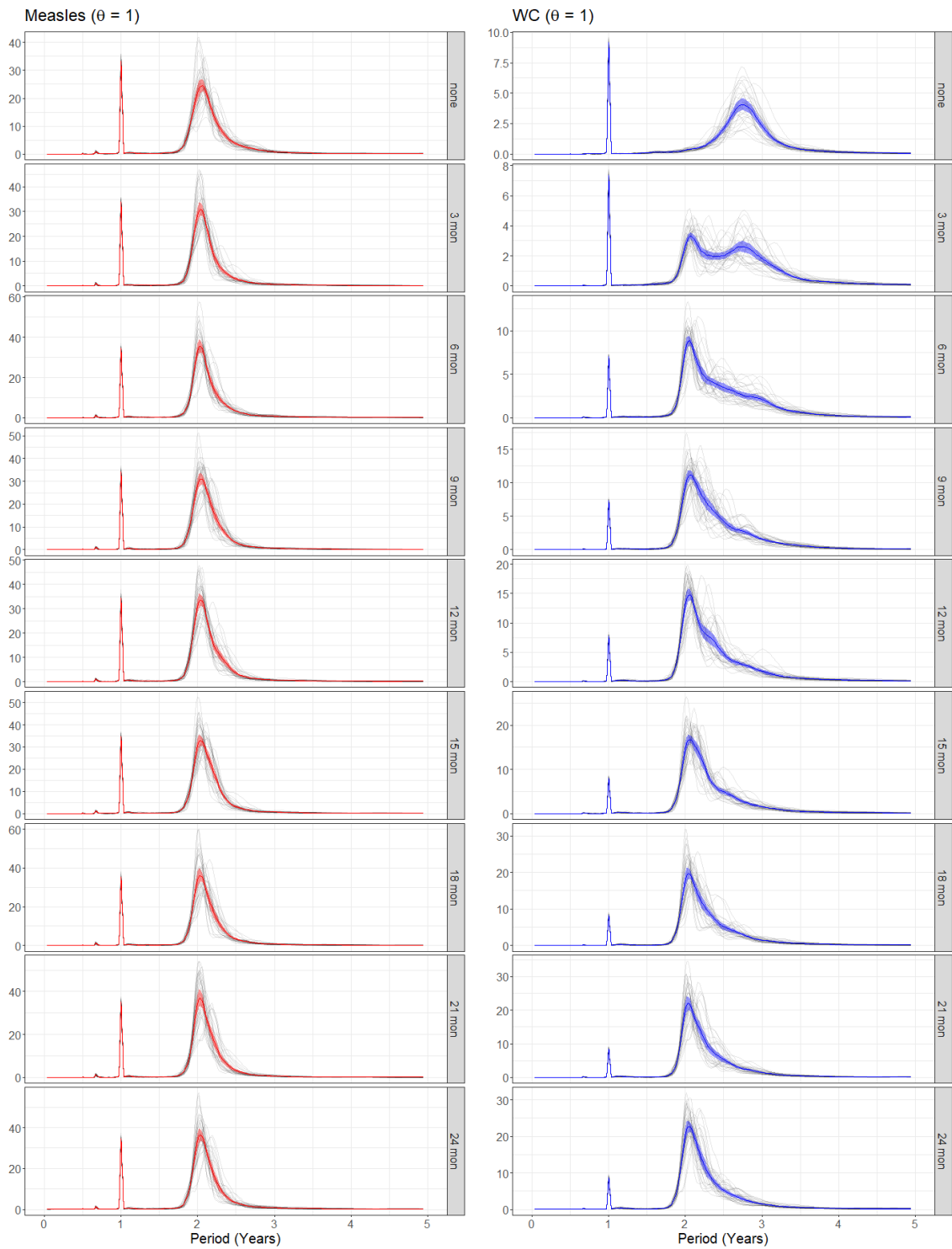
This section provides periodogram results for the simulations from Section 3.5 and Section 4.3 for additional θ and $1/\kappa$ values.

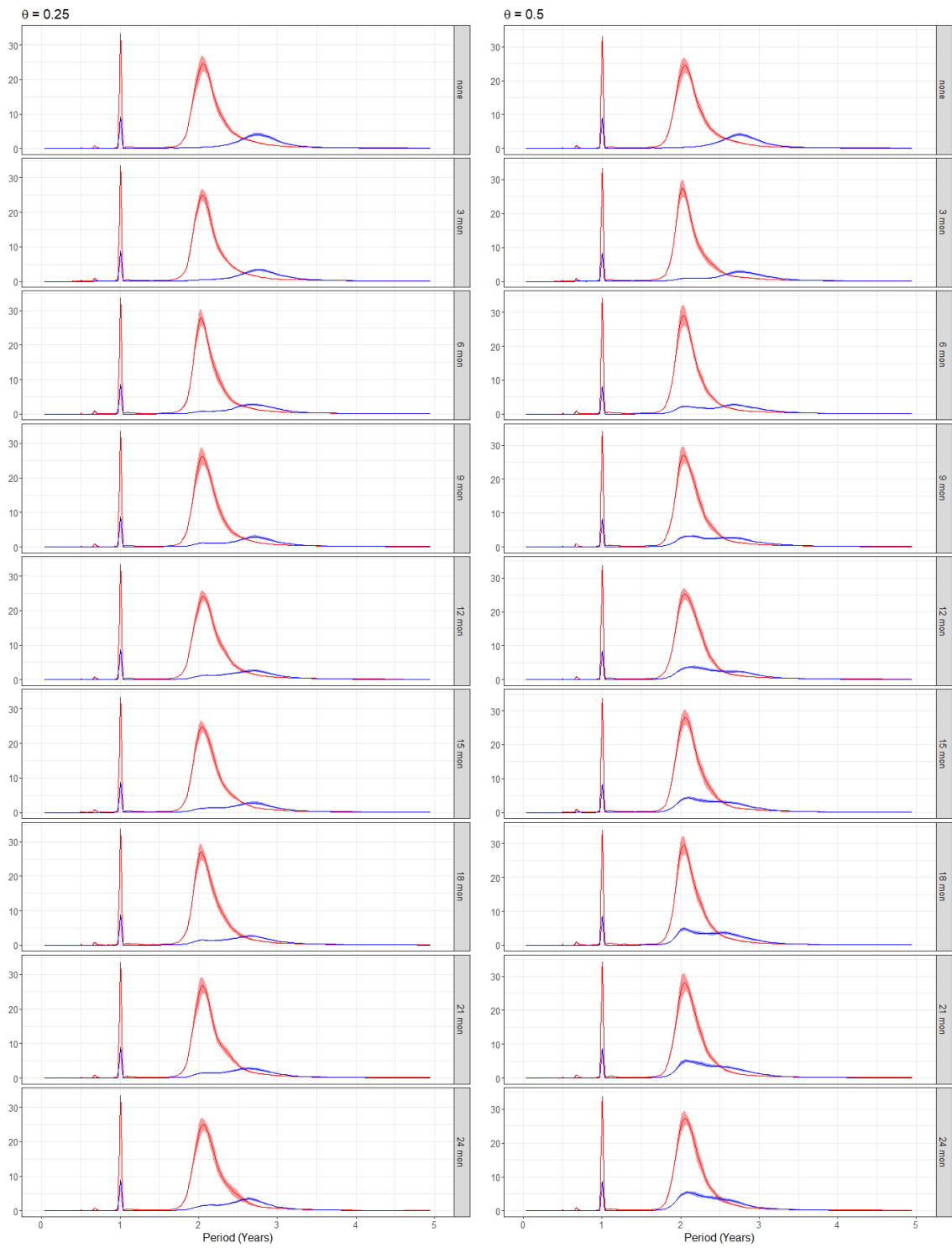
B.1 Simulations with $N = 8 \times 10^5$











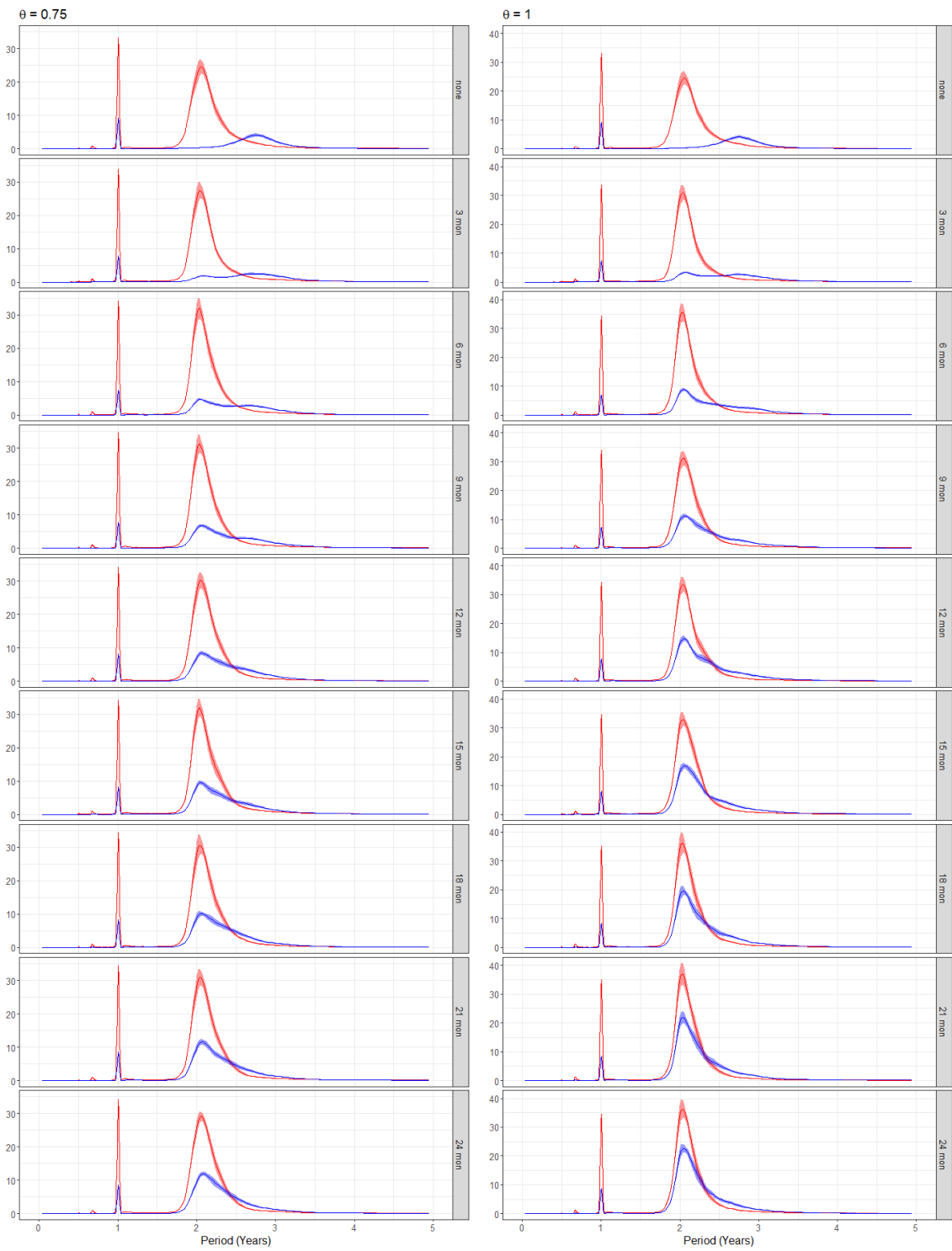
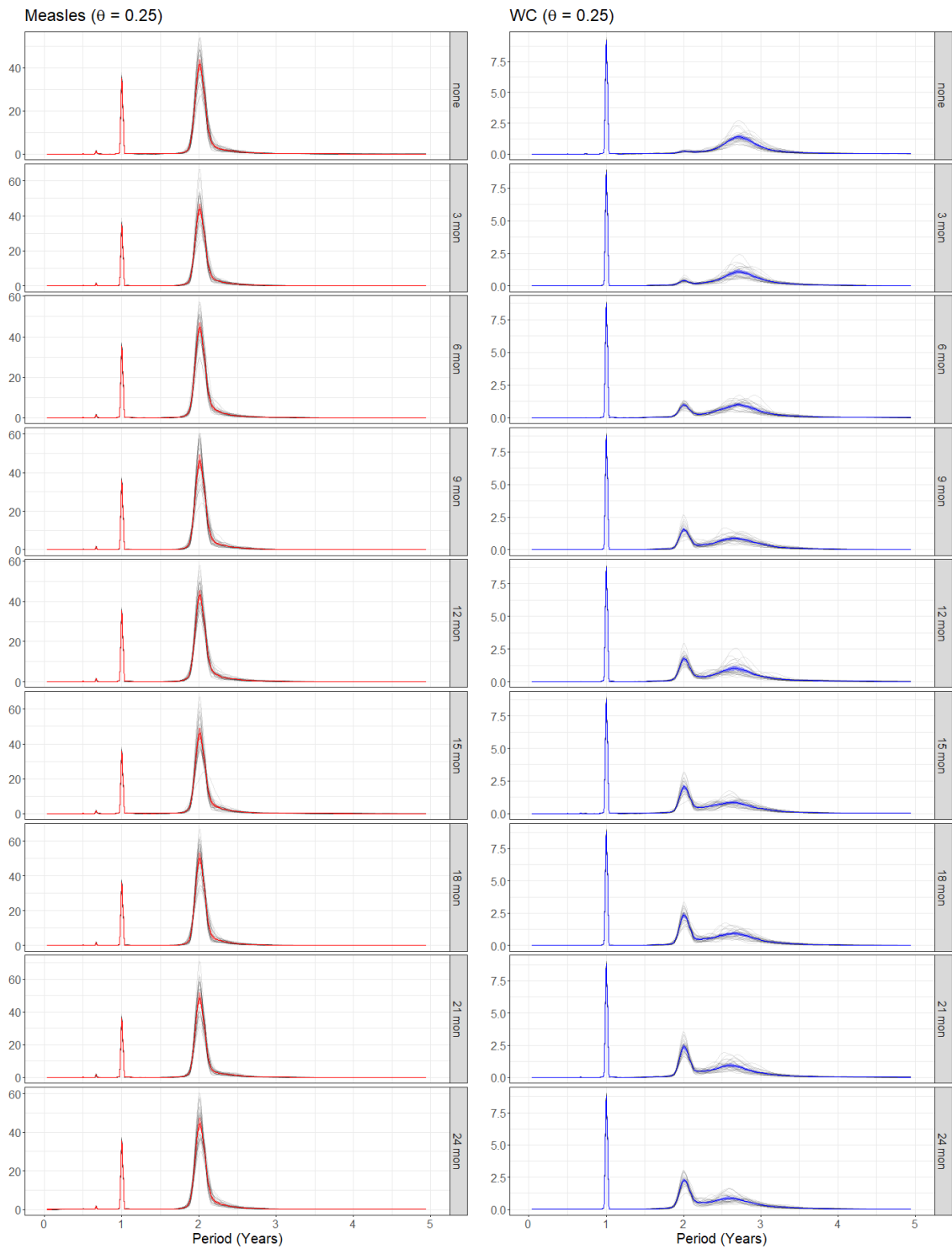
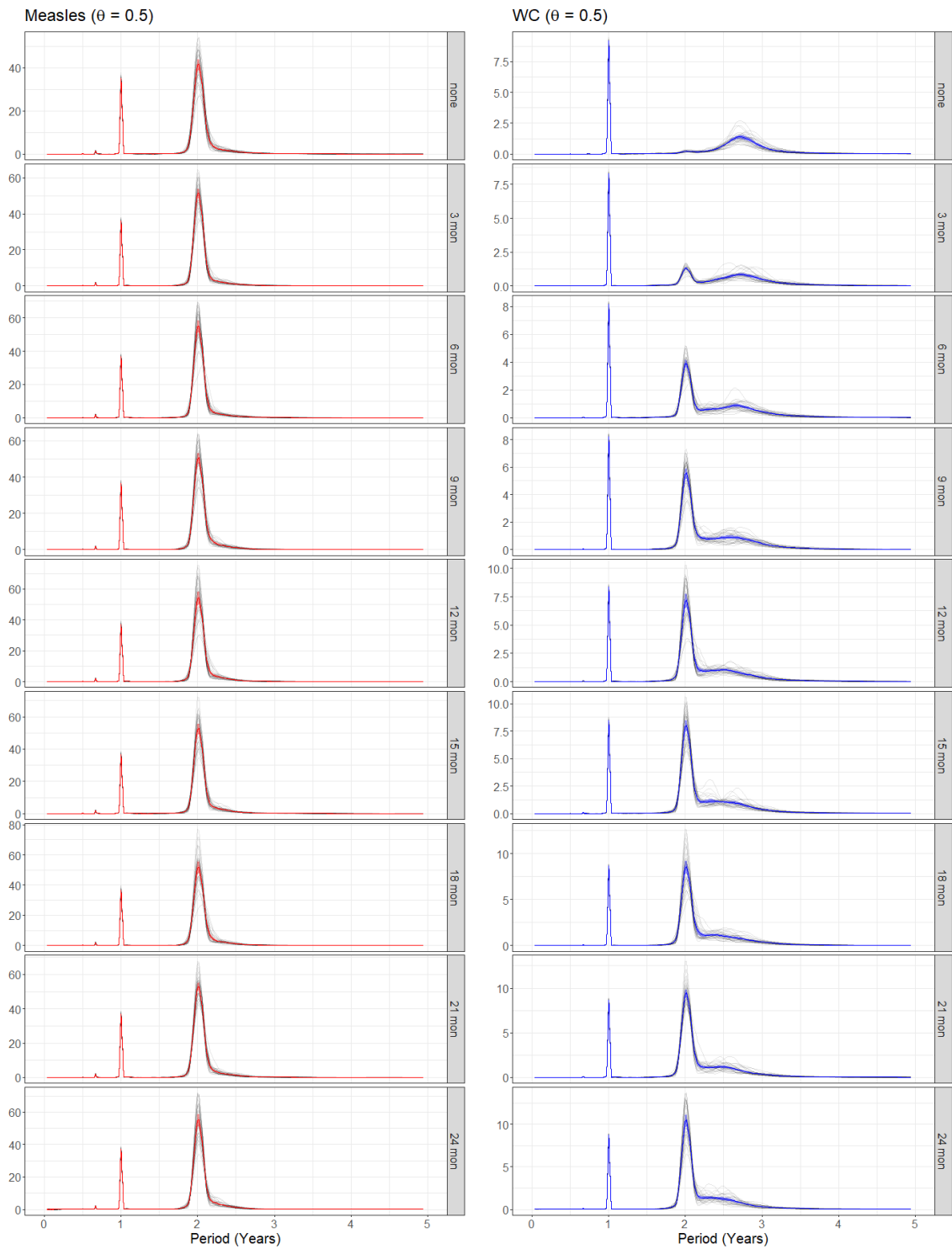
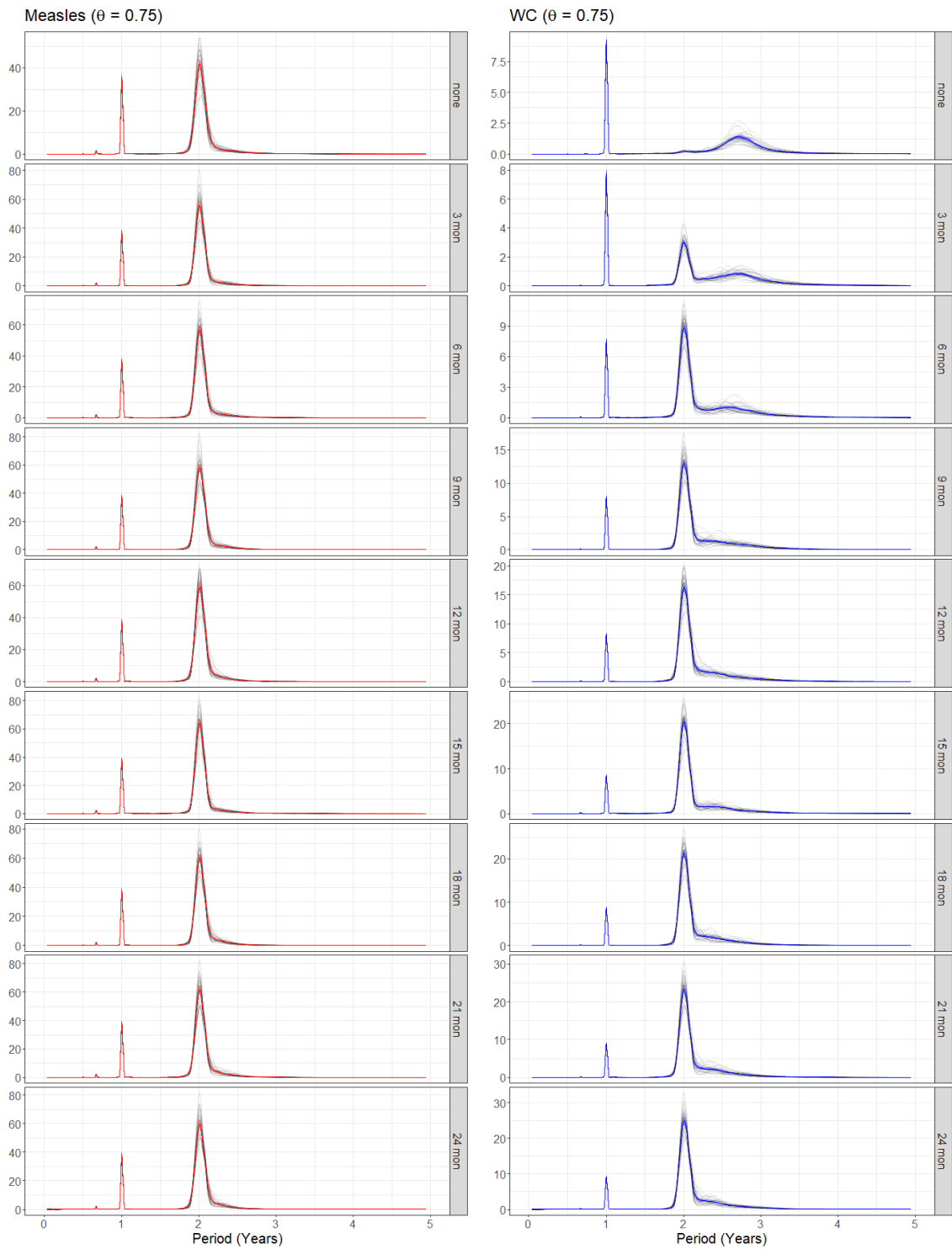


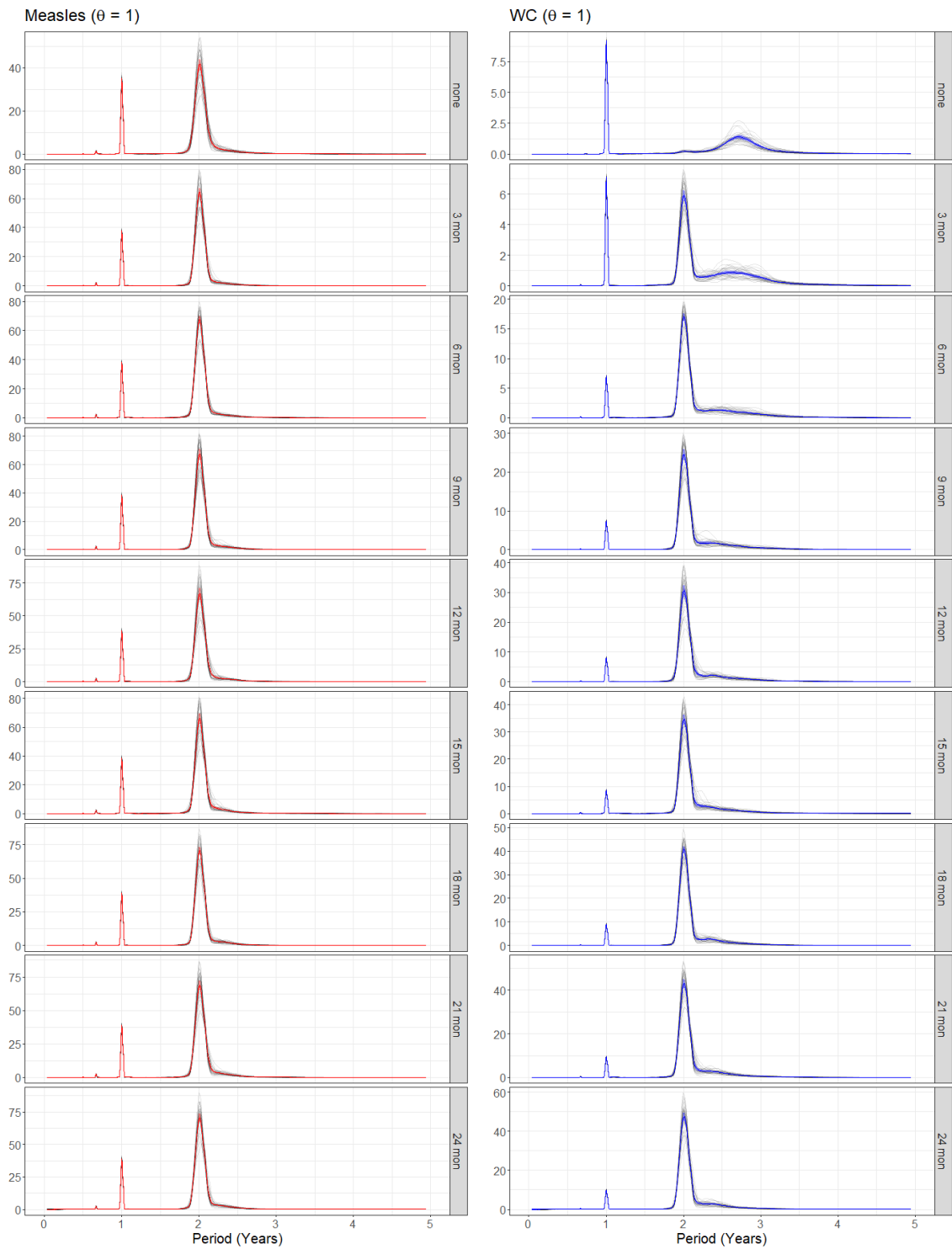
Figure 29: Periodograms of disease incidence from IA model with $N = 8 \times 10^5$. Periodograms were computed using the square-root-transformed normalized measles (red) and WC (blue) incidence weekly series extracted from stochastic simulations. Simulations were done for $\theta = 0.25, 0.5, 0.75, 1$ with $1/\kappa$ values between 0 and 24 months. A total of 30 realizations were done for each set of parameters. Solid colored lines indicate the average periodogram and colored bands represent 95% confidence intervals

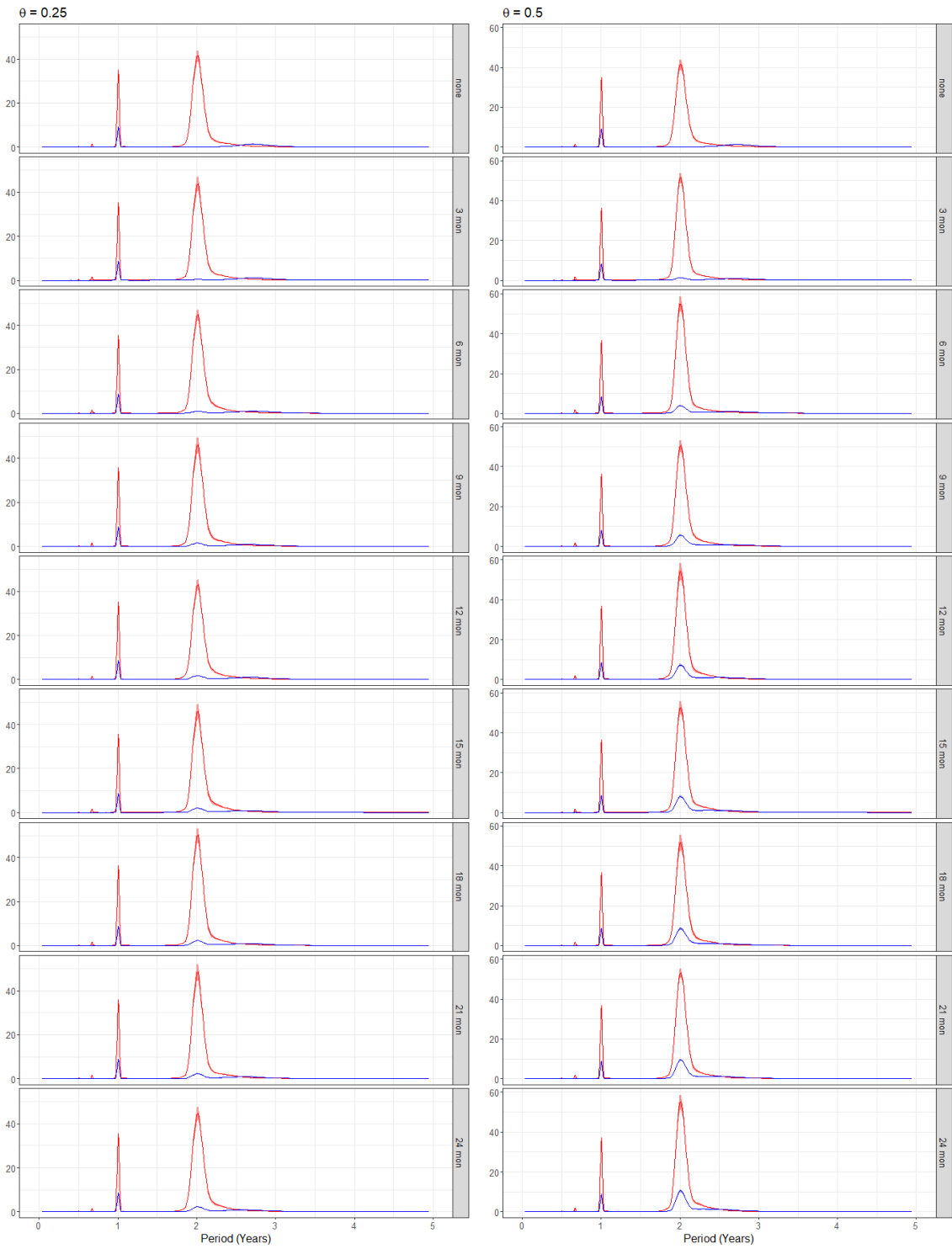
B.2 Simulations with $N = 2.5 \times 10^6$











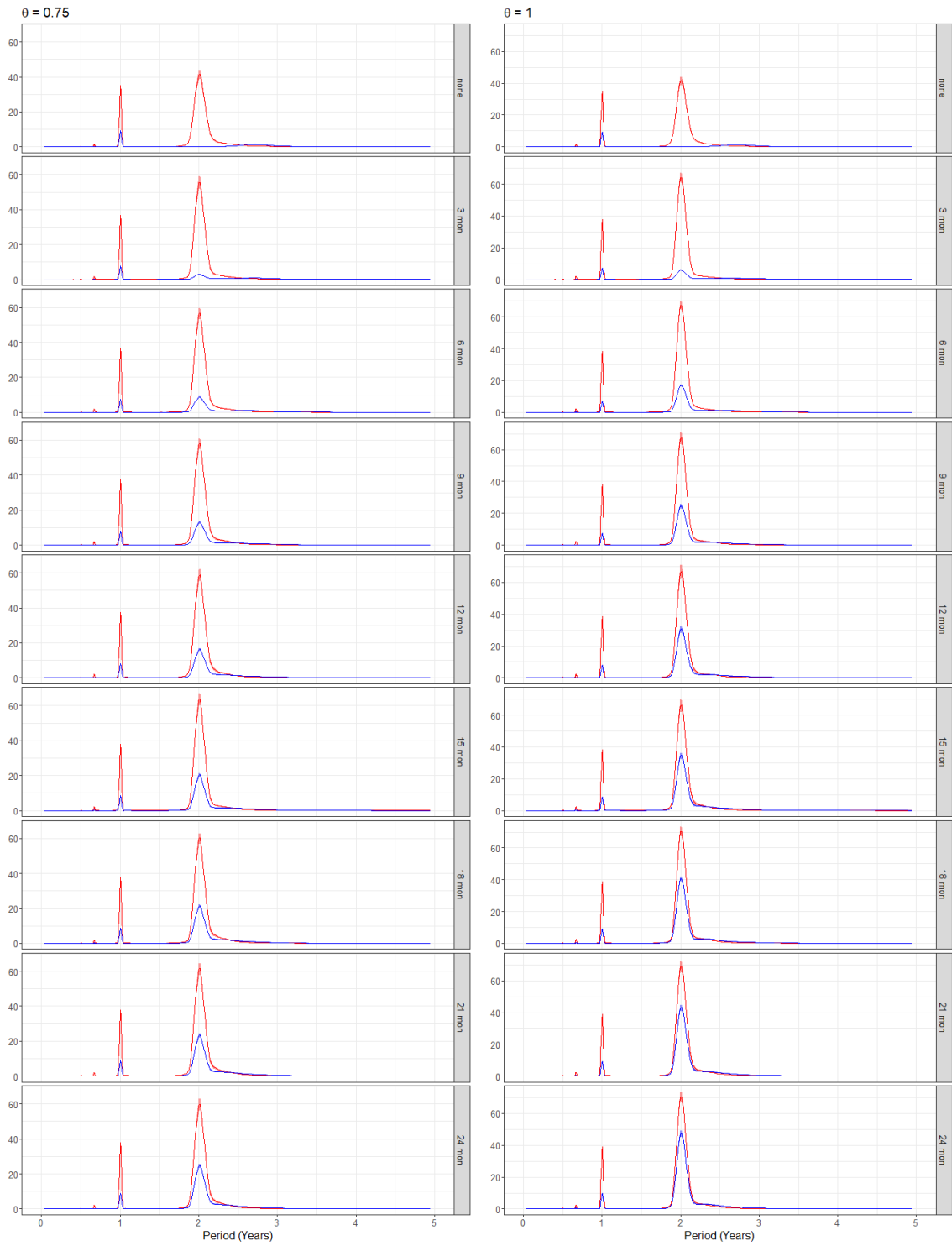
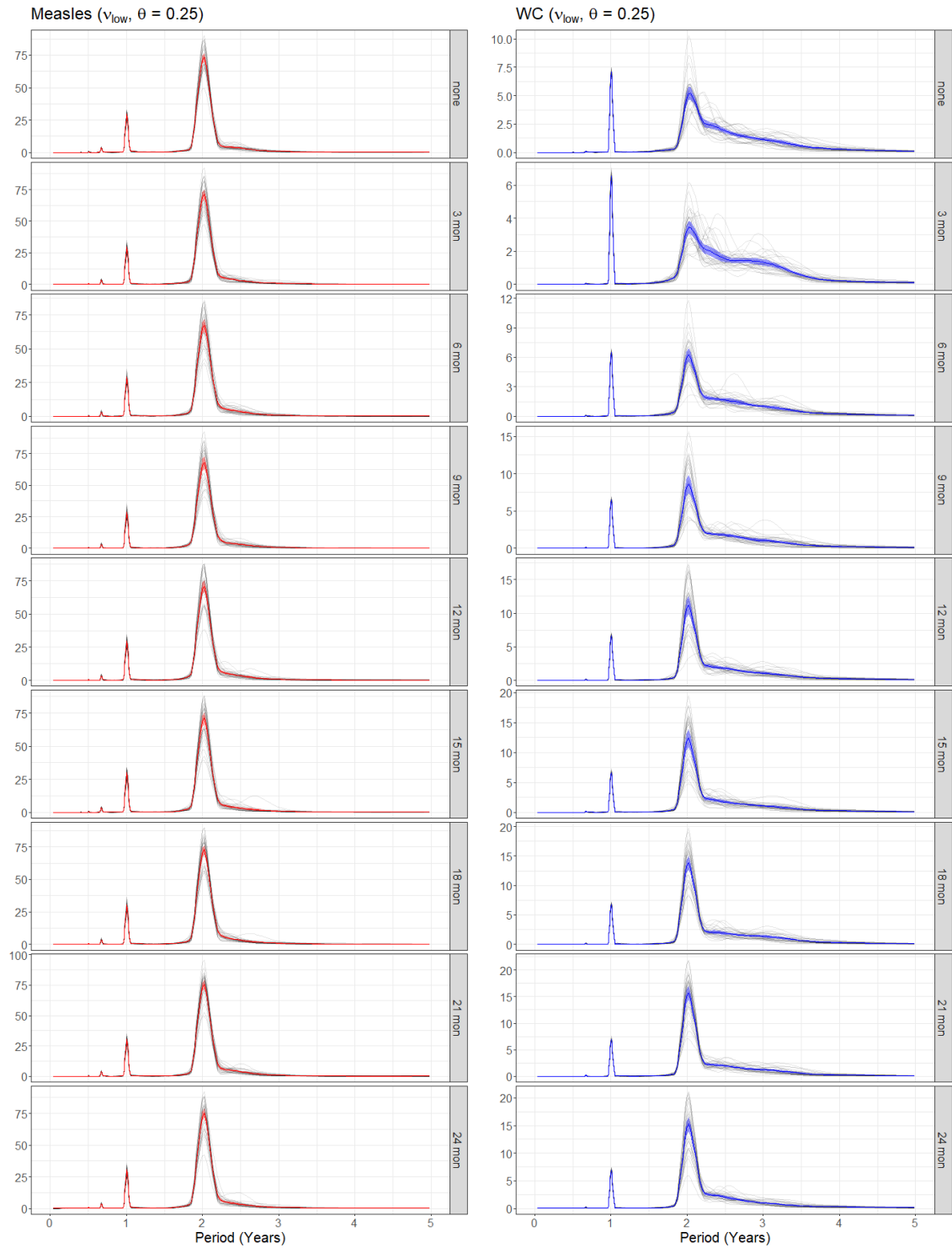
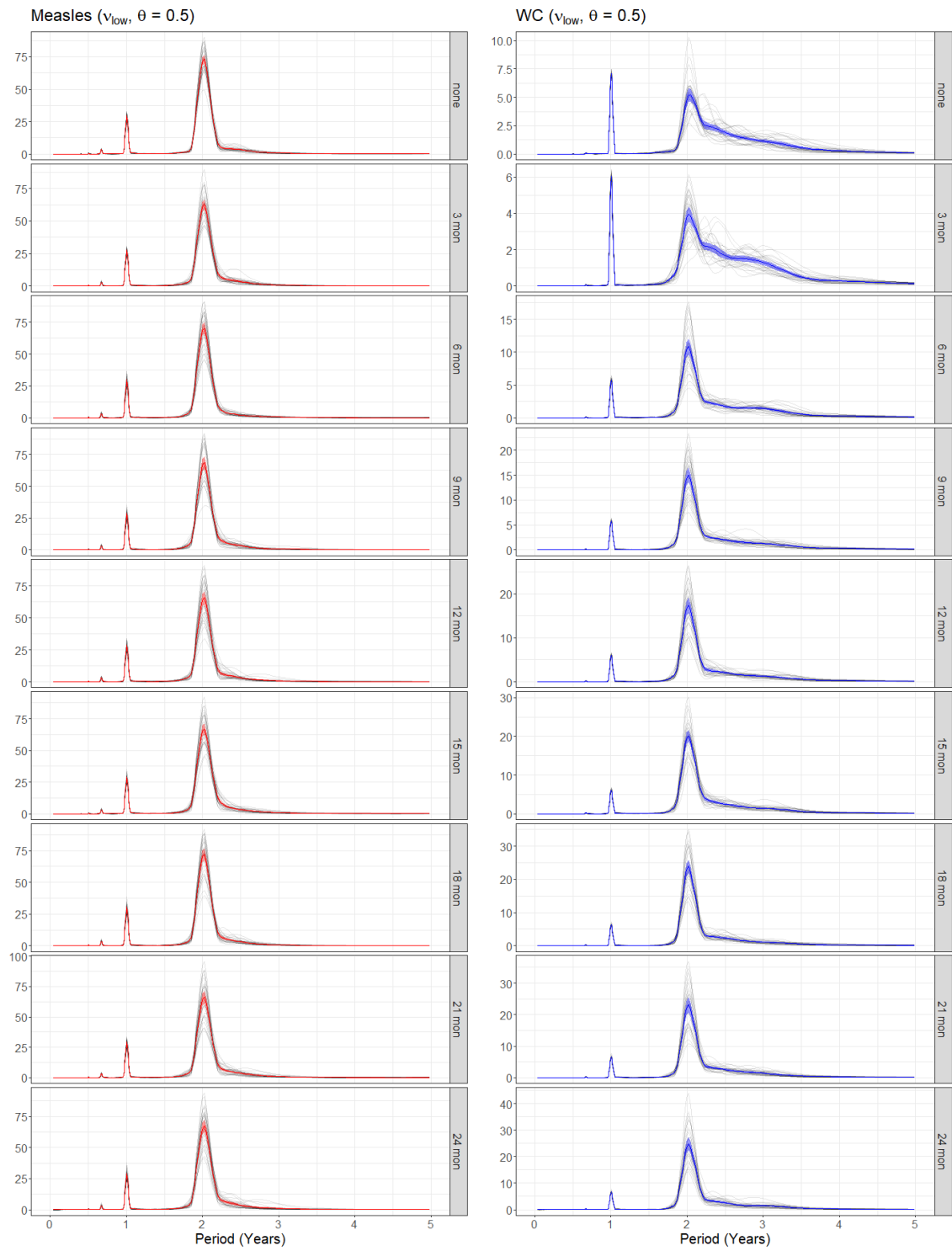


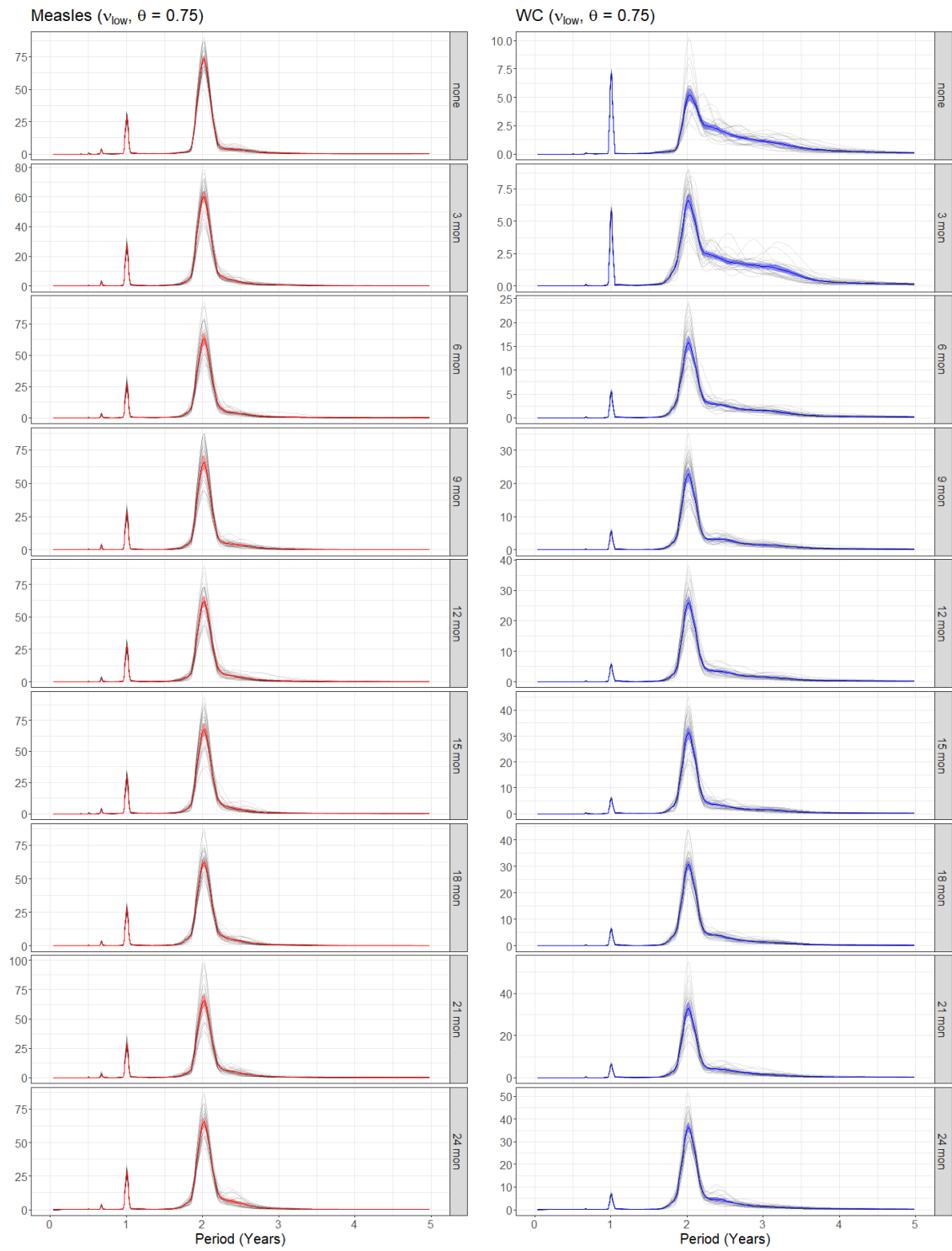
Figure 30: Periodograms of disease incidence from IA model with $N = 2.5 \times 10^6$. Periodograms were computed using the square-root-transformed normalized measles (red) and WC (blue) incidence weekly series extracted from stochastic simulations. Simulations were done for $\theta = 0.25, 0.5, 0.75, 1$ with $1/\kappa$ values between 0 and 24 months. A total of 30 realizations were done for each set of parameters. Solid colored lines indicate the average periodogram and colored bands represent 95% confidence intervals

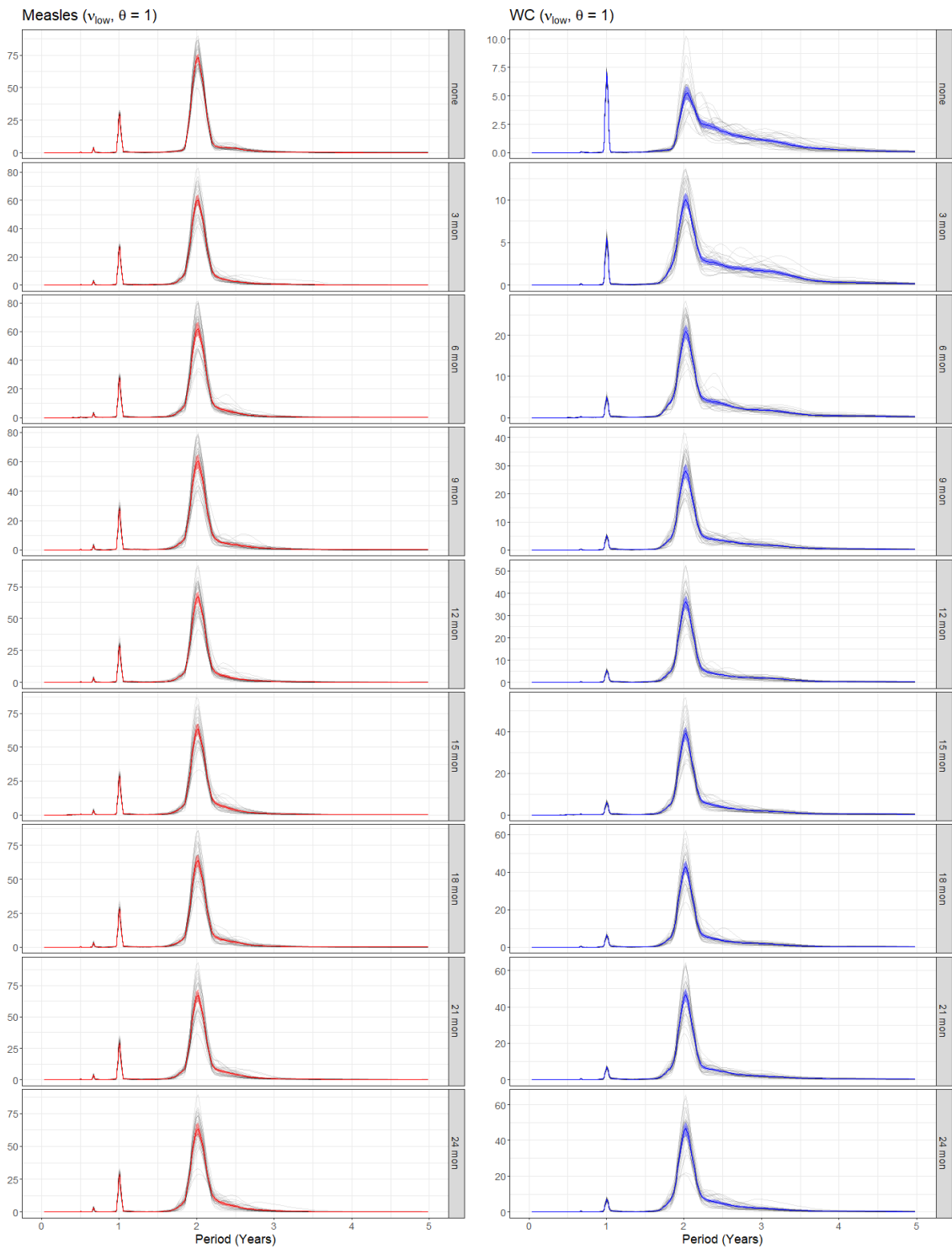
B.3 Simulations with $\nu_{\text{low}}(t)$ and $\mu(t)$

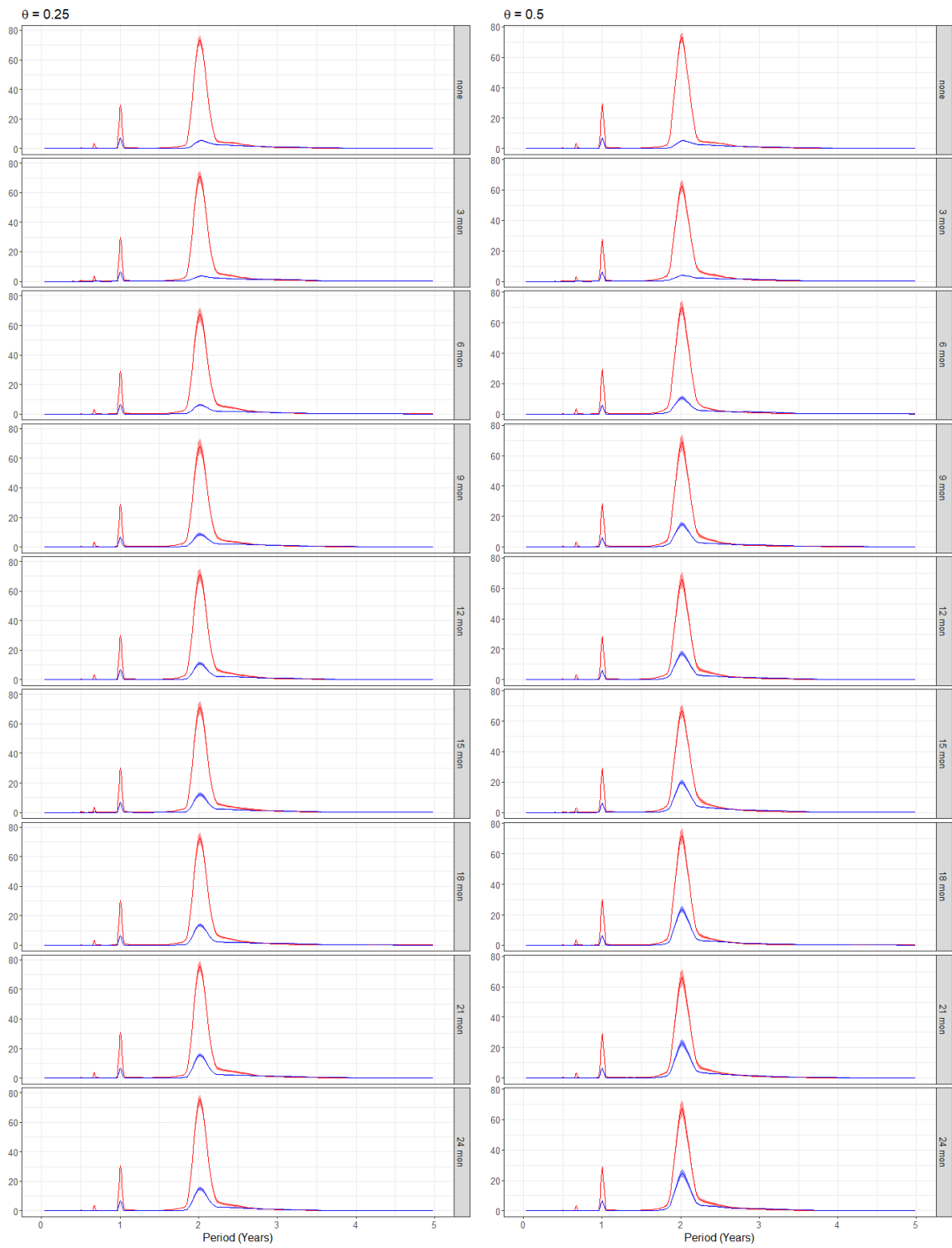
B.3.1 1750–1900











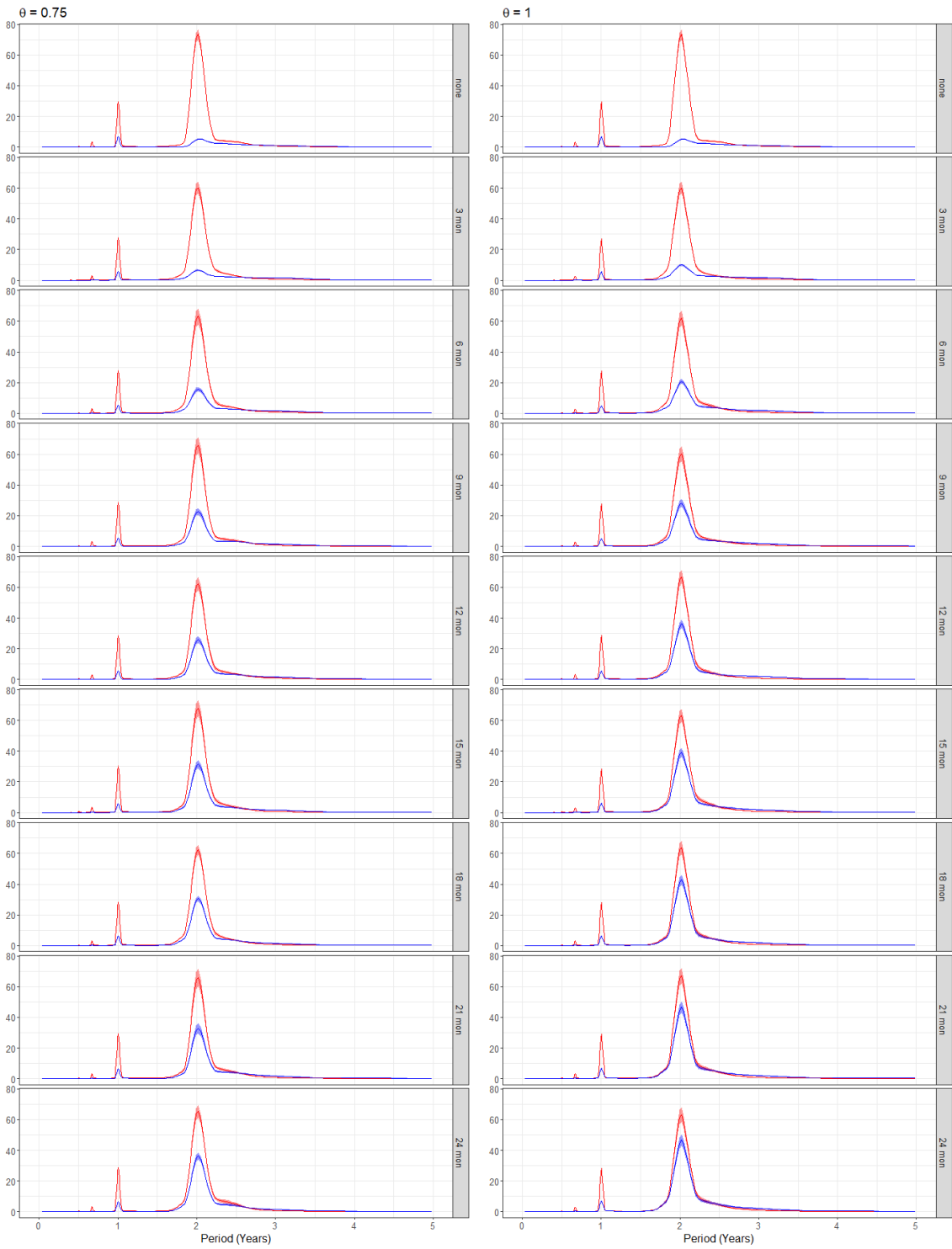
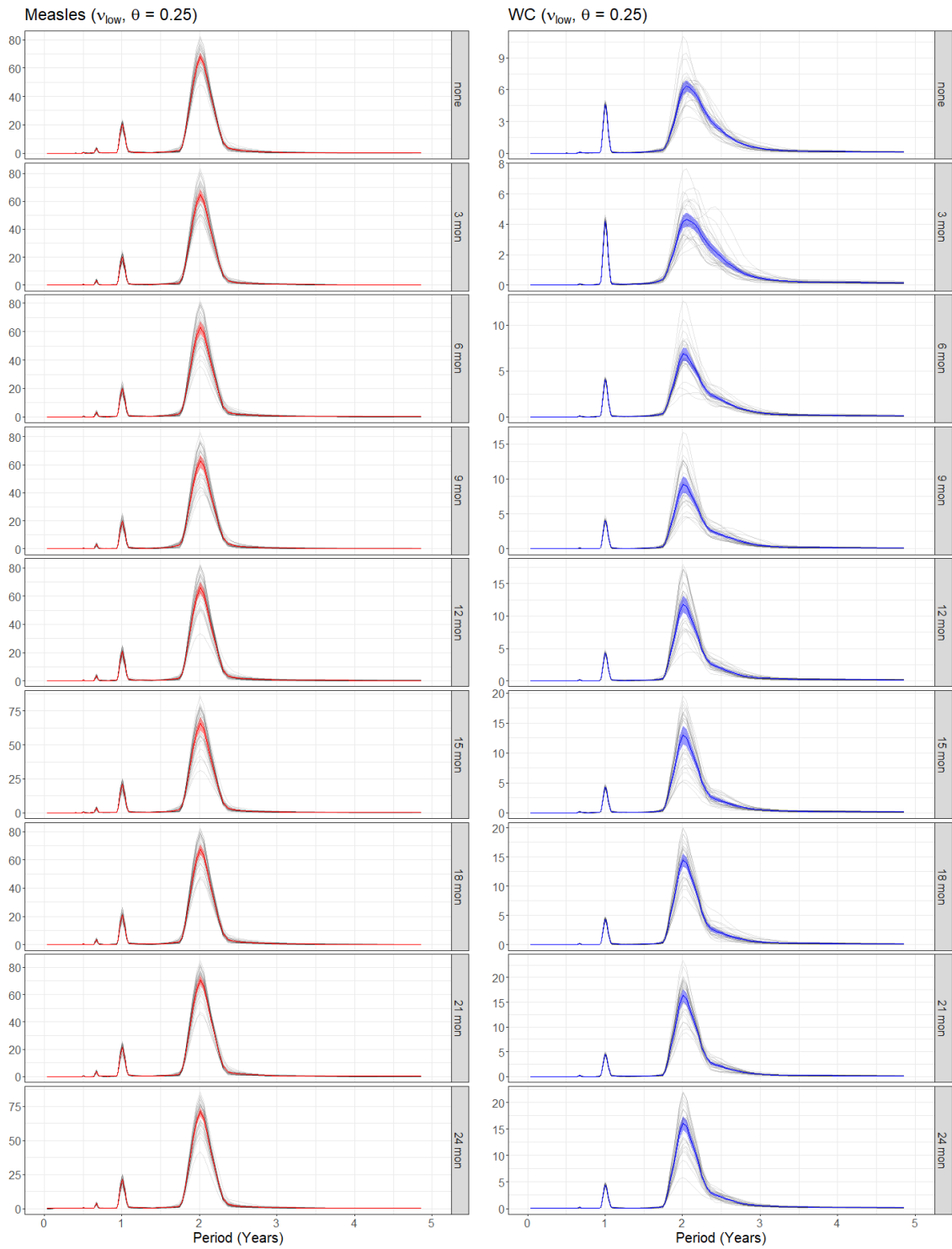
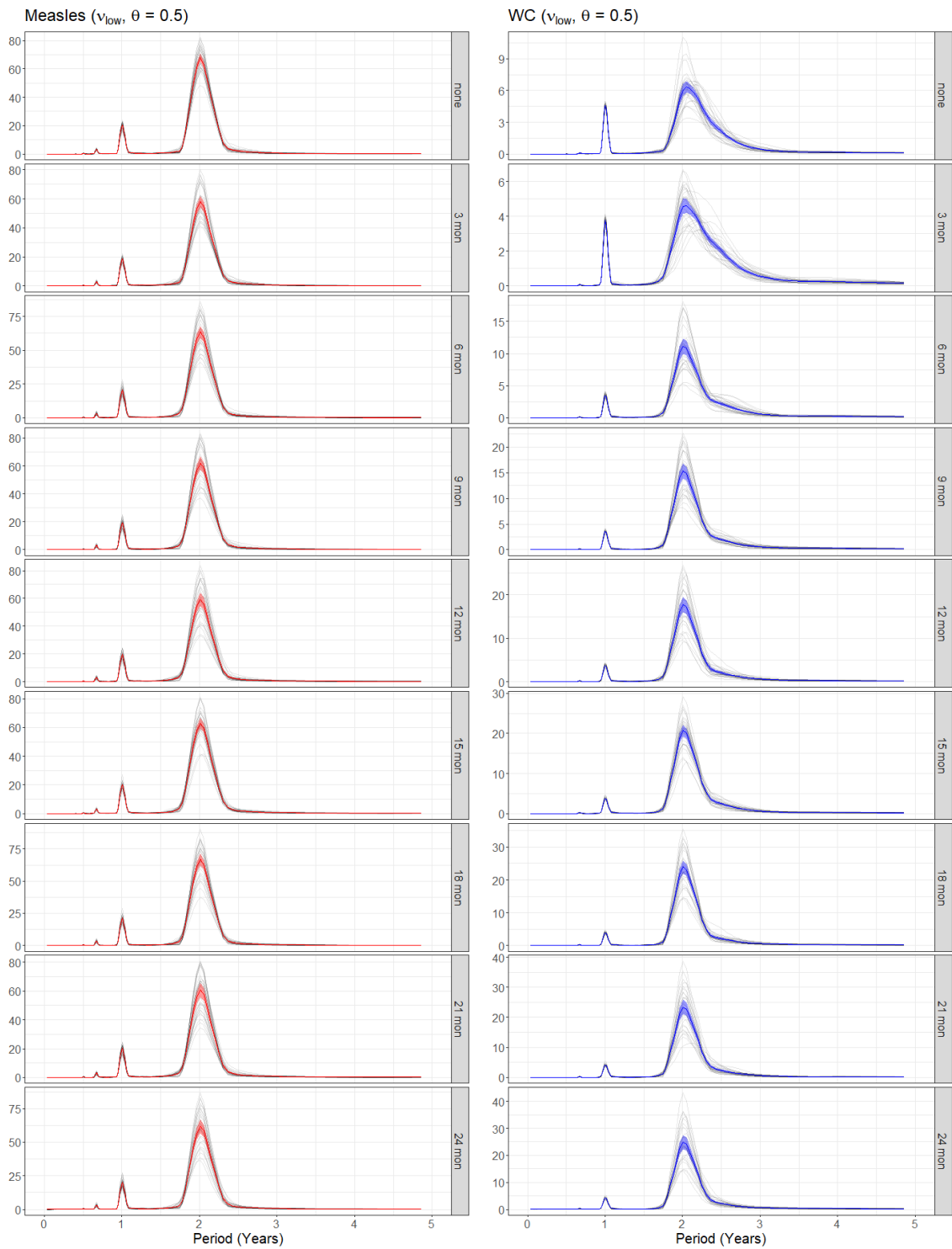
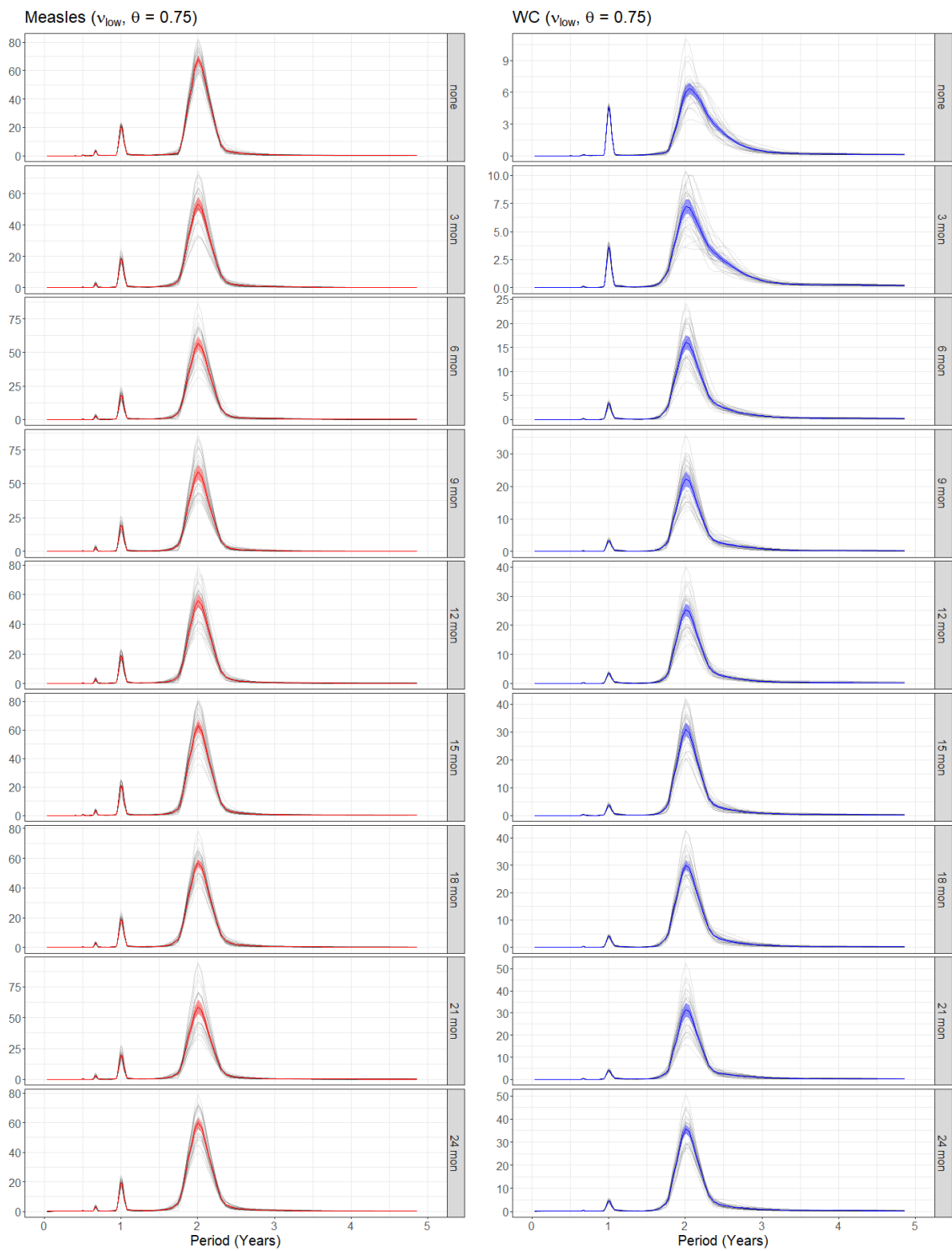


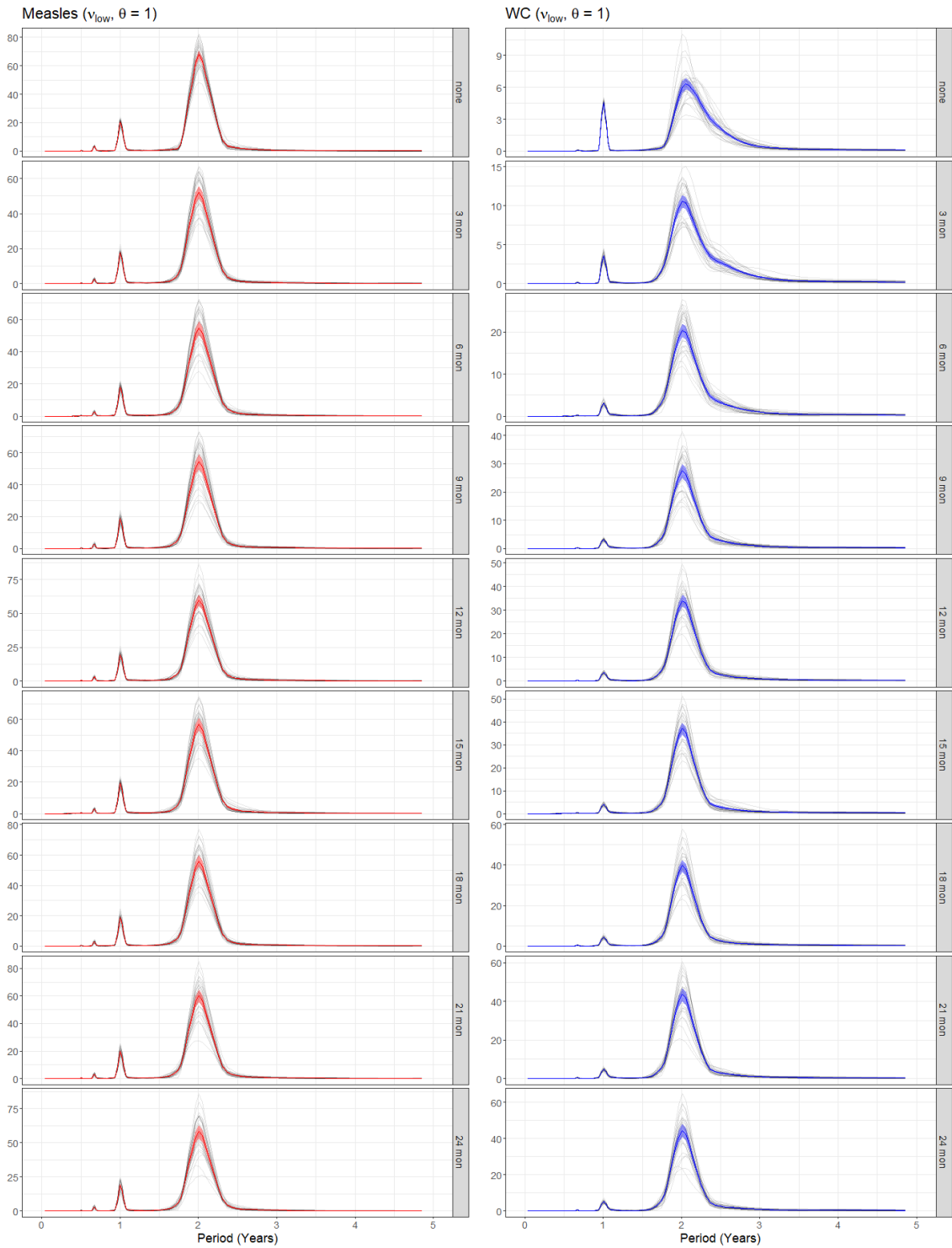
Figure 31: Periodograms of disease incidence from IA model with time-varying ν_{low} and μ . Time-varying parameters were calculated using London data between 1750 - 1900 as described in Section 4.1. Periodograms were computed using the square-root-transformed normalized measles (red) and WC (blue) incidence weekly series extracted from stochastic simulations. Simulations were done for $\theta = 0.25, 0.5, 0.75, 1$ with $1/\kappa$ values between 0 and 24 months. A total of 30 realizations were done for each set of parameters. Solid colored lines indicate the average periodogram and colored bands represent 95% confidence intervals

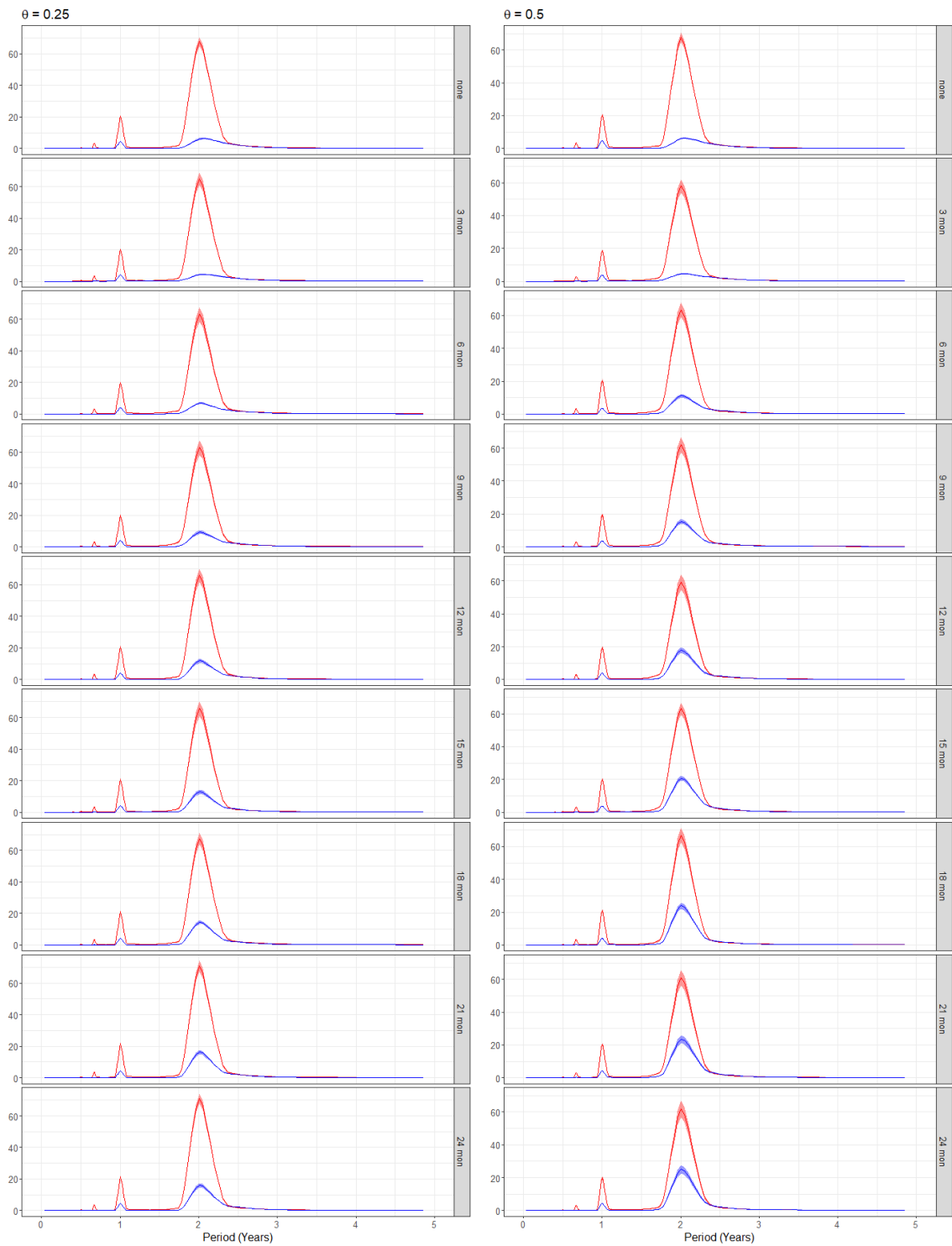
B.3.2 LBoM Period











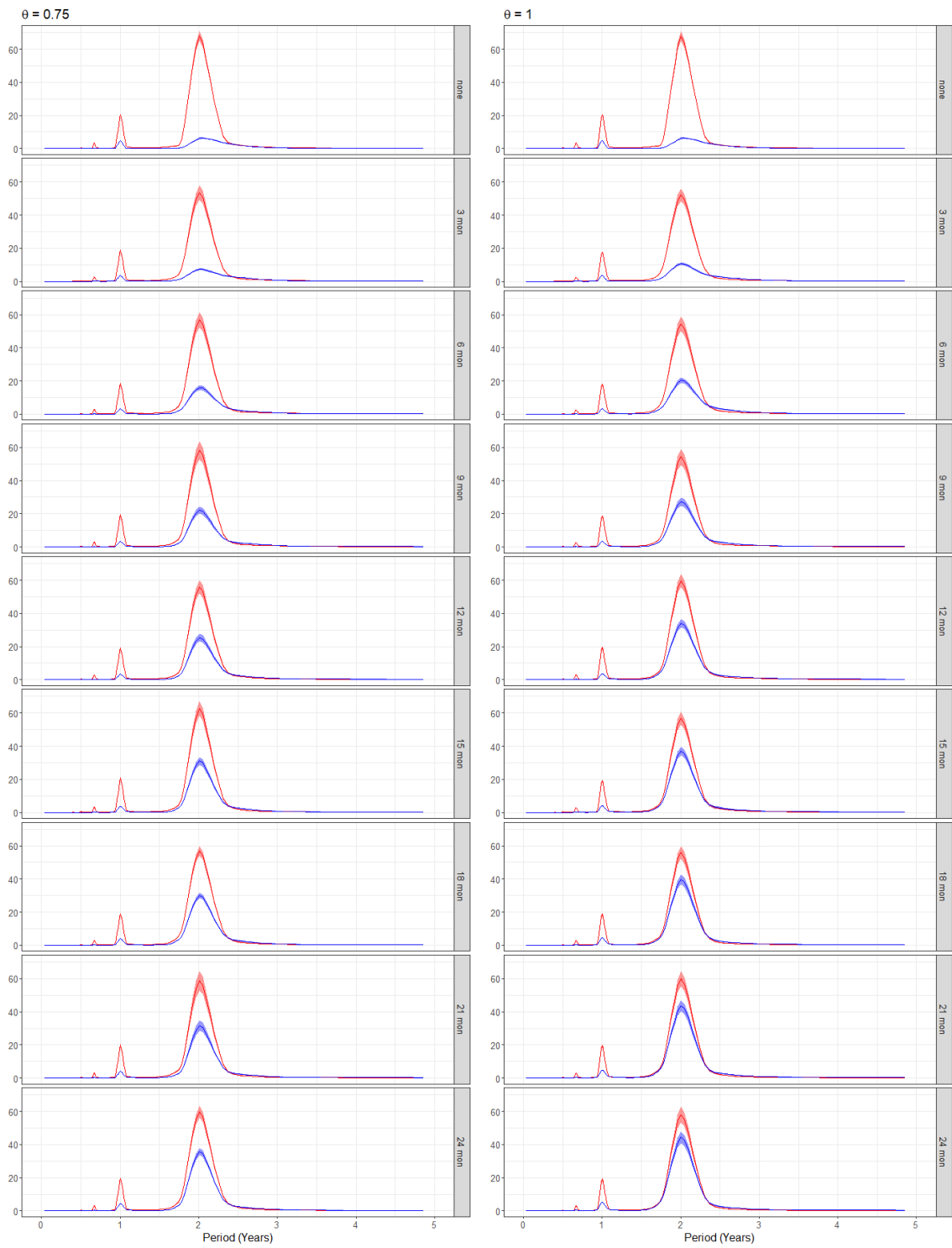
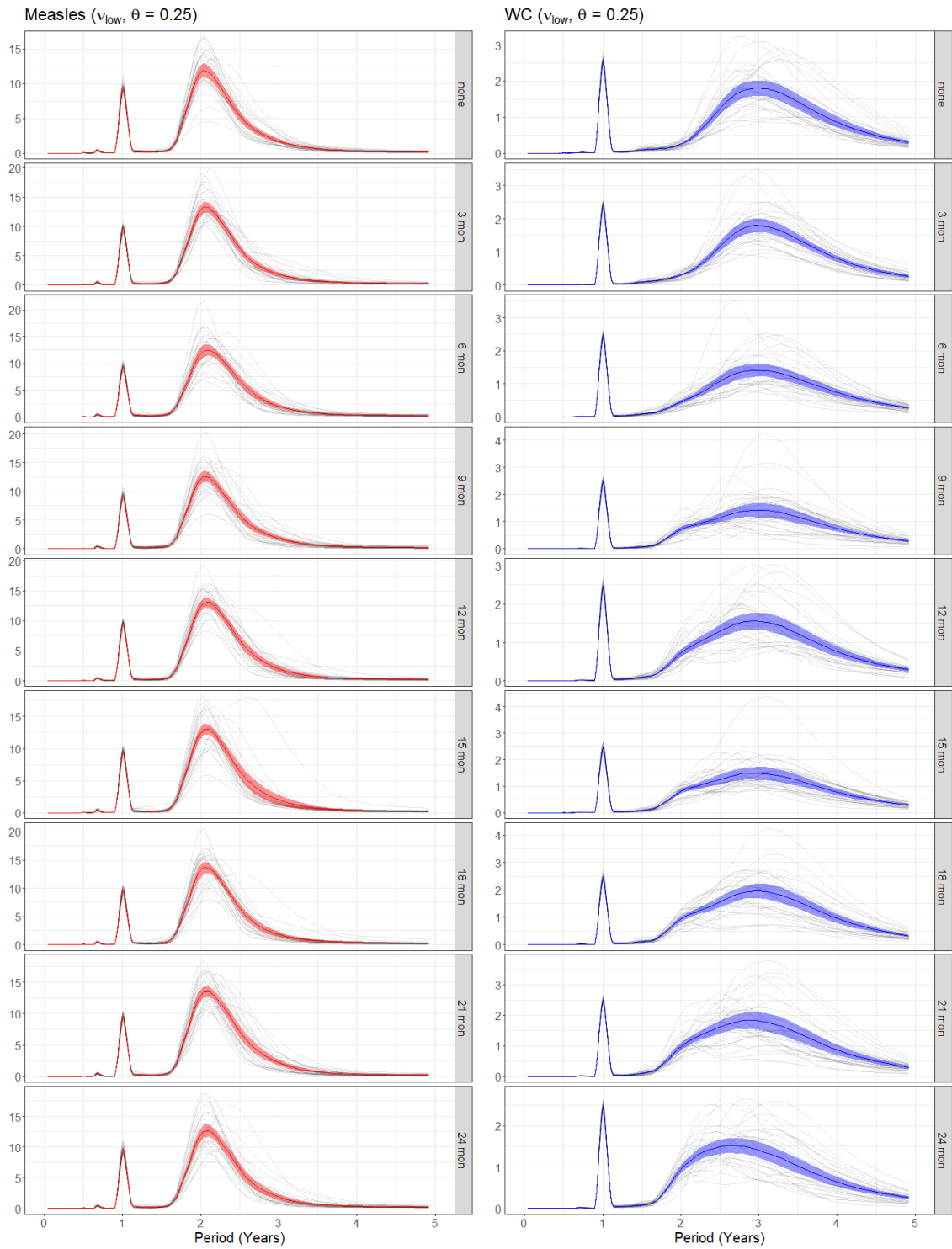
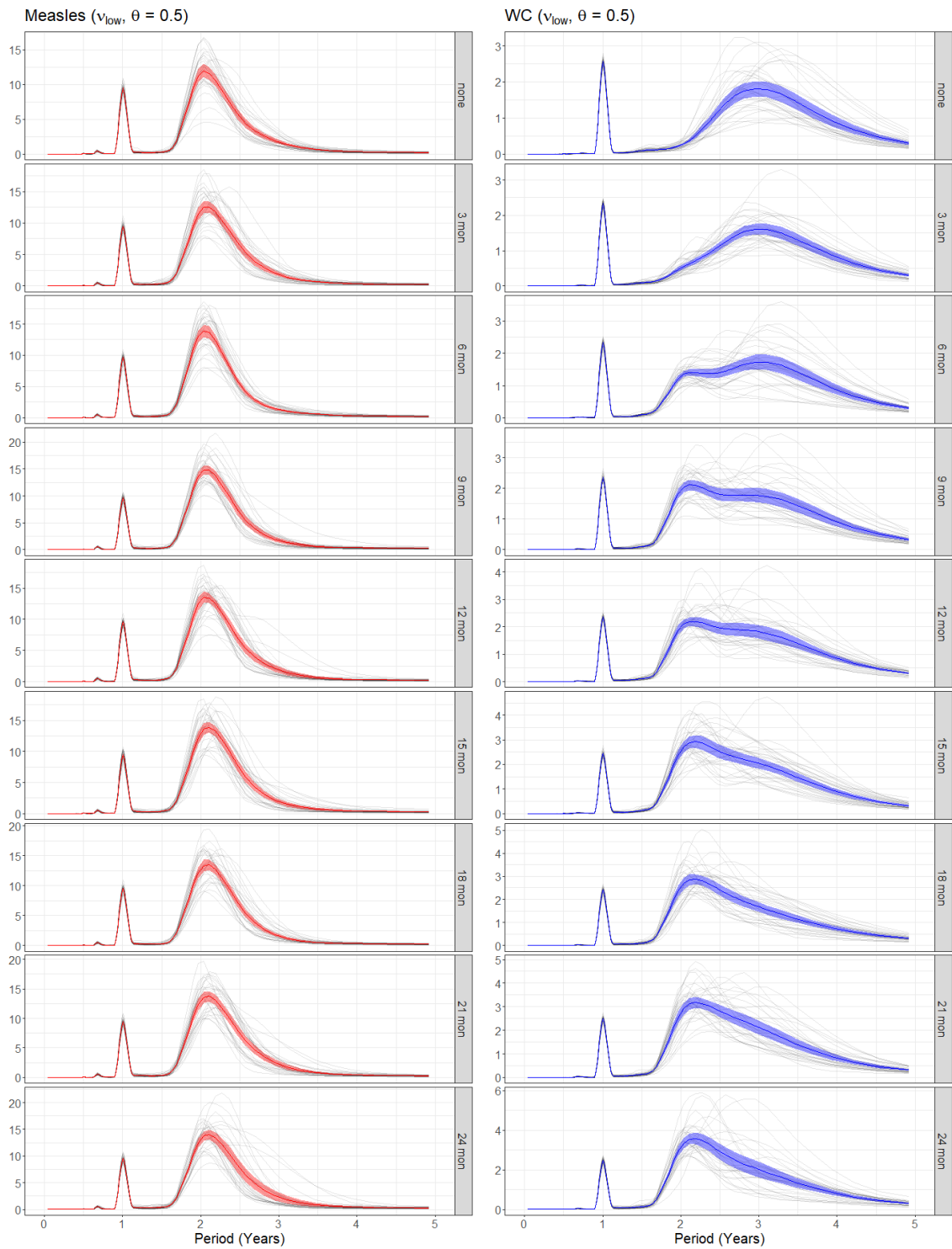
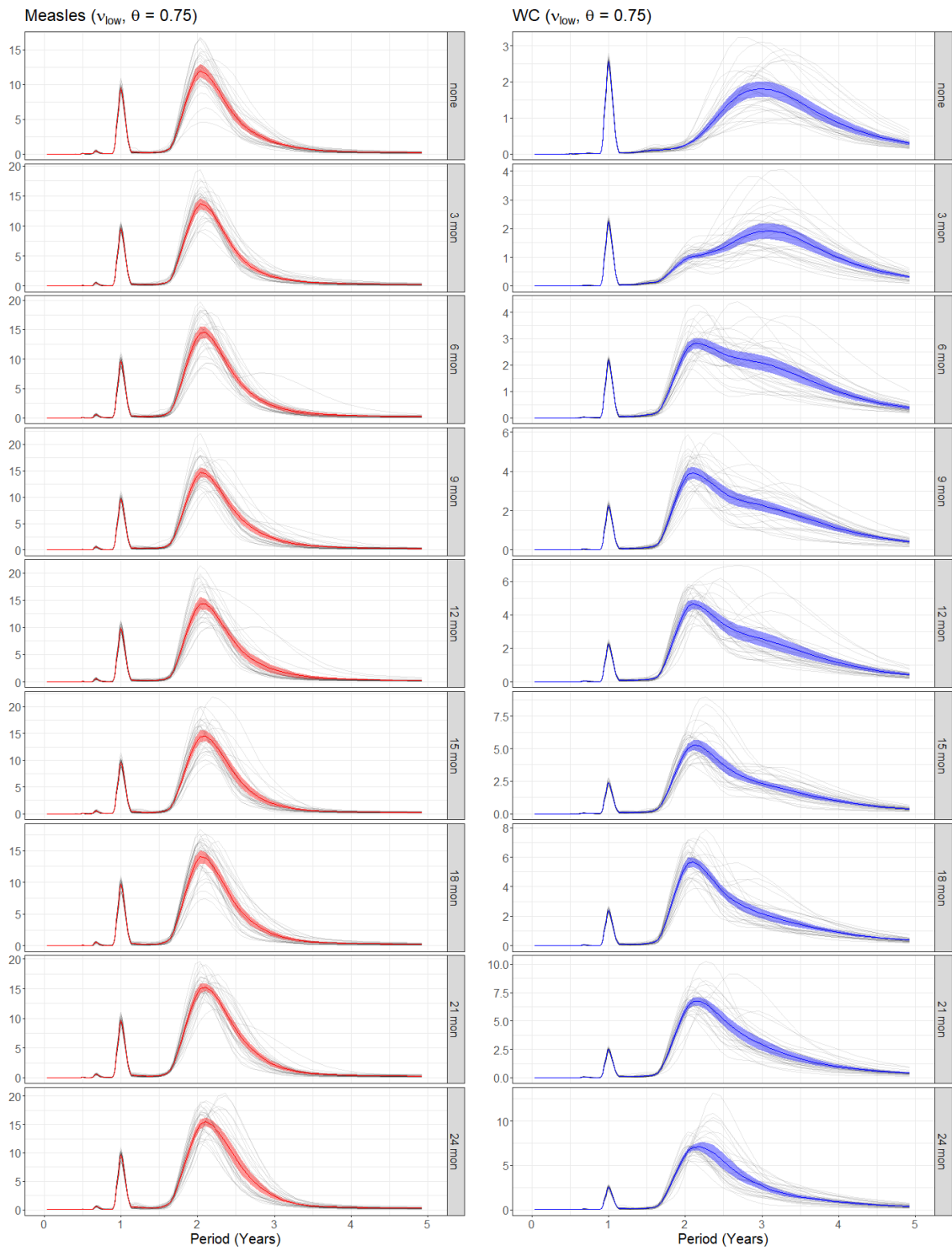


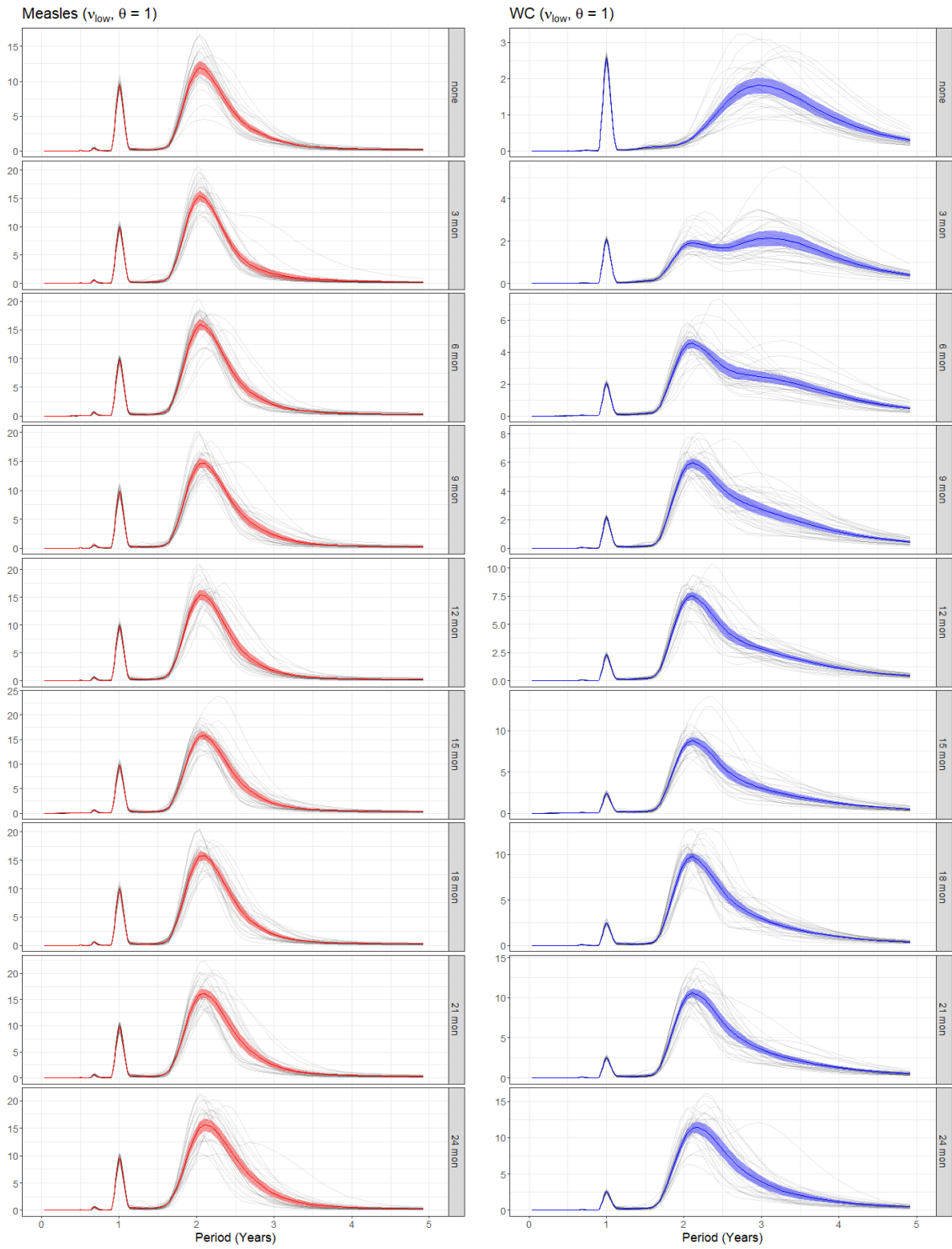
Figure 32: Periodograms of disease incidence from IA model with time-varying ν_{low} and μ corresponding to LBoM period. Time-varying parameters were calculated using London data as described in Section Section 4.1. Periodograms were computed using the square-root-transformed normalized measles (red) and WC (blue) incidence weekly series extracted from stochastic simulations. Simulations were done for $\theta = 0.25, 0.5, 0.75, 1$ with $1/\kappa$ values between 0 and 24 months. A total of 30 realizations were done for each set of parameters. Solid colored lines indicate the average periodogram and colored bands represent 95% confidence intervals

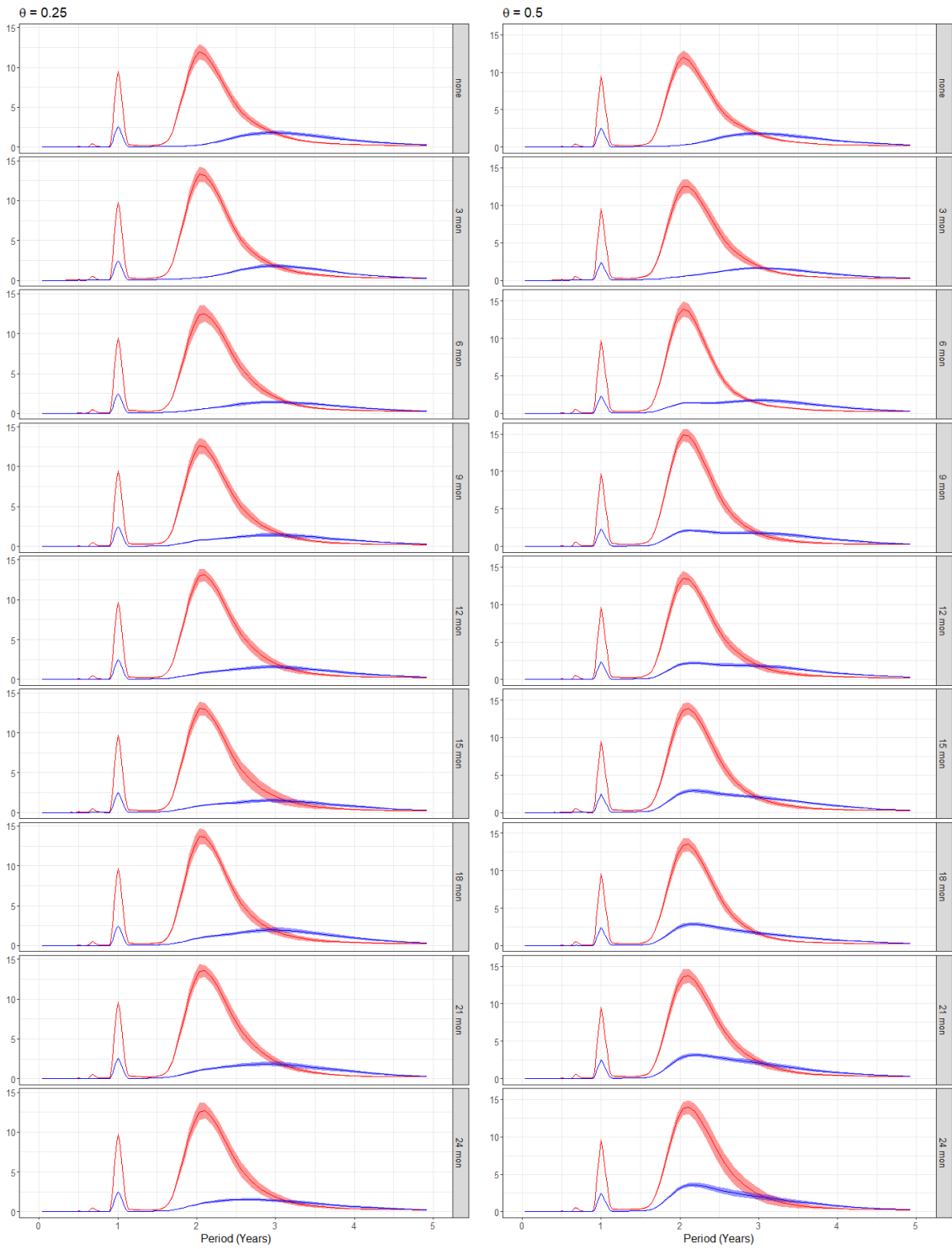
B.3.3 RGWR Period











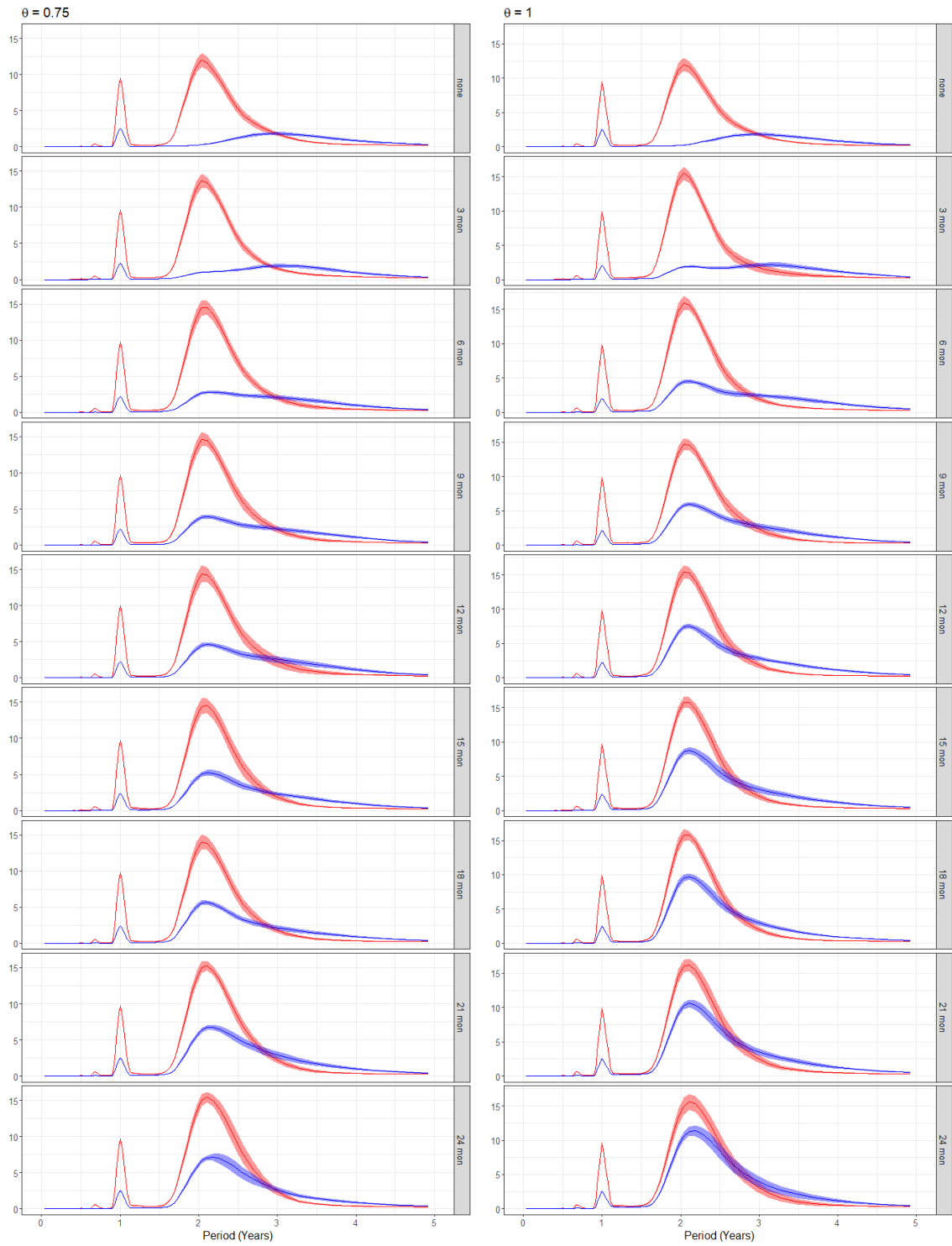
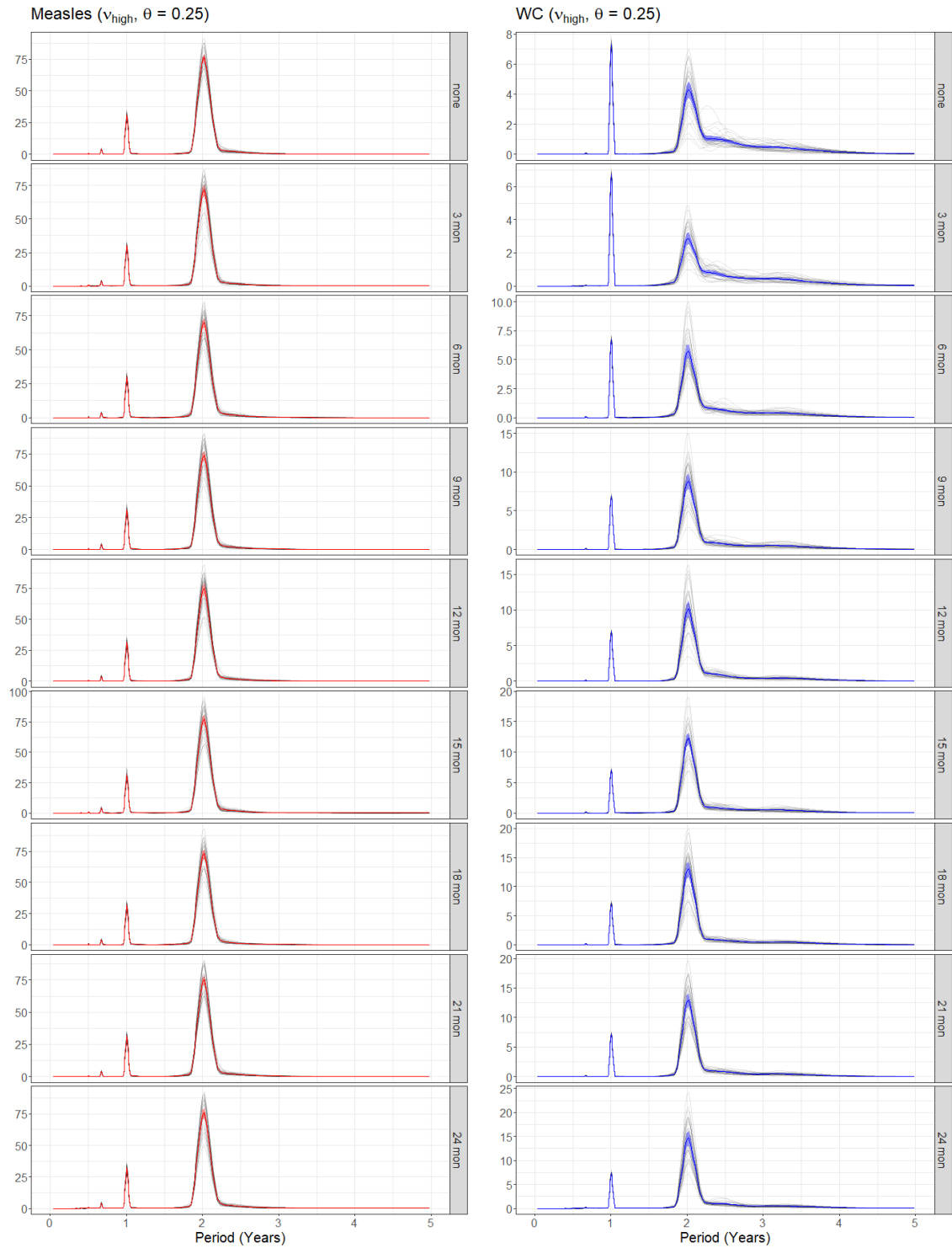
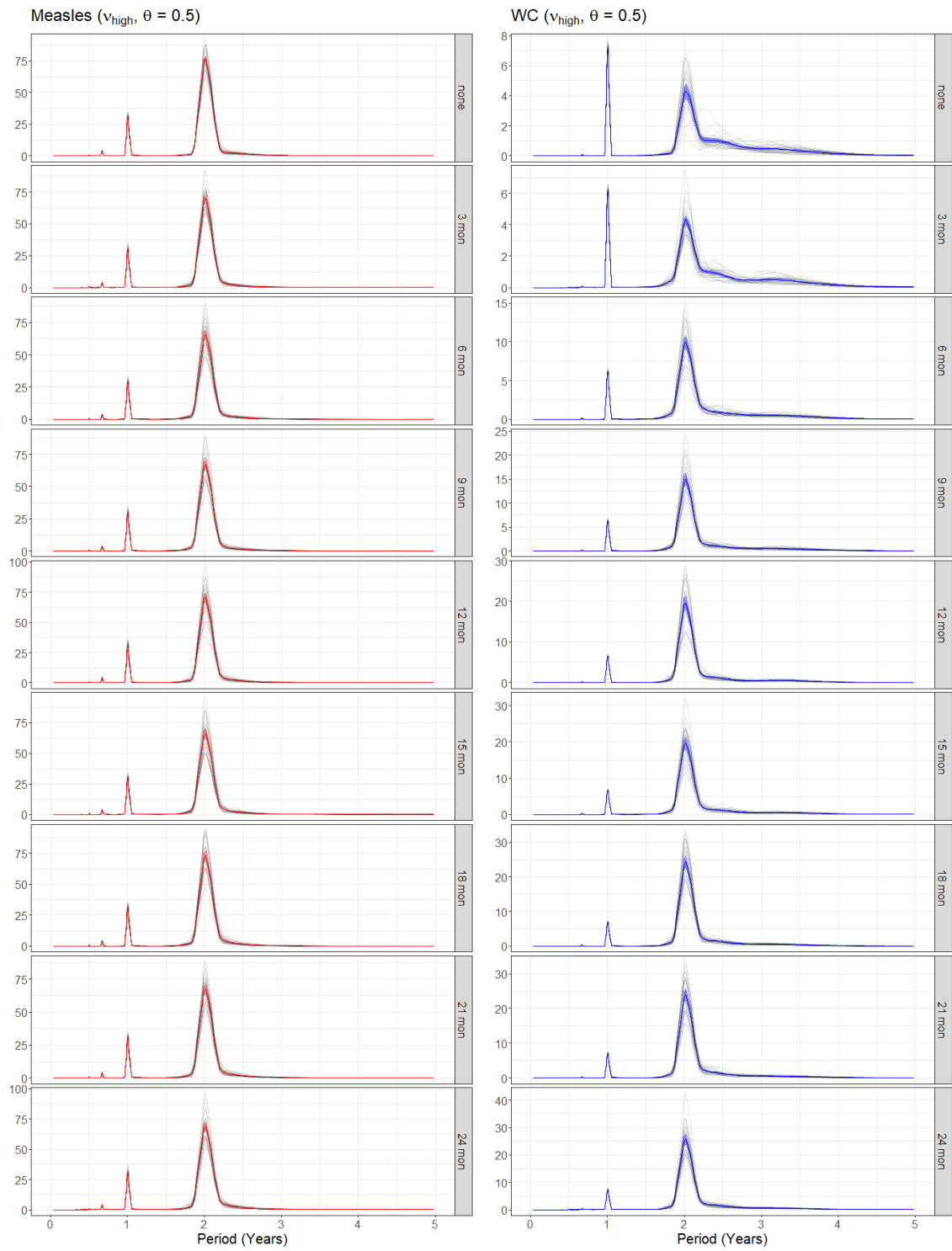


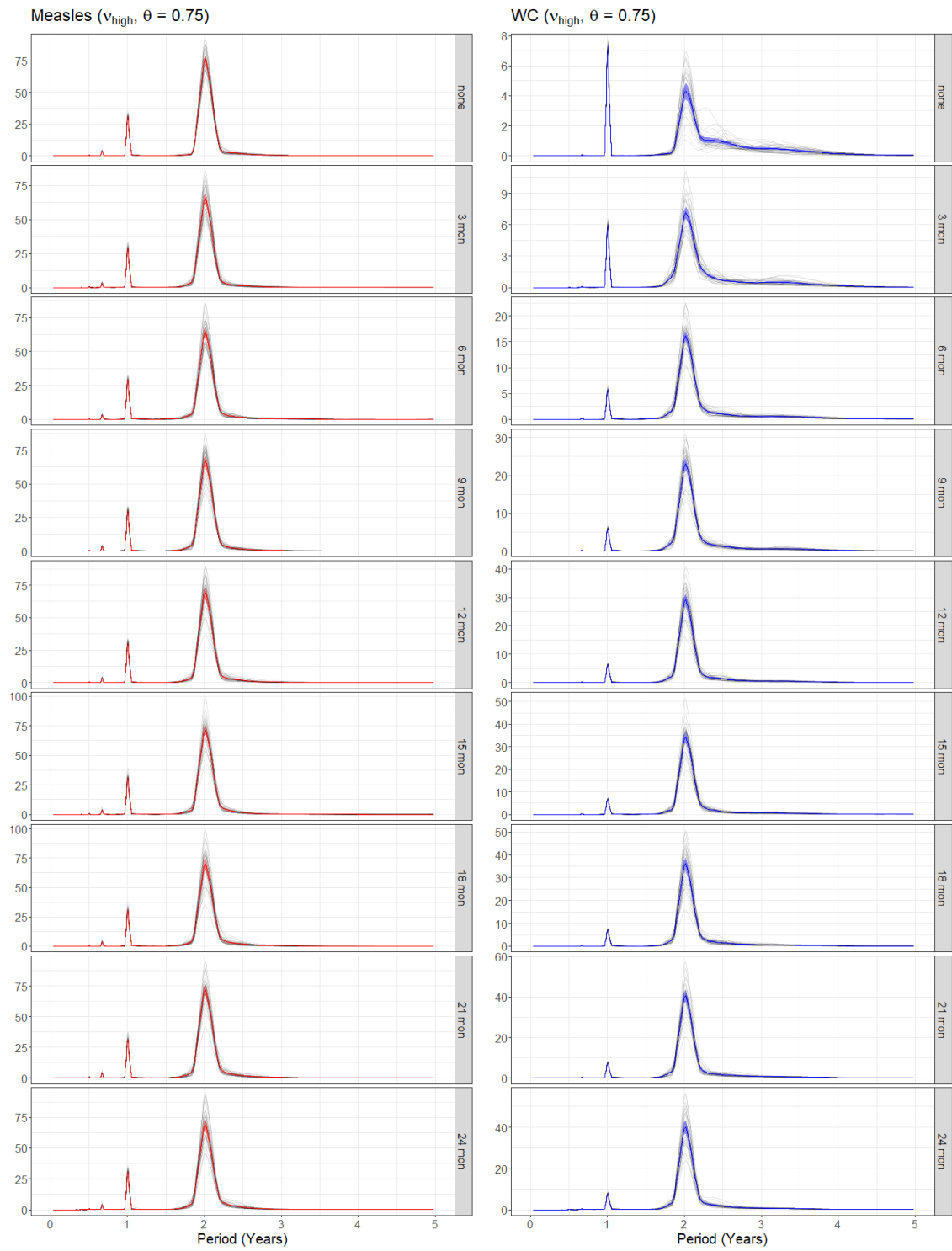
Figure 33: Periodograms of disease incidence from IA model with time-varying ν_{low} and μ corresponding to RGWR period. Time-varying parameters were calculated using London data as described in Section 4.1. Periodograms were computed using the square-root-transformed normalized measles (red) and WC (blue) incidence weekly series extracted from stochastic simulations. Simulations were done for $\theta = 0.25, 0.5, 0.75, 1$ with $1/\kappa$ values between 0 and 24 months. A total of 30 realizations were done for each set of parameters. Solid colored lines indicate the average periodogram and colored bands represent 95% confidence intervals

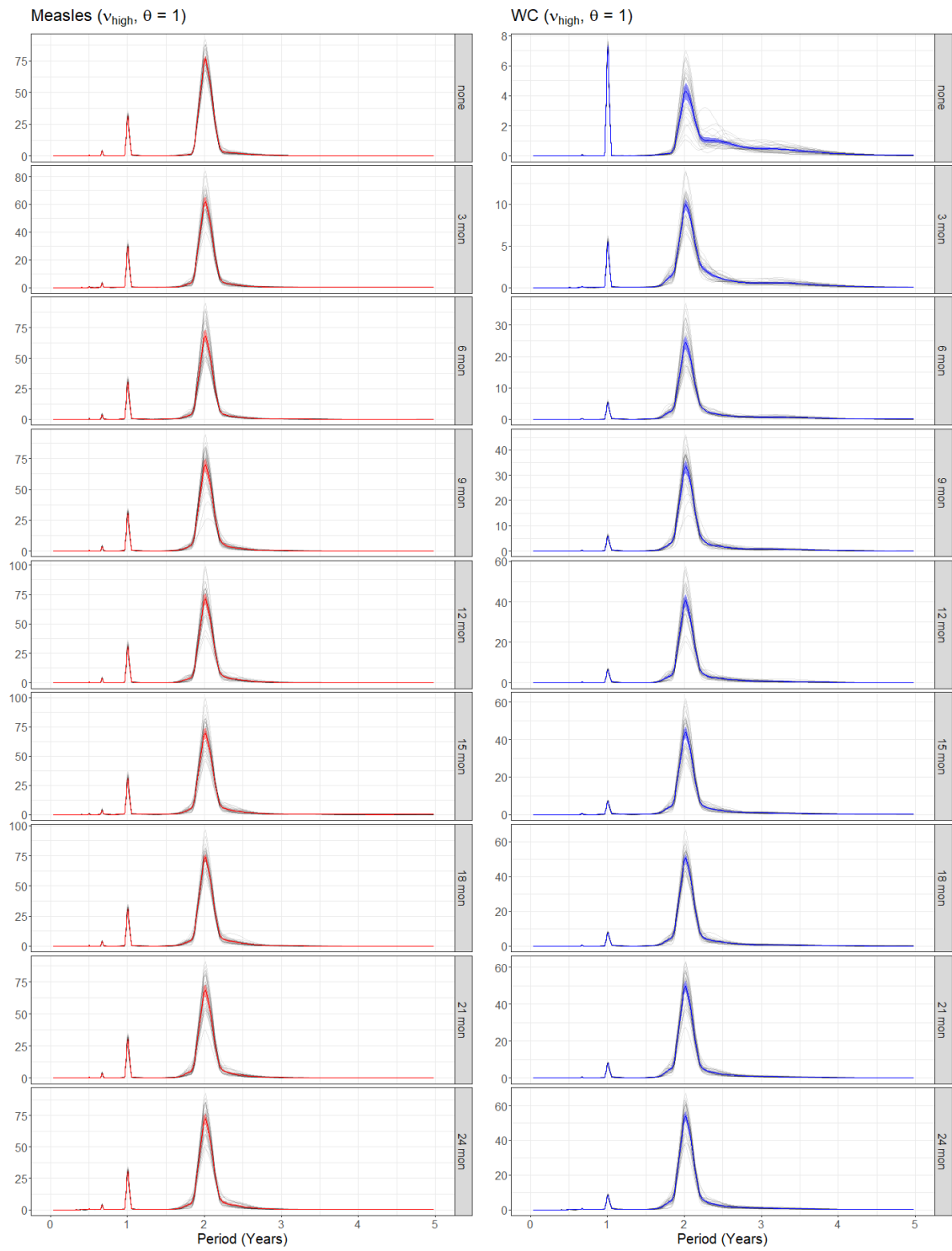
B.4 Simulations with $\nu_{\text{high}}(t)$ and $\mu(t)$

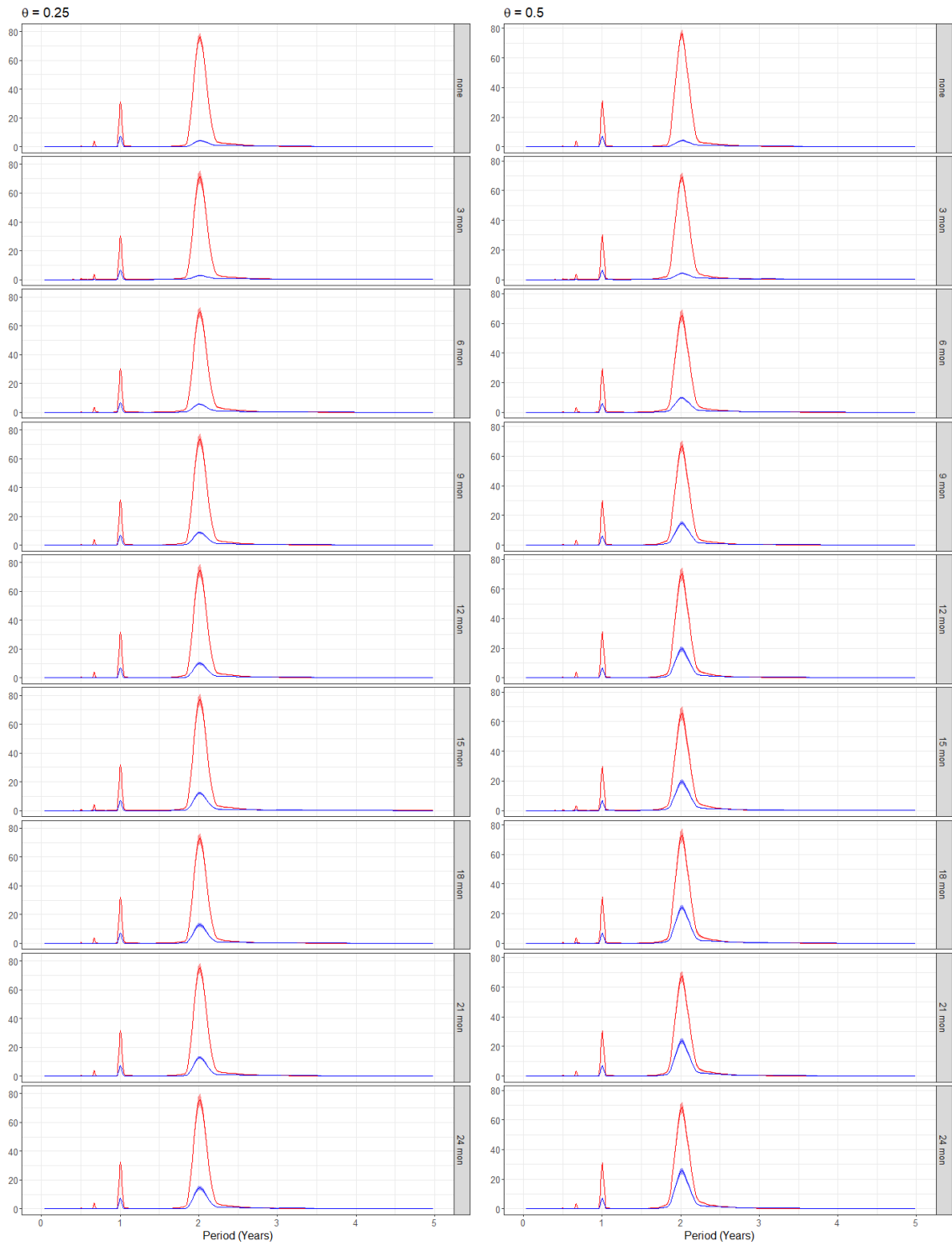
B.4.1 1750–1900











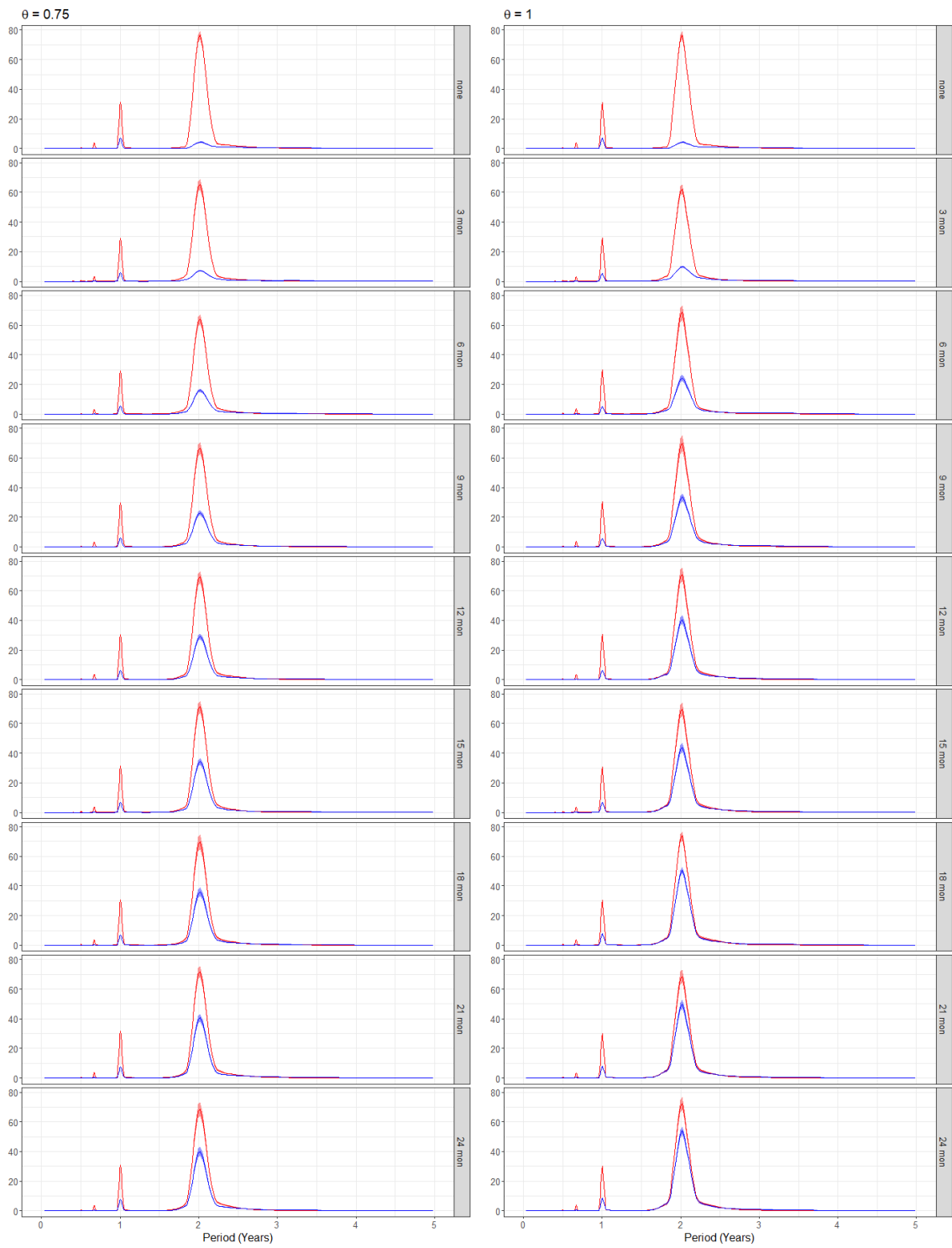
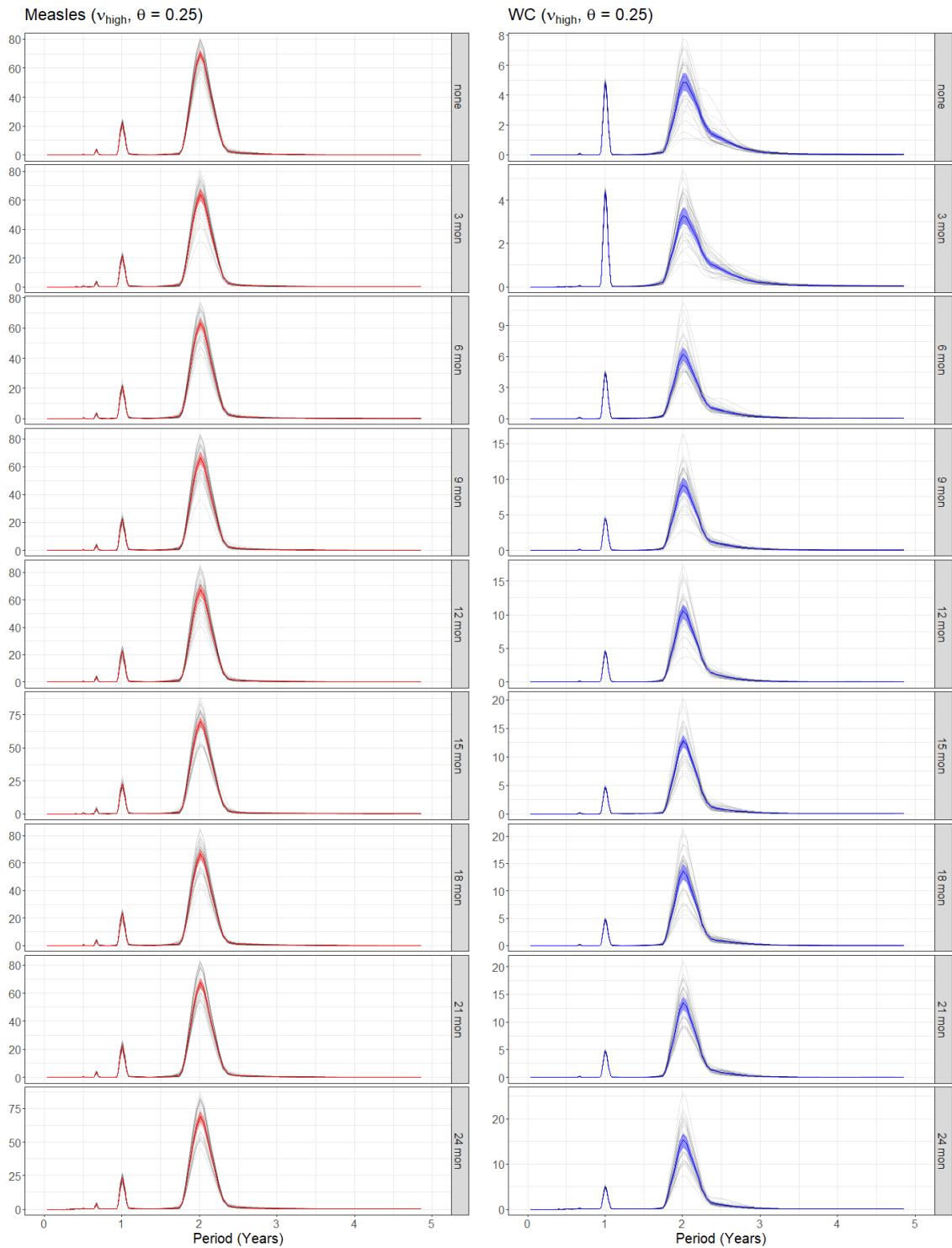
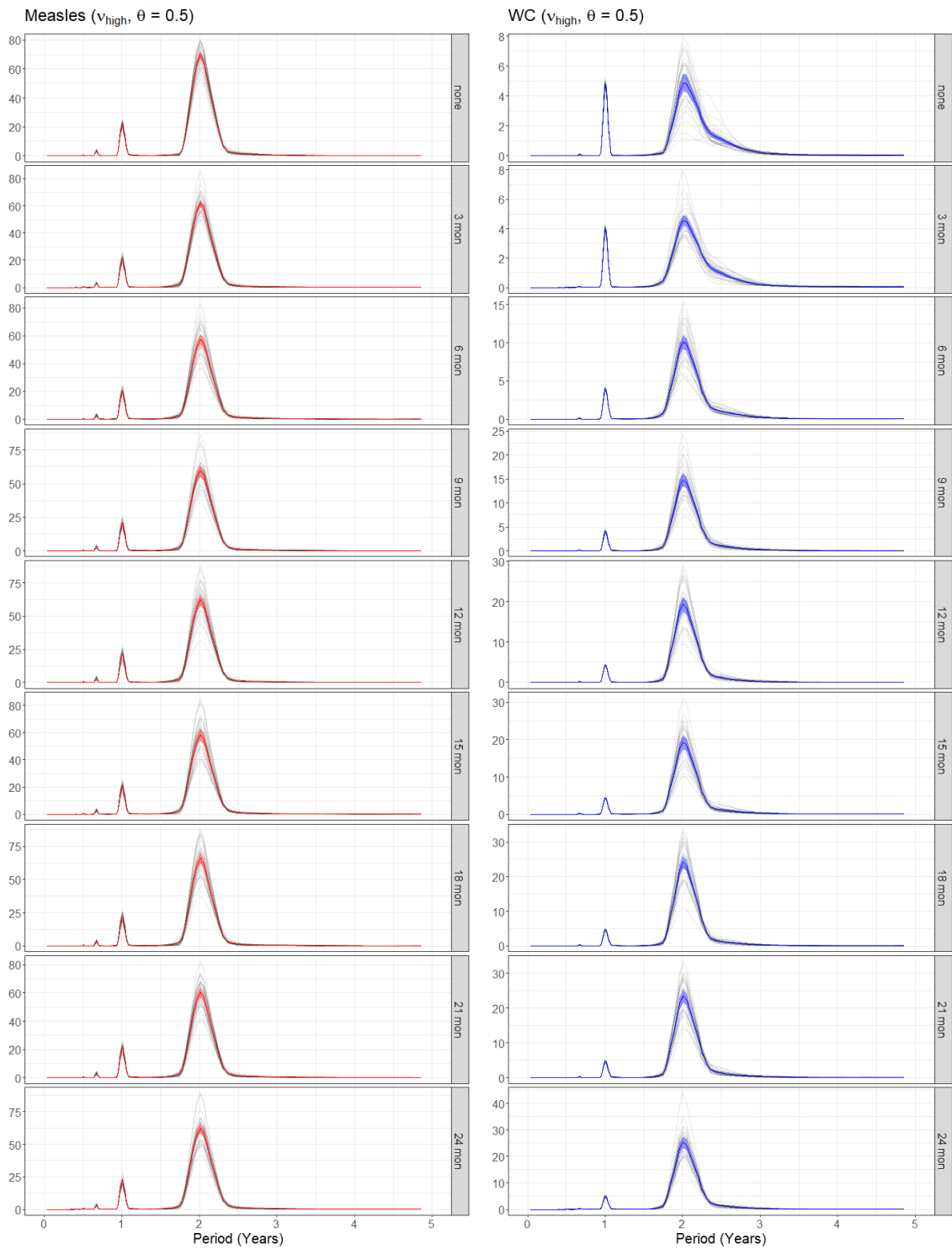
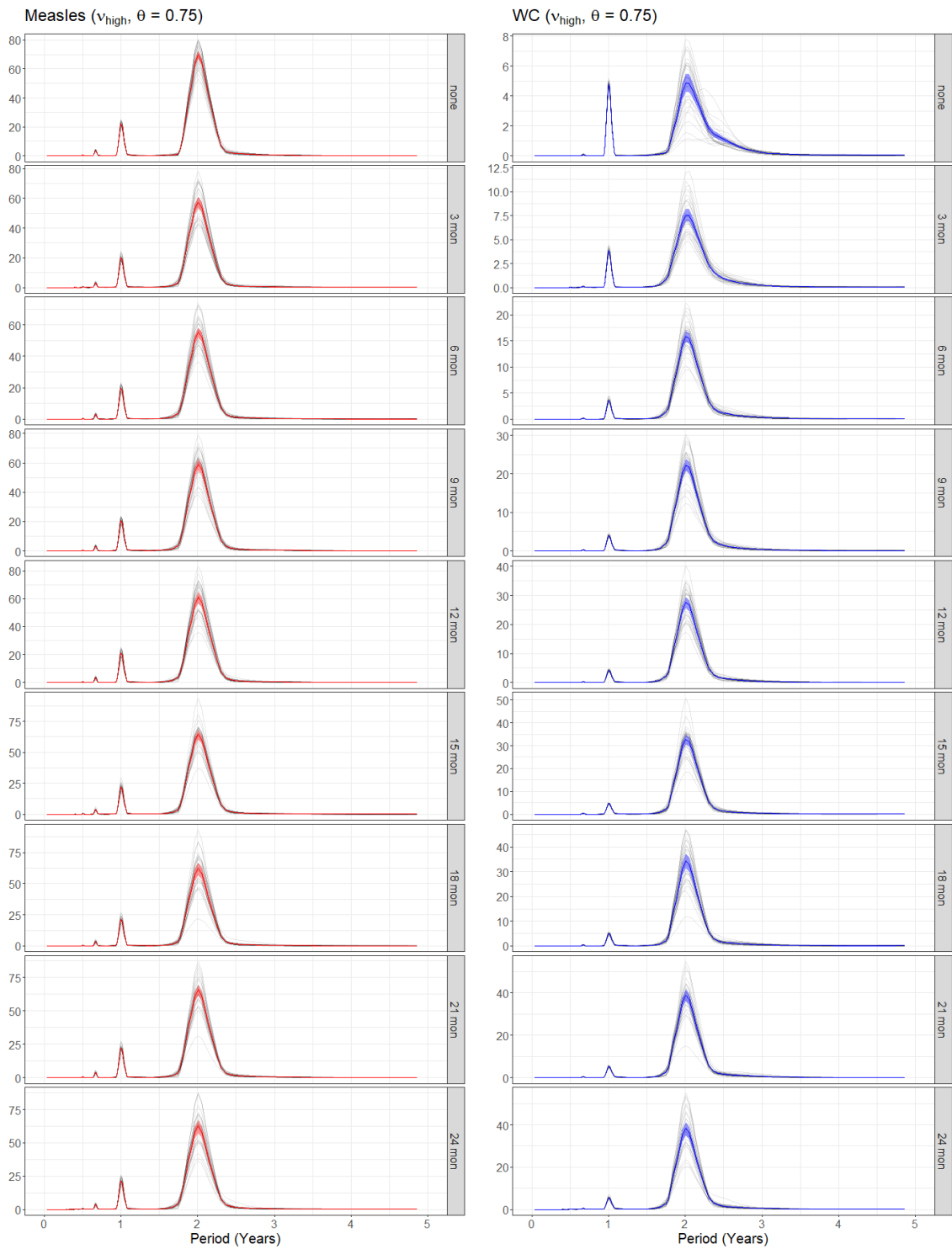


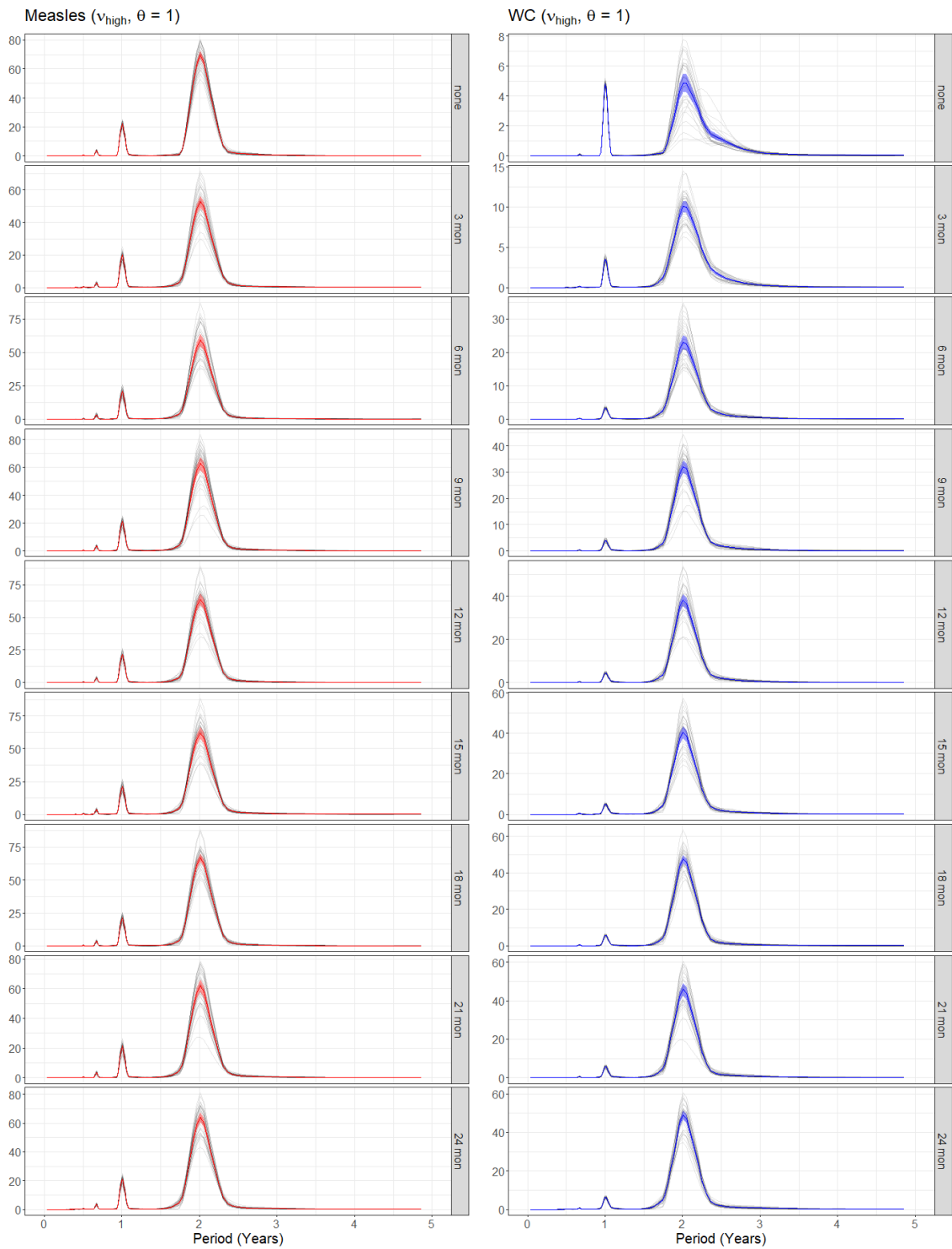
Figure 34: Periodograms of disease incidence from IA model with time-varying ν_{high} and μ . Time-varying parameters were calculated using London data between 1750 - 1900 as described in Section 4.1. Periodograms were computed using the square-root-transformed normalized measles (red) and WC (blue) incidence weekly series extracted from stochastic simulations. Simulations were done for $\theta = 0.25, 0.5, 0.75, 1$ with $1/\kappa$ values between 0 and 24 months. A total of 30 realizations were done for each set of parameters. Solid colored lines indicate the average periodogram and colored bands represent 95% confidence intervals

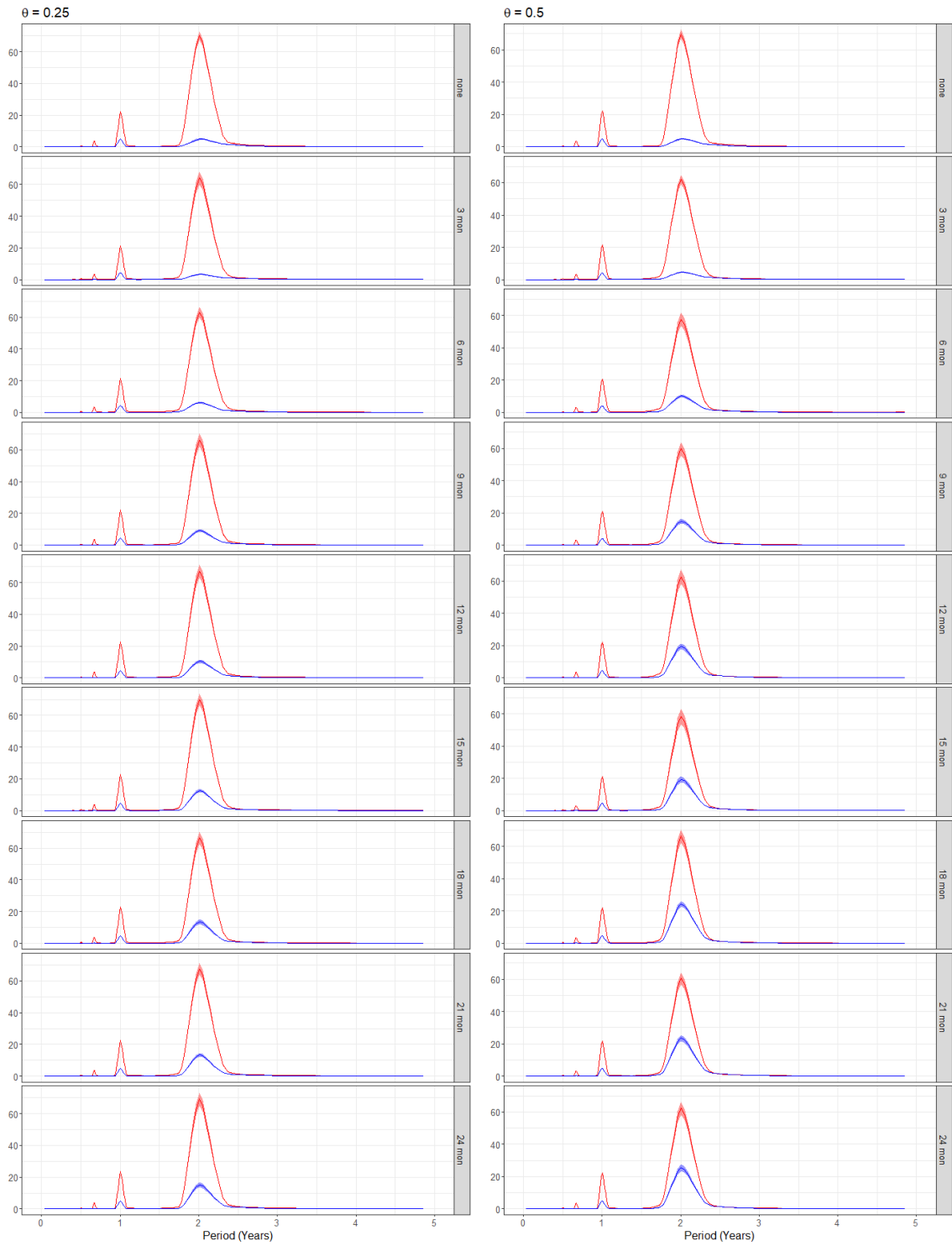
B.4.2 LBoM Period











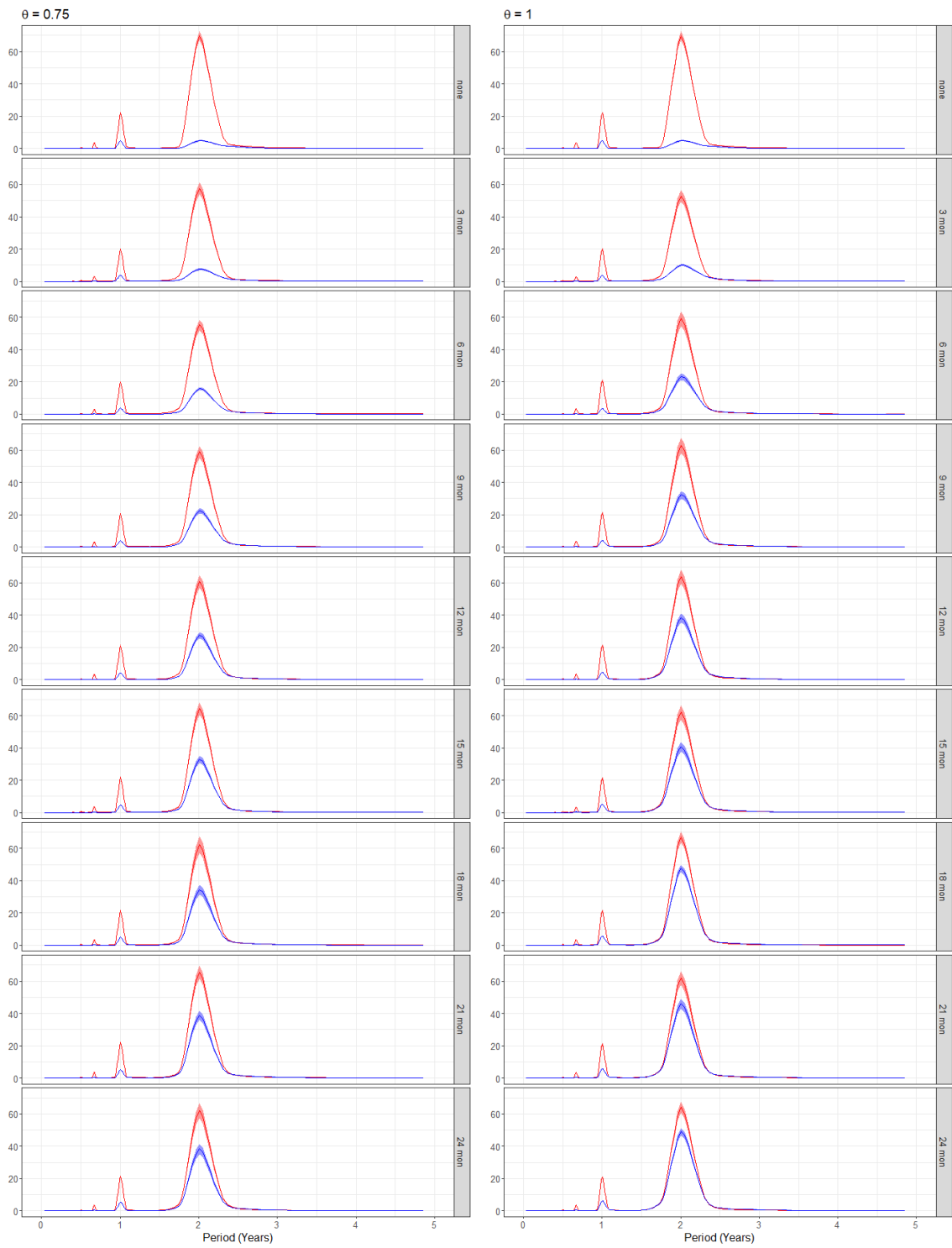
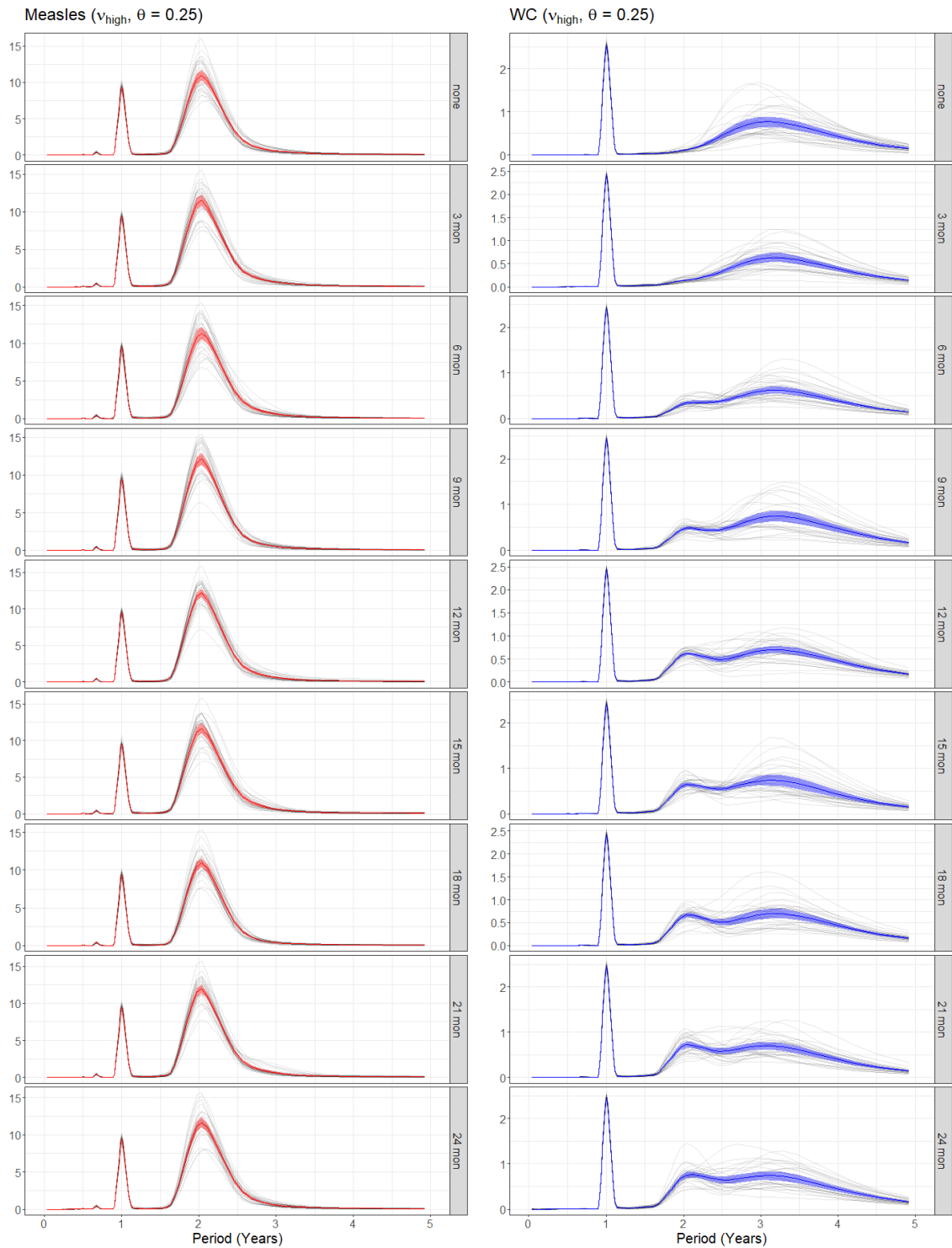
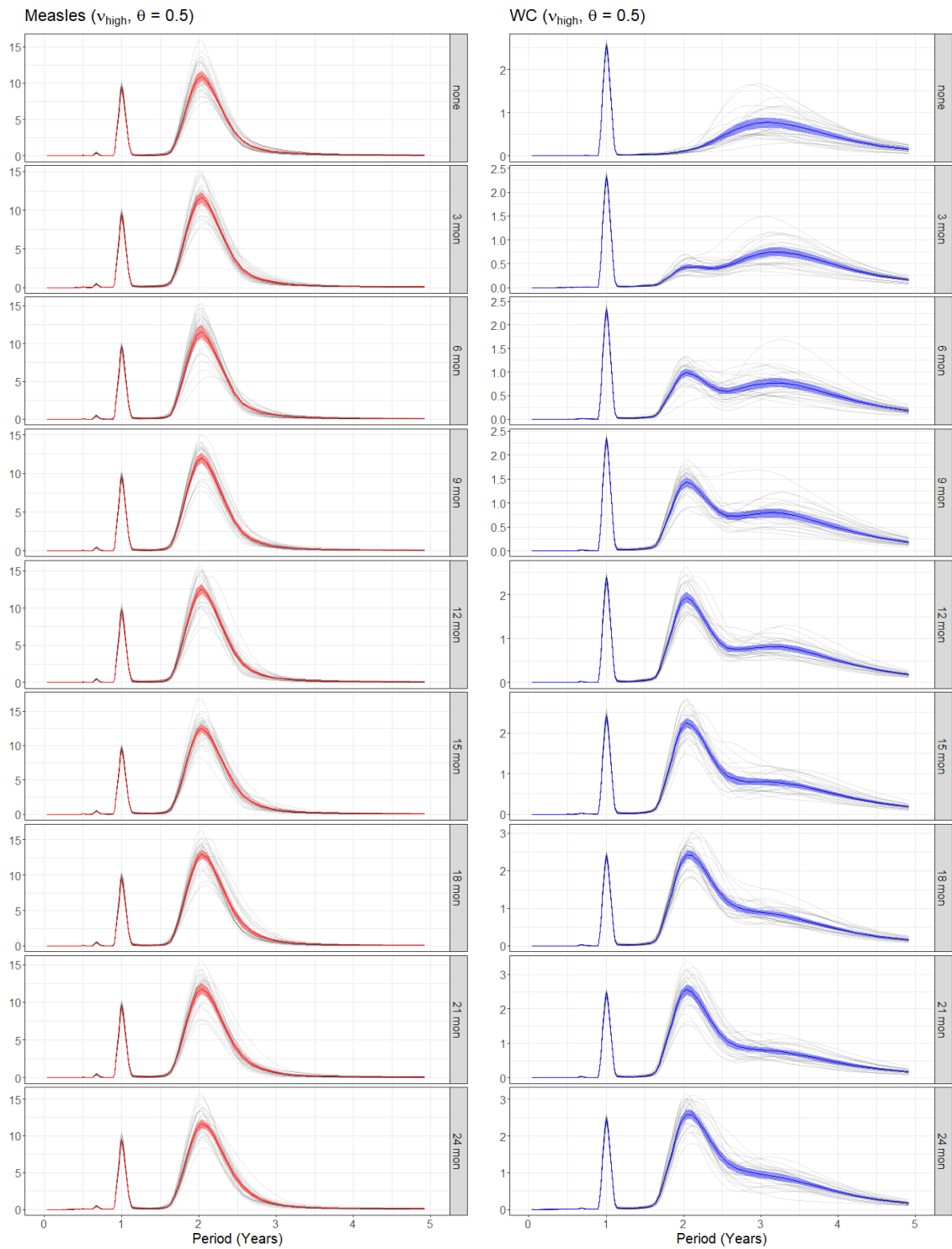
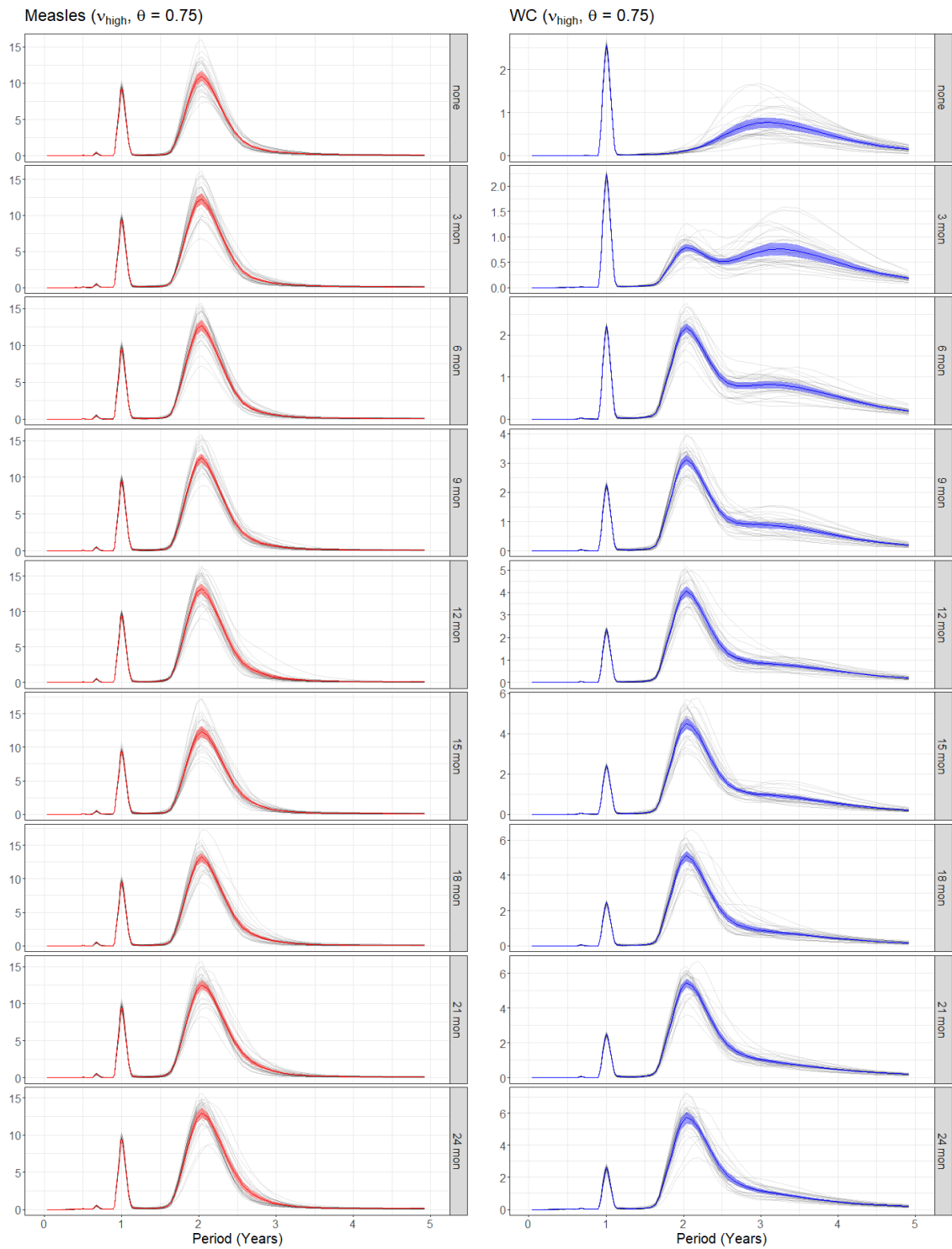


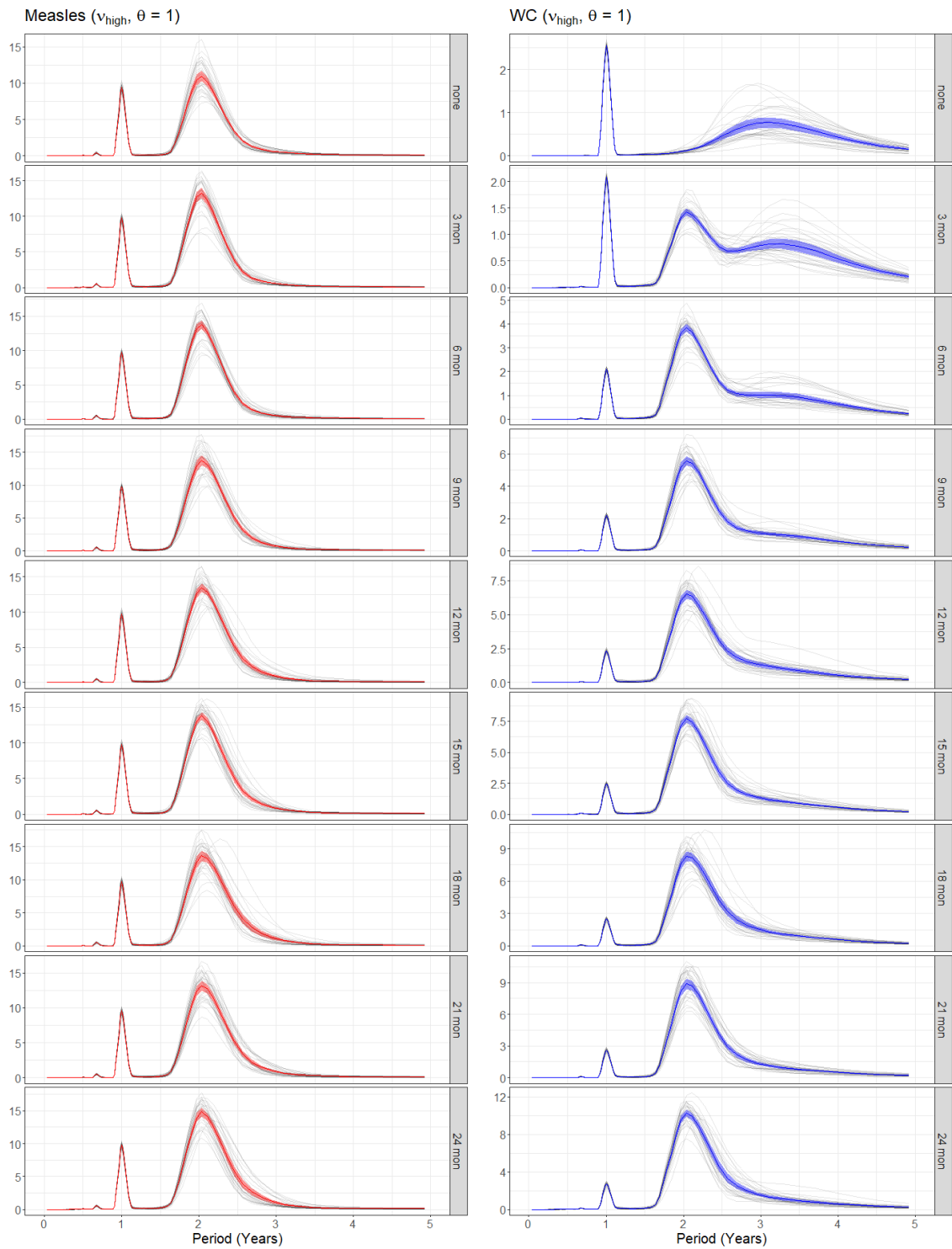
Figure 35: Periodograms of disease incidence from IA model with time-varying ν_{high} and μ corresponding to LBoM period. Time-varying parameters were calculated using London data as described in Section 4.1. Periodograms were computed using the square-root-transformed normalized measles (red) and WC (blue) incidence weekly series extracted from stochastic simulations. Simulations were done for $\theta = 0.25, 0.5, 0.75, 1$ with $1/\kappa$ values between 0 and 24 months. A total of 30 realizations were done for each set of parameters. Solid colored lines indicate the average periodogram and colored bands represent 95% confidence intervals

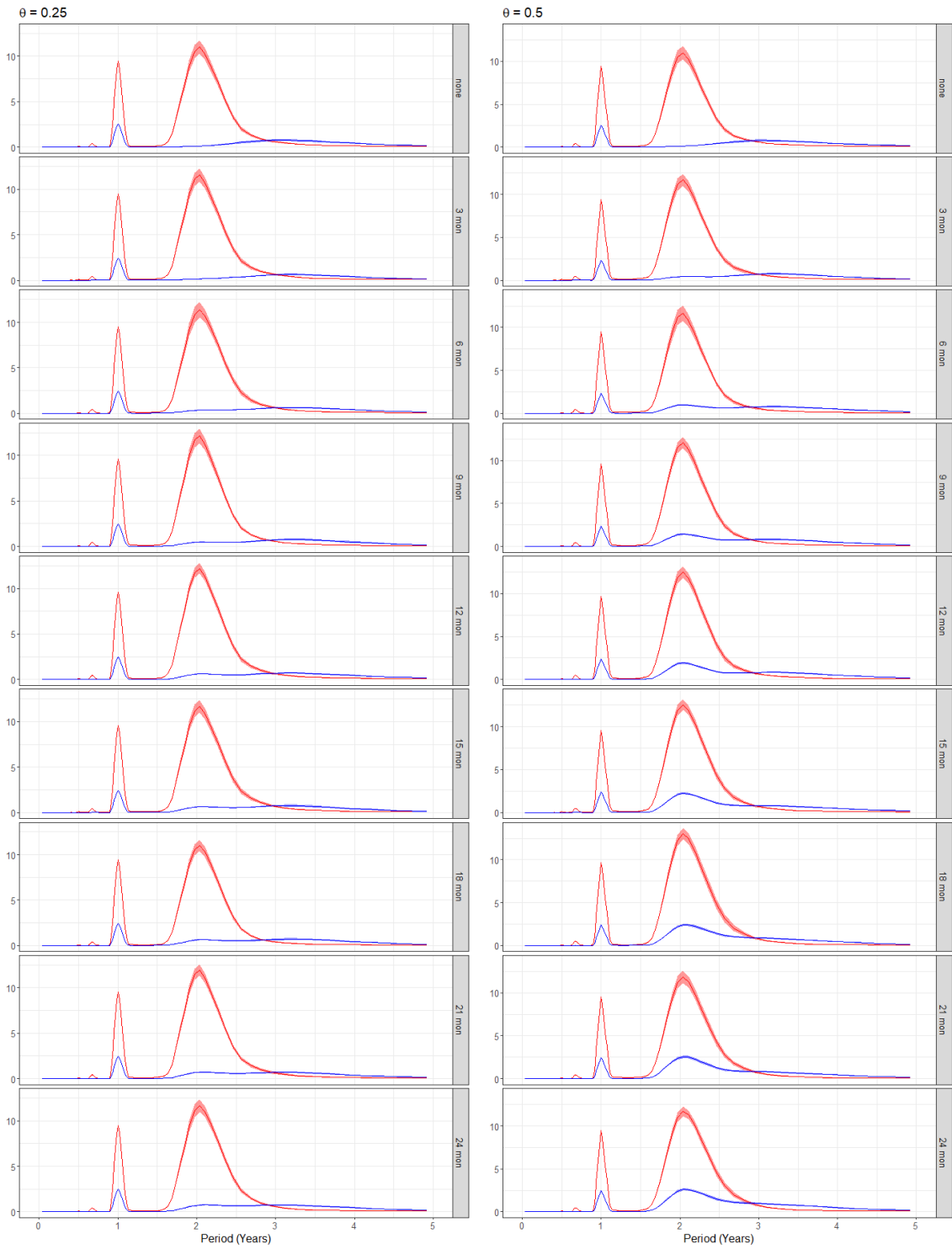
B.4.3 RGWR Period











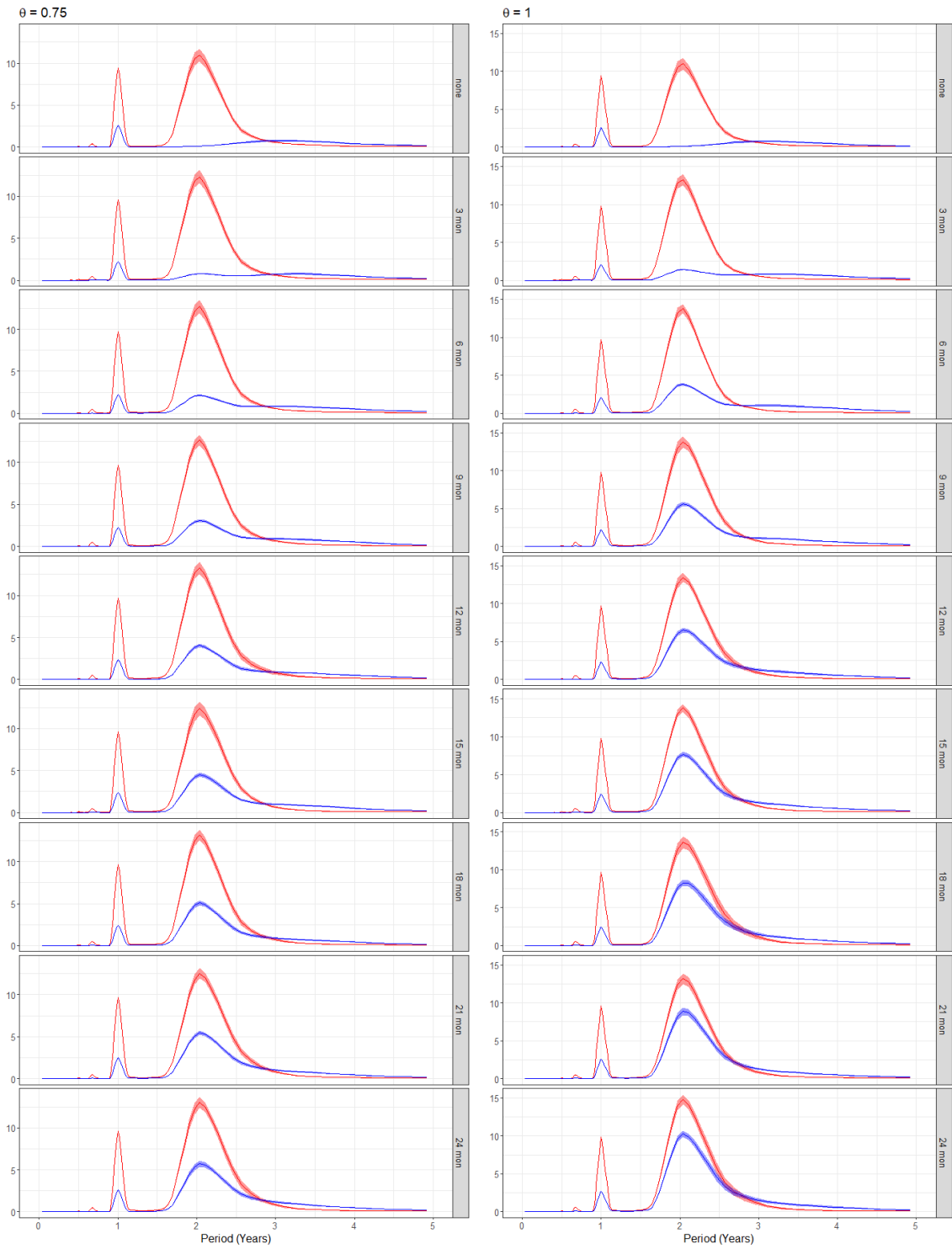


Figure 36: Periodograms of disease incidence from IA model with time-varying ν_{high} and μ corresponding to RGWR period. Time-varying parameters were calculated using London data as described in Section 4.1. Periodograms were computed using the square-root-transformed normalized measles (red) and WC (blue) incidence weekly series extracted from stochastic simulations. Simulations were done for $\theta = 0.25, 0.5, 0.75, 1$ with $1/\kappa$ values between 0 and 24 months. A total of 30 realizations were done for each set of parameters. Solid colored lines indicate the average periodogram and colored bands represent 95% confidence intervals

C Sample Codes

This section presents the basic R code used to generate the results in this thesis.

C.1 Processing & Analyzing London Mortality Data

1 The London mortality data was retrieved from the LBoM package, which was from
2 a private repository. The following code first cleans up and interpolates for missing
3 values in the time series of measles, WC, and ACM, then normalizes the disease
4 mortality time series as outlined in Section 2.3:

```
5 library(tidyverse)
6 library(lubridate)
7 library(LBoM)
8 library(zoo)
9 library(EMD)
10
11 # Process acm data normalization
12 acm_data <- get_data(category = "acm") %>%
13   select(numdate, death.all.causes) %>%
14   filter(numdate >= 1750 & numdate <= 1900) %>%
15   rename(acm = death.all.causes)
16
17 # Linear interpolation if necessary
18 v <- acm_data$acm
19 if (sum(is.na(v)) > 0){
20   v <- na.approx(v, x = acm_data$numdate)
21   v <- floor(v)
22 }
23 acm_data <- acm_data %>%
24   mutate(acm = v)
25
26 # Separate LBoM & GR (calculate trend separately)
27 acm_lbom <- acm_data %>%
28   filter(numdate < 1842)
29 acm_gr <- acm_data %>%
30   filter(numdate >= 1842)
31
32 # Calculate acm trend using EMD
33 e_lbom <- emd(acm_lbom$acm, acm_lbom$numdate, boundary = "wave")
34 e_gr <- emd(acm_gr$acm, acm_gr$numdate, boundary = "wave")
35 e <- c(e_lbom$residue, e_gr$residue)
36 acm_data <- acm_data %>%
```

```

37   mutate(residue = e)
38
39   # Retrieve wc time series from LBoM package
40   # Clean up data first
41   wc <- get_data(category = "diseaseMort", columns = "cough") %>%
42     filter(numdate >= 1750 & numdate <= 1900) %>%
43     mutate(from =
44             ymd(year.from * 10000 + month.from * 100 + day.from)) %>%
45     mutate(to = ymd(year.to * 10000 + month.to * 100 + day.to))
46   wc <- wc[!wc$to == ymd(18731129), ] # Remove repeated date
47   missing_wks <- read_csv("./17501900_missing_weeks.csv") %>%
48     mutate(from = ymd(from)) %>%
49     mutate(to = ymd(to))
50   wc <- bind_rows(wc, missing_wks) %>%
51     arrange(numdate)
52
53   # Linear interpolation
54   v1 <- wc$whooping.cough
55   v2 <- wc$schincough
56   v3 <- wc$hooping.cough
57   v <- numeric(length(v1))
58
59   for (i in 1:length(v1)) {
60     if (!is.na(v1[i]) || !is.na(v2[i]) || !is.na(v3[i])) {
61       v[i] <-
62         replace_na(v1[i], 0) + replace_na(v2[i], 0) + replace_na(v3[i], 0)
63     }
64     else{
65       v[i] <- NA
66     }
67   }
68
69   if (sum(is.na(v)) > 0) {
70     v <- na.approx(v, x = wc$numdate)
71     v <- floor(v)
72   }
73
74   # Interpolate acm trend at listed dates if needed
75   wc_lbom_date <- wc$numdate[wc$numdate < 1842]
76   wc_gr_date <- wc$numdate[wc$numdate >= 1842]
77   emd_lbom_inter <- approx(x = acm_lbom$numdate,
78                            y = e_lbom$residue, xout = wc_lbom_date)

```

```

79 emd_gr_inter <- approx(x = acm_gr$numdate,
80                       y = e_gr$residue, xout = wc_gr_date)
81 emd_inter <- bind_rows(emd_lbom_inter, emd_gr_inter) %>%
82   mutate(y = replace_na(y,
83                       emd_lbom_inter$y[length(emd_lbom_inter$y) - 1]))
84
85 # Calculate normalized and sqrt normalized data
86 wc <- wc %>%
87   select(c("from", "to", "numdate")) %>%
88   mutate(wc.deaths = v) %>%
89   mutate(acm = emd_inter$y) %>%
90   mutate(wc.norm = wc.deaths/acm) %>%
91   mutate(wc.sqrt.norm = sqrt(wc.norm))
92
93 # Retrieve measles time series from LBoM package
94 # Clean up data
95 m <- get_data(category = "diseaseMort", columns = "meas") %>%
96   filter(numdate >= 1750 & numdate <= 1900) %>%
97   mutate(from =
98           ymd(year.from * 10000 + month.from * 100 + day.from)) %>%
99   mutate(to = ymd(year.to * 10000 + month.to * 100 + day.to))
100 m <- m[!m$to == ymd(18731129), ]
101 m <- bind_rows(m, missing_wks) %>%
102   arrange(numdate)
103
104 # Linear interpolation
105 v <- m$measles
106 if (sum(is.na(v)) > 0) {
107   v <- na.approx(v, x = m$numdate)
108   v <- floor(v)
109 }
110
111 # Calculate normalized and sqrt normalized data
112 m <- m %>%
113   select(c("from", "to", "numdate")) %>%
114   mutate(m.deaths = v) %>%
115   mutate(acm = emd_inter$y) %>%
116   mutate(m.norm = m.deaths/acm) %>%
117   mutate(m.sqrt.norm = sqrt(m.norm))

```

The normalized data was then used to perform the spectral analysis done in Sec-

tion 2.4. The code for spectral analysis of the measles data is presented, but could be modified to perform analysis on WC or simulation data.

```
118
119 tion 2.4. The code for spectral analysis of the measles data is presented, but could be
120 modified to perform analysis on WC or simulation data.
121 library(tidyverse)
122 library(WaveletComp)
123
124 # Periodogram
125 # Retrieve sqrt normalized data from previous code
126 m_data <- m$m.sqrt.norm
127
128 # Calculate periodogram
129 m_pgram <- spec.pgram(m_data, log="no", plot = FALSE, taper = 0,
130                       kernel = kernel("modified.daniell",c(3,3))) %>%
131   mutate(per = 1/(52*freq)) %>%
132   select(per, spec)
133
134 # Plot periodogram
135 m_pgram_plt <- ggplot(m_pgram, aes(x = per, y = spec)) +
136   geom_line() +
137   scale_x_continuous(limits = c(0, 7), breaks = seq(0, 7, by = 1)) +
138   scale_y_continuous(limits = c(0, NA)) +
139   labs(x = "Period", y = "")
140
141 # Wavelet Spectra
142 m_data <- m %>%
143   select(from, m.sqrt.norm) %>%
144   mutate(date = as.Date(from))
145
146 # Calculate wavelet spectra
147 m_wav <- analyze.wavelet(data.frame(date = m.data$date,
148                                     cases = m.data$m.sqrt.norm),
149                           "cases", loess.span = 0.0,
150                             dt = 1/52, dj = 1/200, lowerPeriod = 0.5,
151                             upperPeriod = 8, n.sim = 1000)
152
153 # Plot wavelet spectra
154 wt.image(m_wav,
155           plot.coi = TRUE,
156           n.levels = 250,
157           siglvl = 0.05,
158           show.date = TRUE,
159           timelab = "Year",
160           periodlab = "Period (Years)",
```

```
161     main = "Measles")
```

C.2 Base Code for Stochastic Simulation of IA Model

162 The following base code was used to perform stochastic simulations of the IA model
 163 using parameters from Table 1. This code was slightly modified to perform simulations
 164 of other parameter combinations analyzed in this thesis.

```
165 library("tidyverse")
166 library("adaptivetau")
167
168 # Define realizations
169 realizations = 30
170
171 # Create data frame of IA parameters
172 IA_str = c(0.25, 0.5, 0.75, 1)
173 IA_str_fn = c("025", "05", "075", "1")
174 IA_len = c(30, 90, 180, 270, 365, 455, 545, 635, 730, 1095, 1825)
175 IA_len_fn = c("_1mon", "_3mon", "_6mon", "_9mon", "_12mon", "_15mon",
176              "_18mon", "_21mon", "_24mon", "_36mon", "_60mon")
177
178 IA_df <- as.data.frame(expand.grid(IA_len, IA_str)) %>%
179   mutate(Var1 = 365/Var1)
180 IA_df <- rbind(c(0, 0), IA_df)
181 IA_fn_df <- as.data.frame(expand.grid(IA_len_fn, IA_str_fn)) %>%
182   mutate(Var1 = as.character(Var1)) %>%
183   mutate(Var2 = as.character(Var2))
184 IA_fn_df <- rbind(c("", "0"), IA_fn_df)
185
186 # Measles Parameters
187 T_lat.m = 8/365
188 T_inf.m = 5/365
189 R0.m = 17
190 beta.m = R0.m * ((lat.m + mu.m)/lat.m) * (inf.m + mu.m)
191 alp.m = 0.1
192
193 # wc Parameters
194 T_lat.w = 8/365
195 T_inf.w = 14/365
196 R0.w = 17
197 beta.w = R0.w * ((lat.w + mu.w)/lat.w) * (inf.w + mu.w)
198 alp.w = 0.1
```

```

199
200 # Birth, death, and immigration rate
201 b_rate = 0.02
202 d_rate = 0.02
203 imm.IS = 0.00005
204 imm.IR = 0.00005
205 imm.SI = 0.00005
206 imm.RI = 0.00005
207
208 # Initial conditions for sim
209 N_0 = 800000
210 e = 130
211 q = round(1/RO.m*N_0)
212
213 init.values = c(
214     SS = q,
215     ES = e,
216     IS = e,
217     RS = e,
218     RE = e,
219     RI = e,
220     SE = e,
221     SI = e,
222     SR = e,
223     ER = e,
224     IR = e,
225     A = 0,
226     RR = N_0 - q - 10*e,
227     N = N_0,
228     Cm = 0, # Accumulator components
229     Cw = 0
230 )
231
232 # State transitions
233 transitions = list(c(SS = +1, N = +1),
234                  c(SS = -1, ES = +1),
235                  c(ES = -1, IS = +1, Cm = +1),
236                  c(IS = -1, RS = +1),
237                  c(RS = -1, RE = +1),
238                  c(RE = -1, RI = +1, Cw = +1),
239                  c(RI = -1, RR = +1),
240                  c(SS = -1, SE = +1),

```

```

241         c(SE = -1, SI = +1, Cw = +1),
242         c(SI = -1, SR = +1),
243         c(SR = -1, ER = +1),
244         c(ER = -1, IR = +1, Cm = +1),
245         c(IR = -1, A = +1),
246         c(IR = -1, RR = +1),
247         c(A = -1, RE = +1),
248         c(A = -1, RR = +1),
249         c(SS = -1, N = -1),
250         c(ES = -1, N = -1),
251         c(IS = -1, N = -1),
252         c(RS = -1, N = -1),
253         c(RE = -1, N = -1),
254         c(RI = -1, N = -1),
255         c(SE = -1, N = -1),
256         c(SI = -1, N = -1),
257         c(SR = -1, N = -1),
258         c(ER = -1, N = -1),
259         c(IR = -1, N = -1),
260         c(RR = -1, N = -1),
261         c(A = -1, N = -1),
262         c(IS = +1, N = +1),
263         c(IR = +1, N = +1),
264         c(SI = +1, N = +1),
265         c(RI = +1, N = +1)
266     )
267
268     # Rates
269     lvrates <- function(x, params, t){
270         return(c(params$nu * x["N"], #birth
271                 params$beta[1] * (1+params$alp[1]*cos(2*pi*t))
272                 * x["SS"] * (x["IS"] + x["IR"]) * 1/x["N"],
273                 params$lat[1] * x["ES"],
274                 params$inf[1] * x["IS"],
275                 params$beta[2] * (1+params$alp[2]*cos(2*pi*t))
276                 * x["RS"] * (x["SI"] + x["RI"]) * 1/x["N"],
277                 params$lat[2] * x["RE"],
278                 params$inf[2] * x["RI"],
279                 params$beta[2] * (1+params$alp[2]*cos(2*pi*t))
280                 * x["SS"] * (x["SI"] + x["RI"]) * 1/x["N"],
281                 params$lat[2] * x["SE"],
282                 params$inf[2] * x["SI"],

```

```

283     params$beta[1] * (1+params$alp[1]*cos(2*pi*t))
284         * x["SR"] * (x["IS"] + x["IR"]) * 1/x["N"],
285     params$lat[1] * x["ER"],
286     params$inf[1] * params$ome * x["IR"],
287     params$inf[1] * (1 - params$ome) * x["IR"],
288     params$beta[2] * (1+params$alp[2]*cos(2*pi*t))
289         * x["A"] * (x["SI"] + x["RI"]) * 1/x["N"],
290     params$kappa * x["A"],
291     (params$mu) * x["SS"],
292     (params$mu) * x["ES"],
293     (params$mu) * x["IS"],
294     (params$mu) * x["RS"],
295     (params$mu) * x["RE"],
296     (params$mu) * x["RI"],
297     (params$mu) * x["SE"],
298     (params$mu) * x["SI"],
299     (params$mu) * x["SR"],
300     (params$mu) * x["ER"],
301     (params$mu) * x["IR"],
302     (params$mu) * x["RR"],
303     (params$mu) * x["A"],
304     params$imm[1] * x["N"],
305     params$imm[2] * x["N"],
306     params$imm[3] * x["N"],
307     params$imm[4] * x["N"]
308 ))
309 }
310
311 # Adaptive tau for each IA parameters
312 for(k in 1:nrow(IA_fn_df)){
313   for(j in 1:realizations){
314     params = list(
315       lat = c(1/T_lat.m, 1/T_lat.w),
316       inf = c(1/T_inf.m, 1/T_inf.w),
317       R0 = c(Reff.m, Reff.w),
318       mu = b_rate,
319       nu = d_rate,
320       beta = c(beta.m, beta.w),
321       alp = c(alp.m, alp.w),
322       ome = IA_df[k, 2],
323       kappa = IA_df[k, 1],
324       imm = c(imm.IS, imm.IR, imm.SI, imm.RI)

```

```

325 )
326
327 coupled.sim <- as_tibble(ssa.adaptivetau(init.values, transitions,
328                                     lvrates, params, tf = 300)) %>%
329   mutate(Im = IS + IR) %>%
330   mutate(Iw = SI + RI)
331
332   # Save sim data
333   fn <- paste0("./str", IA_fn_df[k, 2], IA_fn_df[k, 1],
334               "_raw_", j, ".rds")
335   saveRDS(coupled.sim, file = fn)
336 }
337 }

```

The following code extracts evenly-spaced disease incidence time series from the simulation results. This was then used to perform spectral analysis using the previous code from Appendix C.1.

```

338 library(tidyverse)
339 library(EMD)
340
341 realization = 30
342
343 # IA parameters (for calling in sim data)
344 IA_str_fn = c("025", "05", "075", "1")
345 IA_len_fn = c("_1mon", "_3mon", "_6mon", "_9mon", "_12mon", "_15mon",
346              "_18mon", "_21mon", "_24mon", "_36mon", "_60mon")
347
348 # Define event spaced time points
349 tpoints <- seq(7/365, 200, by = 7/365) + 100
350 tpoints2 <- c(100, tpoints)
351
352 for(ia_str in IA_str_fn){
353   for(ia_len in IA_len_fn){
354     for(d in 1:realization){
355       # Read in raw sim data
356       sim.data <- readRDS(paste0("./str", ia_str, ia_len,
357                                 "_raw_", d, ".rds")) %>%
358         select(time, Cm, Cw)
359
360       # Interpolate accumulator for even timepoints
361       C_m <- approx(x = sim.data$time,

```

```
362         y = sim.data$Cm,
363         xout = tpoints2)
364     C_w <- approx(x = sim.data$time,
365                 y = sim.data$Cw,
366                 xout = tpoints2)
367
368     # Create data frame of incidence extracted from sim data
369     df <- data.frame(t = tpoints,
370                    m = diff(floor(C_m$y)),
371                    w = diff(floor(C_w$y)))
372
373     # Sqrt normalize incidence data
374     e_m <- emd(df$m, df$t, boundary="wave")
375     e_w <- emd(df$w, df$t, boundary="wave")
376     df <- df %>%
377         mutate(m.trend = e_m$residue) %>%
378         mutate(m.sqnm = sqrt(m/m.trend)) %>%
379         mutate(w.trend = e_w$residue) %>%
380         mutate(w.sqnm = sqrt(w/w.trend))
381
382     # Save data
383     fn <- paste0("./str", ia_str, ia_len,
384                "_clean_", d, ".rds")
385     saveRDS(df, file = fn)
386   }
387 }
388 }
```